UNIVERSITÀ DEGLI STUDI DI MILANO

PhD course in Molecular and Cellular Biology
XXXIV Cycle

“Long-distance turgor changes induce systemic activation of plant GLUTAMATE RECEPTOR-LIKE channels”

Matteo Grenzi

PhD thesis

Scientific supervisor and tutor:
Prof. Alex Costa

Academic year: 2020/2021

Index

Abstract (Italian version) 1

Abstract (English version) 3

Chapter I. Bibliographic introduction 5

I.1. *Ca^{2+} as a second messenger* 5

I.2. *Shaping the Ca^{2+} signature: Ca^{2+} importers and exporters* 7

I.3. *Shaping the Ca^{2+} signature: the contribution of organelles* 7

I.4. *Shaping the Ca^{2+} signature: the Endoplasmic Reticulum (ER)* 9

I.5. *Glutamate Receptor-Like channels (GLRs)* 11

I.6. *Evolutionary origin of plant GLRs* 15

I.7. *GLRs at the crossroads of long-distance signalling in plants* 16

I.8. *How do plant GLRs work?* 17

I.9. *A plethora of tools for the study of Ca^{2+} dynamics in vivo* 21

I.10. *Yellow Cameleon – A FRET-based Ratiometric Sensor* 22

I.11. *R-GECO1, GCaMP3, ER-GCaMP6-210 – Intensiometric Sensors* 23

I.12. *Measurement of glutamate dynamics in vivo* 24

Aim of the thesis 26

Chapter II. Results and discussion 27

II.1. *Leaf wound triggers leaf-to-leaf $[L\text{-}Glu]_{apo}$ and AtGLR3.3-dependent $[Ca^{2+}]_{cyt/nuc}$ increases* 27

II.2. *Burn induce systemic increase in $[L\text{-}Glu]_{apo}$ precedes subsequent $[Ca^{2+}]_{cyt/nuc}$ rise* 29

II.3. *AtGLR3.3 is needed for burn and L-Glu induced $[Ca^{2+}]_{cyt/nuc}$ increase in the phloem cells* 31

II.4. *Endoplasmic reticulum does not act as $[Ca^{2+}]_{cyt/nuc}$ sink in AtGLR3.3-dependent responses* 31

II.5. *The amino acid-binding by AtGLR3.3 is required for its function* 37

II.6. *In vivo iGluSnFR characterization suggests µM concentrations of L-Glu accumulate systemically in response to mechanical damage* 46

II.7. *Local delivery of µM concentrations of L-Glu into leaf tissues does not trigger systemic propagating $[Ca^{2+}]_{cyt}$ waves* 48

II.8. *Leaf-burning induces the bending of the stem independently from AtGLR3.3 activity* 51

II.9. *Hypo-osmotic stress triggers systemic root-to-shoot $[L\text{-}Glu]_{apo}$ and AtGLR3.3-dependent $[Ca^{2+}]_{cyt}$ waves* 54

Chapter III. Conclusions and future perspectives 57

Chapter IV. Materials and methods 61

IV.1. *Plant material and growth conditions* 61

IV.2. *Bacterial strains* 62

IV.3. *Molecular cloning and plasmid constructs – pGreen0029 pSUC2::YC3.6* 62

IV.4. *Molecular cloning and plasmid constructs – pB7WG2.0 p35S::GLR3.3-EGFP* 62

IV.5. *Molecular cloning and plasmid constructs – pGreen0179 pGLR3.3::gGLR3.3* 63

IV.6. *Transformation of plasmid DNA into DH5α competent E. coli cells* 63

IV.7. *Plasmid DNA extraction* 63

IV.8. *Agrobacterium tumefaciens transformation* 64

IV.9. *Transient Expression in Nicotiana benthamiana leaves* 64

IV.10. *Transgenic plants* 64

IV.11. *Genomic DNA extraction from plant tissues* 65

IV.12. *Genotyping of Arabidopsis thaliana insertion mutant alleles* 66

IV.13. *PCR conditions* 66

IV.14. *RNA extraction and quantitative qRT-PCR analysis* 67

IV.15. *GUS staining* 67

IV.16. *Preparation of transverse sections* 68

IV.17. *Confocal laser scanning microscopy* 68

IV.18. *Wide-field fluorescence microscopy* 68

IV.19. Spinning Disk Confocal Microscopy 69

IV.20. *Stereomicroscopy of wound-, burn- and hypoosmotic stress-induced Ca^{2+} and L-Glu increase in adult plants* 69

IV.21. *Image analysis* 70

IV.22. *Measurements of the burning-induced bending of the stem of the primary inflorescence* 70

IV.23. *Kymograph* 71

IV.24. *Seedling imaging* 71

IV.25. *Imaging in longitudinal stem sections* 71

IV.26. *Organic Electronic Ion Pump fabrication and characterization (Performed by Eleni Stavrinidou's lab)* 71

IV.27. *L- and D-Glu UHPLC-MS/MS analysis (Performed by Eleni Stavrinidou's lab)* 72

IV.28. *In planta glutamate delivery with the c-OEIP (Performed in collaboration with Eleni Stavrinidou's lab)* 73

IV.29. *Statistical analysis* 73

Chapter V. Supplementary materials 74

Chapter VI. References 75

List of scientific publications on Journals with Impact Factor 87
(the manuscripts are attached)

Abstract (Italian version)

Nel corso della loro vita le piante, essendo organismi sessili, sono continuamente soggette a cambiamenti ambientali che necessitano di essere accuratamente percepiti, a cui devono seguire appropriate risposte sia a livello locale che sistemico che ne garantiscano la sopravvivenza. Il calcio (Ca^{2+}) è uno ione che agisce come importante secondo messaggero in tutti gli esseri viventi, in grado di accoppiare la percezione di uno stimolo extracellulare a peculiari risposte intracellulari. La specificità di trasduzione del segnale basata sul Ca^{2+} è ottenuta grazie alla generazione di transienti incrementi della sua concentrazione citosolica ($[Ca^{2+}]_{cyt}$), specifici nella loro evoluzione spaziale e temporale, alla quale ci si riferisce come “Ca^{2+} signatures”. La decodifica delle “Ca^{2+} signatures” da parte di proteine capaci di legare il Ca^{2+} permette la messa in atto di appropriate risposte fisiologiche. Nelle piante, è stato documentato che transienti variazioni citosoliche di Ca^{2+} sono coinvolte in svariati processi fisiologici che includono lo sviluppo della radice, lo sviluppo del tubetto pollinico e il processo di fecondazione, la risposta a stress abiotici, la regolazione dell’interazione pianta-microbo. Transienti incrementi nella $[Ca^{2+}]_{cyt}$ con caratteristica intensità, frequenza, dinamica e durata sono generati dalla azione orchestrata di sistemi di influsso ed efflusso del Ca^{2+}, che includono canali, pompe e scambiatori del Ca^{2+} che sono localizzati a livello delle membrane cellulari. Data l’importanza e l’universalità della trasduzione del segnale basata sul Ca^{2+}, risulta essere di primaria importanza l’identificazione degli attori molecolari che governano la generazione dei segnali Ca^{2+}. In questo contesto, lo studio delle dinamiche del Ca^{2+} *in vivo* rappresenta un potente strumento investigativo.

Nel corso del mio dottorato di ricerca, ho esplorato il meraviglioso mondo del “Ca^{2+} imaging” utilizzando il vasto universo di Biosensori fluorescenti per il Ca^{2+} geneticamente codificati. Ho appreso e affinato tecniche per produrre immagini di alta qualità rappresentative di dinamiche del Ca^{2+} *in vivo*, sia a livello di intero organismo che a singola cellula. Le competenze che ho acquisito mi hanno permesso di contribuire a vari progetti tutti accomunati da quello che è un comune denominatore, ovvero il ruolo cardine del Ca^{2+} nella regolazione di svariati processi di trasduzione del segnale. Mi sono avventurato nello studio di vari aspetti legati alla segnalazione del Ca^{2+} tra cui: (i) gli aumenti della $[Ca^{2+}]_{cyt}$ indotti nelle cellule dell’apice radicale in risposta a differenti amminoacidi, contribuendo a definire i determinanti molecolari sottostanti a tali risposte (Alfieri et al., 2020); (ii) la caratterizzazione dei transienti incrementi della $[Ca^{2+}]_{cyt}$ indotti da auxine naturali e da molecole analoghe dell’auxina, e la decifrazione del ruolo di alcuni attori molecolari coinvolti nella genesi delle risposte $[Ca^{2+}]_{cyt}$ indotte da auxina (Wang, Himschoot, Grenzi et al., 2022); (iii) lo sviluppo di un nuovo biosensore per il Ca^{2+} geneticamente codificato per indagare il ruolo del reticolo endoplasmico nella modellazione delle “Ca^{2+} signatures” in processi di sviluppo, così come in risposta a vari stimoli (Resentini, Grenzi et al., 2021); (iv) l’effetto di modulazione che alcuni composti chimici hanno sulle oscillazioni spontanee nella $[Ca^{2+}]_{cyt}$ delle cellule di guardia che governano l’apertura e la chiusura degli stomi. Ho inoltre contribuito alla scrittura di reviews legate al mondo del “Ca^{2+} signalling” in

pianta. Tutti i lavori pubblicati, così come i lavori in preparazione, sono allegati al termine di questa dissertazione, alla quale rimando gentilmente il lettore. Qui presenterò il lavoro portato avanti nel contesto del mio progetto di dottorato, il quale si è focalizzato principalmente alla comprensione dei meccanismi rapidi di segnalazione a lunga distanza.

Le risposte sistemiche sono governate da eventi di segnalazione a lunga distanza che richiedono l'attività dei Recettori del Glutammato (GLRs). I GLRs sono proteine omologhe ai Recettori del Glutammato animali (iGluRs), ovvero canali ionici attivati da ligando presenti nel sistema nervoso centrale. Nonostante negli animali è chiaro che gli iGluRs mediano il passaggio di ioni a seguito del loro legame con il L-Glutammato, il meccanismo attraverso cui i GLRs sono attivati in pianta è ancora largamente discusso. Ad esempio, non si è ancora a conoscenza se il legame dell'aminoacido ai GLRs sia realmente necessario per la loro attivazione.

In questo lavoro di tesi, analizzando i dati della struttura cristallografica del Dominio di Legame all' amminoacido (LBD) del *At*GLR3.3 di *Arabidopsis thaliana,* abbiamo identificato dei residui amminoacidici coinvolti nel legame del glutammato. Abbiamo dunque introdotto mutazioni puntiformi nella sequenza genomica del *At*GLR3.3 per inficiare o abolire la sua abilità di legare il ligando amminoacidico, e con i costrutti ottenuti abbiamo eseguito una complementazione genetica dei mutanti knock out per il gene GLR3.3 (*glr3.3-1* e *glr3.3-2)*. Combinando analisi di imaging, genetica, e bioelettronica, dimostriamo che un danno a livello della foglia, come una ferita o una bruciatura, e l'applicazione di uno stress ipoosmotico alla radice, inducono l'aumento sistemico nella concentrazione apoplastica di L-Glutammato che attiva i GLRs attraverso il legame al loro LBD. Inoltre, il nostro lavoro supporta l'evidenza che gli eventi di segnalazione a lunga distanza siano governati da cambiamenti nello stato di turgore della pianta e che i GLRs siano a valle di essi.

Abstract (English version)

Throughout their life plants, being sessile organisms, are continuously exposed to environmental challenges that need to be properly perceived and that require appropriate local and systemic responses. Calcium ion (Ca^{2+}) is a key second messenger in all living beings that couples the perception of extracellular stimuli to characteristics intracellular responses. The specificity of the Ca^{2+}-based signalling is achieved through the generation of specific spatial and temporal transient elevations in the cytosolic Ca^{2+} concentration $[Ca^{2+}]_{cyt}$, which are referred to as "Ca^{2+} signatures". The interplay of Ca^{2+} signatures with a toolkit of cognate Ca^{2+}-binding proteins that decode these increases allow the plant to implement a series of tailored physiological responses (e.g., gene expression, metabolism, developmental reprogramming) to withstand the stress. In plants, transient increases in the $[Ca^{2+}]_{cyt}$ have been documented to be involved in several physiological processes including root or pollen tube growth and fertilization, abiotic stress responses, plant-microbe interaction. Ca^{2+} transients with unique magnitude, frequency, shape, and duration are generated by the orchestrated action of Ca^{2+} influx and efflux systems that include Ca^{2+} channels, pumps, and exchangers located at different cellular membranes. Given the importance and universality of Ca^{2+}-based signalling, the identification of actors of the molecular machinery that govern the generation of Ca^{2+} signals is of primary importance. In this context, the study of Ca^{2+} dynamics *in vivo* represents a powerful tool.

In the frame of my PhD, I explored the marvellous world of Ca^{2+} imaging using some of the instruments made available from a vast universe of genetically encoded fluorescent Ca^{2+} biosensors. I learned and refined techniques to produce high-end images of *in vivo* Ca^{2+} dynamics both at the entire organism and single-cell level. The expertise that I acquired allowed me to contribute to different projects, all unified by the common denominator that is the master regulatory role of Ca^{2+} in many signalling processes. I therefore contributed to the study of: (i) the $[Ca^{2+}]_{cyt}$ responses of root tip cells in response to different amino acids, helping to define the molecular determinants involved in the process (Alfieri et al., 2020); (ii) the characterization of $[Ca^{2+}]_{cyt}$ transients induced by the administration of natural auxins and auxin analogues, and the deciphering of the role of molecular actors involved in the genesis of the auxin-induced $[Ca^{2+}]_{cyt}$ response (Wang, Himschoot, Grenzi et al., 2022); (iii) the development of a novel genetically encoded Ca^{2+} biosensors to unravel the role of the endoplasmic reticulum in the shaping of the Ca^{2+} signature in developmental processes, as well as in response to various stimuli (Resentini, Grenzi et al., 2021); (iv) the modulatory effects of chemicals on the spontaneous $[Ca^{2+}]_{cyt}$ oscillations of guard cells that govern the opening and closing of stomata. I also contributed to the preparation of reviews linked to the field of Ca^{2+} signalling. All the published manuscripts, as well as works in preparation, are attached at the end of this dissertation, to which I kindly redirect the readers. Here, I am presenting the main work of my PhD project which focused on the understanding of how local damages can trigger inducible defence mechanisms in systemic organs and tissues.

Systemic responses are mediated by long-distance signalling that requires the activity of Glutamate Receptor-Like channels (GLRs). GLRs are homologs of animal Ionotropic Glutamate Receptors (iGluRs) which are ligand-gated cation channels in the central nervous system. Even though iGluRs are gated through the binding with the L-Glutamate, the mechanism throughout GLRs are activated *in planta* is poorly understood. As an example, we still do not know if the GLRs binding of amino acids is necessary for their activity.

In this PhD thesis, we took the advantage of the recently obtained crystal structure of the *Arabidopsis thaliana At*GLR3.3 Ligand Binding Domain (LBD) to identify residues involved in the amino acid-binding. We, therefore, introduced single point mutations in the genome sequence of the *At*GLR3.3 gene to prevent or abolish its amino acid-binding, and with the obtained constructs we complemented the *glr3.3* KO. By combining high-end imaging, genetics, and bioelectronics we prove that leaf injury, such as wound and burn, and root-applied hypo-osmotic stress induce the systemic apoplastic increase of L-Glutamate that activates GLR channels through their LBD. In addition, our work supports the evidence that long-distance signalling is governed by a systemic change in the turgor state and that GLRs are downstream of it.

Chapter I. Bibliographic introduction

I.1 Ca^{2+} as a second messanger

Peculiar physical and chemical properties dictate the ability of Ca^{2+} ions to interact eagerly with biological molecules (Jaiswal, 2001). Because of this reactivity, at high concentration Ca^{2+} ions affect the integrity of lipid membranes, cause the aggregation of proteins and nucleic acids, interact with free phosphate molecules present in a cell as inorganic phosphate (Pi) and eventually precipitate as Ca^{2+} phosphate (Case et al., 2007). These effects are incompatible with life, and they are the reason why since their origin all living organisms evolved homeostatic mechanisms to keep the concentration of Ca^{2+} ions in the cytosol ($[Ca^{2+}]_{cyt}$) low. Thus, the free $[Ca^{2+}]_{cyt}$ is maintained in the range of hundreds of nanomolar (100–200 nM), a value that is ~10'000-20'000 times lower than that in both the extracellular milieu and some subcellular compartments where its concentration can reach up to millimolar ranges (Case et al., 2007; Stael et al., 2012; Resentini et al., 2021). A substantial part of an organism's metabolic energy is consumed to maintain the $[Ca^{2+}]_{cyt}$ in the physiological range, through mechanisms of active transport that use the energy of hydrolysis of ATP or the proton motive force to extrude Ca^{2+} ions against the unfavourable electrochemical gradient (Demidchik et al., 2018). De facto the evolution managed to gain an advantage from this constrain, enduing organisms of the ability to take advantage of the large electrochemical gradient that exists for Ca^{2+} ions across the cell's membranes for signalling purposes. Cells exploit these gradients to generate rapid intracellular concentration changes, which provide the basis for Ca^{2+} signalling (Sanders et al., 1999; Dodd et al., 2010; Grenzi et al., 2021a). Nowadays Ca^{2+} is universally recognized as a ubiquitous second messenger in both prokaryotes and eukaryotes (Berridge et al., 2000). In plants, a wide variety of environmental and endogenous stimuli can evoke a rise of the free $[Ca^{2+}]_{cyt}$ (Monshausen, 2012; Grenzi et al., 2021a; Resentini et al., 2021). Remarkably, the increase in $[Ca^{2+}]_{cyt}$ possesses the characteristic of an "analog" signal rather than that of a "digital" one. In fact, a stimulus-induced Ca^{2+} signal is not characterized by an "all or nothing" nature as can be a classic binary digital system, but it can be modulated by the specific nature and intensity of the stimulus. McAinsh and Hetherington proposed a model according to which different stimuli can differentially affect the $[Ca^{2+}]_{cyt}$, evoking transient $[Ca^{2+}]_{cyt}$ increases that can vary in amplitude, frequency and duration. McAinsh and Hetherington coined the term "Ca^{2+} signature" to describe these unique stimulus-specific Ca^{2+} fingerprints (McAinsh and Heterington, 1998). As an exemplification of the concept, Ca^{2+} signatures characterizing developmental processes and responses to a variety of stimuli that I measured during my PhD are shown in **Fig. I-1**. Experimental evidence demonstrated in the model plant species *Arabidopsis thaliana* (hence after *Arabidopsis*) that different Ca^{2+} signatures encode stimulus-specific information, which decoding leads to distinct gene expression profiles (Whalley et al., 2011; Whalley and Knight, 2012). The decoding phase is carried out by a toolkit of Ca^{2+}-binding proteins that can act as primary responders or sensor relays. Primary responders are proteins whose activity is directly regulated by the binding of Ca^{2+} ions (e.g calcium-dependent kinases). Sensor relays are proteins undergoing a conformational change upon the binding of Ca^{2+} ions that enable them to interact with different targets and in turn modulate their activities (e.g Calmodulin, Calmodulin-like proteins, Calcineurin B-like proteins) (Kudla et al., 2018; Tian et al., 2020). Thus, Ca^{2+} signals trigger tailored responses altering gene expression and metabolism that allow plants to withstand environmental changes and survive (De Falco et al., 2010).

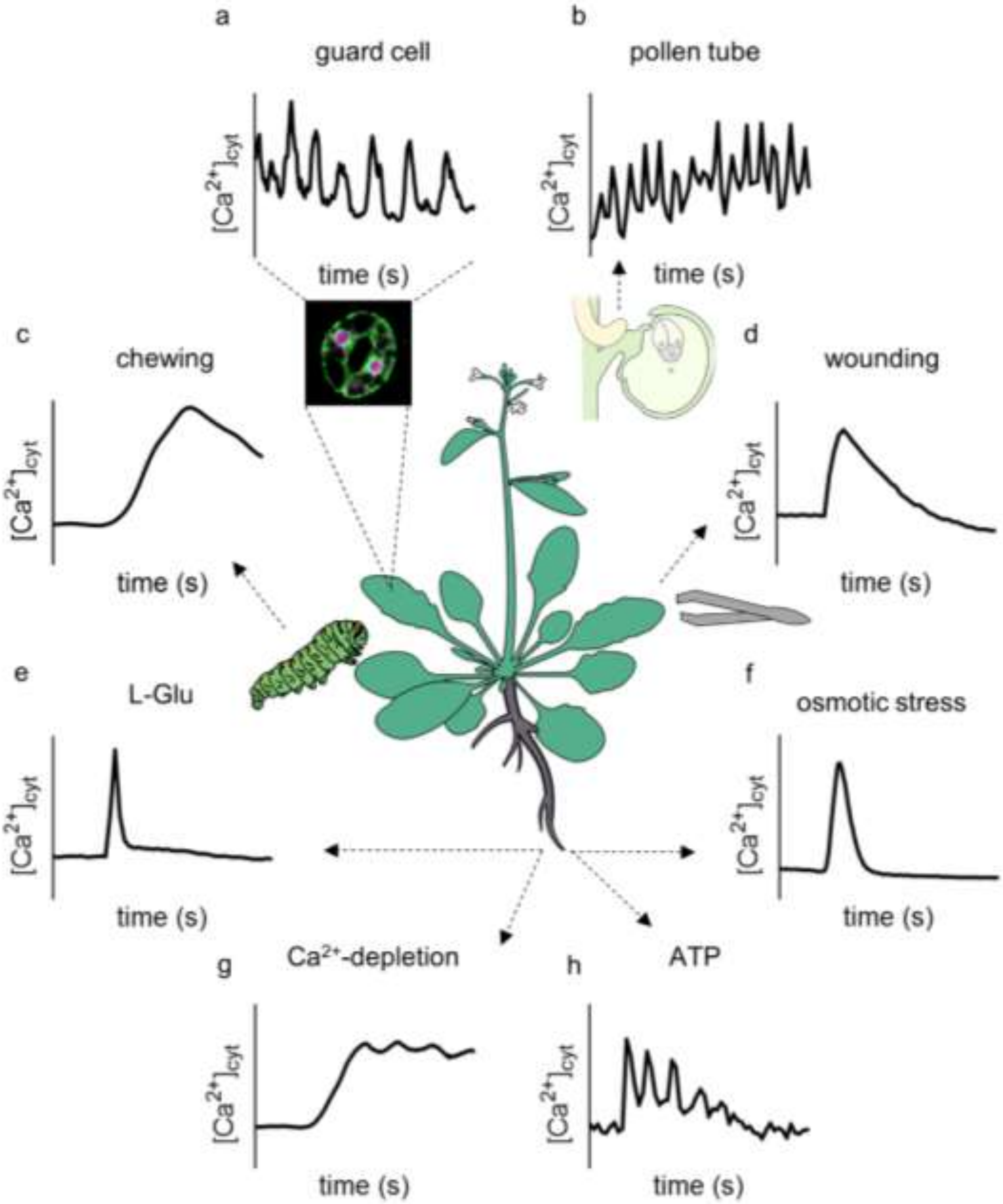
a
guard cell
$[Ca^{2+}]_{cyt}$
time (s)
b
pollen tube
$[Ca^{2+}]_{cyt}$
time (s)
c
chewing
$[Ca^{2+}]_{cyt}$
time (s)
d
wounding
$[Ca^{2+}]_{cyt}$
time (s)
e
L-Glu
$[Ca^{2+}]_{cyt}$
time (s)
f
osmotic stress
$[Ca^{2+}]_{cyt}$
time (s)
g
Ca^{2+}-depletion
$[Ca^{2+}]_{cyt}$
time (s)
h
ATP
$[Ca^{2+}]_{cyt}$
time (s)

Figure I-1. Representative Ca^{2+} signatures induced by a variety of stimuli. (a) Spontaneous cytosolic Ca^{2+} oscillations in guard cells**. (b)** Spontaneus cytosolic Ca^{2+} oscillation in the tip of a growing pollen tube. **(c)** Chewing-induced cytosolic Ca^{2+} increase. **(d)** Wounding-induced cytosolic Ca^{2+} increase. **(e)** Cytosolic Ca^{2+} increase in root tip cells in response to L-Glu. **(f)** Cytosolic Ca^{2+} increase in root tip cells in response to osmotic stress. **(g)** Cytosolic Ca^{2+} increase in root tip cells in response to Ca^{2+} depletion. **(h)** Cytosolic Ca^{2+} increase in root tip cells in response to ATP.

I.2 Shaping the Ca^{2+} signature: Ca^{2+} importers and exporters

Ca^{2+} has two positive charges in the external orbital and cannot cross the membranes. Nonetheless, electrophysiological evidence showed that plant membranes are permeable to Ca^{2+} and are characterized by Ca^{2+} conductance (Demidchik et al., 2002). The influx of Ca^{2+} ions is mediated by membrane-spanning proteins defined as Ca^{2+} channels. With the opening of Ca^{2+} channels, the large electrochemical potential allows the passive influx of Ca^{2+} into the cytosol from either the extracellular space or intracellular compartments, so that the $[Ca^{2+}]_{cyt}$ can be elevated by a factor of 10-20 within seconds (Bose et al., 2011). Notably, ion channels that mediate the influx of Ca^{2+} ions are called Ca^{2+}-permeable channels in plants, since channels with a Ca^{2+}-selective filter have not been identified so far (Swarbrek et al., 2013). Five families of Ca^{2+}-permeable channels have been identified in *Arabidopsis*: Glutamate Receptor-Like (GLRs – 20 members), Cyclic Nucleotide Gated Channels (CNGCs – 20 members), Two Pore Channel (TPC – 1 member), Mechanosensitive Channels (MCAs – two members), reduced hyperosmolality-induced $[Ca^{2+}]_{cyt}$ increase (OSCAs – 15 members) (Kudla et al., 2018). A high $[Ca^{2+}]_{cyt}$ can be maintained only for a short time window otherwise the onset of cytotoxic effects and cell death occurs (Lecourieux et al., 2006). Thus, the action of Ca^{2+}-permeable channels must be rapidly counteracted by the activity of Ca^{2+} transporters that actively pump Ca^{2+} ions out of the cytosol against their electrochemical gradient and restore the basal $[Ca^{2+}]_{cyt}$. These Ca^{2+} transporters belong to at least four families in *Arabidopsis*: Ca^{2+}-ATPases (ACAs), ER-type Ca^{2+}-ATPases (ECAs) and P1-ATPases all use the hydrolysis energy of ATP and Ca^{2+} exchangers (CAX) that dissipate the proton motive force (Kudla et al., 2018). Last but not least, a pool of Ca^{2+}-binding molecules (e.g ATP, ADP, phosphates, anionic heads of lipids, Ca^{2+}-binding proteins etc.) take part in the buffering of excess Ca^{2+} (Demidchik et al., 2018). It was estimated in mouse neuroblastoma cells that the cytosol has a buffering capacity of 1700 Ca^{2+} ions bound per Ca^{2+} ion free (Fleet et al., 1998). As the result of the orchestrated action of Ca^{2+}-importers, Ca^{2+}-exporters and Ca^{2+}-buffering systems the physiological $[Ca^{2+}]_{cyt}$ is maintained constant and, in response to a stimulus, specific Ca^{2+}-signatures are shaped (Demidchik et al., 2018).

I.3 Shaping the Ca^{2+} signature: the contribution of organelles

In plants, several reports highlighted the preeminent role of apoplast as the primary source of Ca^{2+} ions in the generation of cytosolic Ca^{2+} increases in response to many stimuli (Stael et al., 2012; Costa et al., 2018). This is not unusual considering that the cell wall is characterized by an estimated free Ca^{2+} concentration up to 1mM and represents, together with the vacuole, the main Ca^{2+} store (Conn et al., 2011). Nonetheless, scientific efforts of the last two decades emphasized how subcellular compartments can participate in the shaping of Ca^{2+} signatures acting as both Ca^{2+} sinks and Ca^{2+} sources (Costa et al., 2018; Resentini et al., 2021), and how at least chloroplast and nucleus can even generate their own organellar Ca^{2+} signal (Xiong et al., 2006; Loro et al., 2016;

Sello et al., 2016; 2018; Kelner et al., 2018; Leitão et al., 2019) (**Fig. I-2**). Remarkably, computational and modelling approaches estimated that in guard cells more than 95% of Ca^{2+} ions participating in the genesis of $[Ca^{2+}]_{cyt}$ increases comes from internal stores (Minguet-Parramona et al., 2016). For a general overview of the organelle's role in the shaping of the Ca^{2+} signature, I refer to a recent review that we have published (Resentini et al., 2021). In the next session, I'll summarize pieces of evidence demonstrating the importance of the Endoplasmic Reticulum (ER) in the control of $[Ca^{2+}]_{cyt}$ homeostasis and in the shaping of $[Ca^{2+}]_{cyt}$ signatures, a field in which I dedicated part of my PhD.

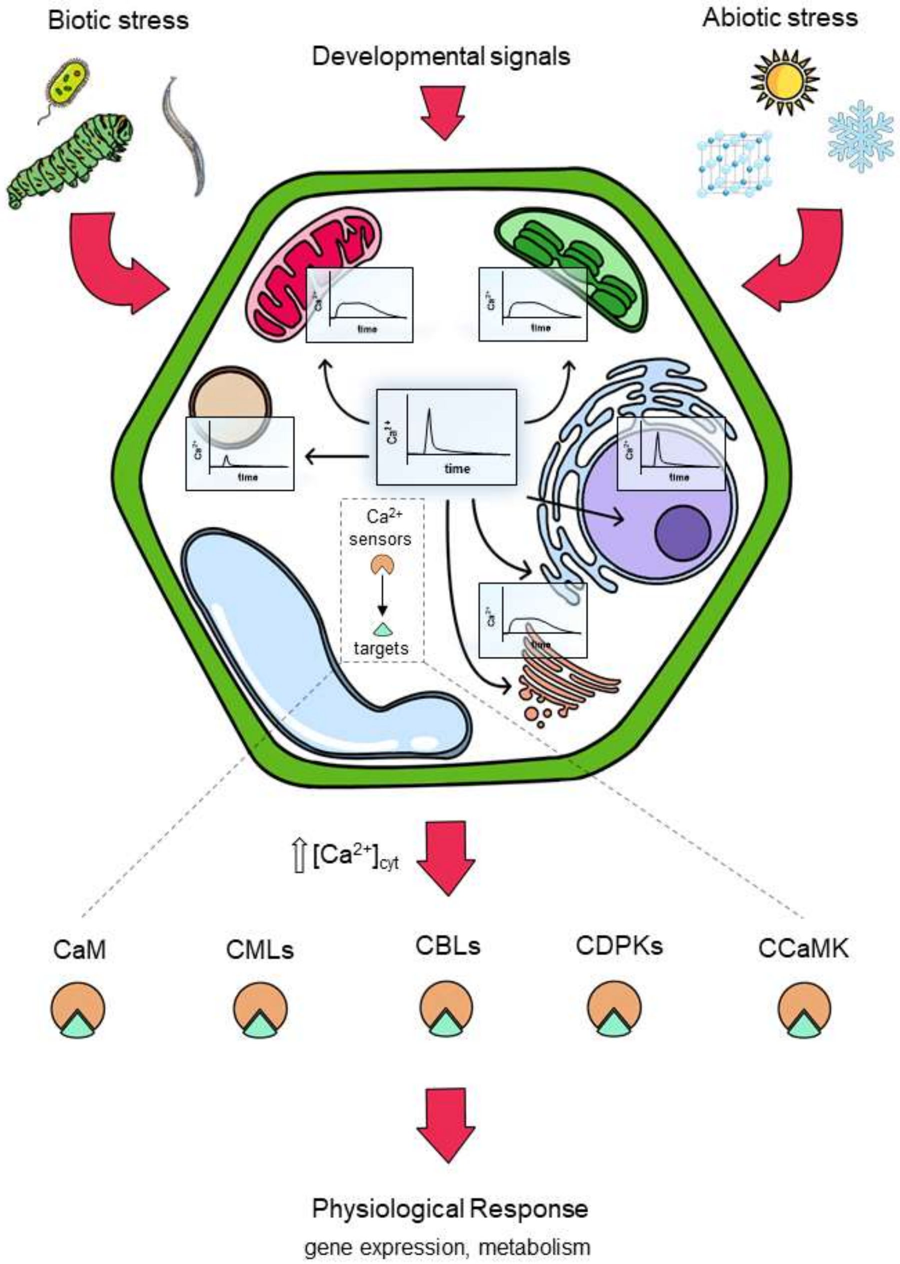
Biotic stress
Developmental signals
Abiotic stress
Ca^{2+}
time
Ca^{2+} sensors
targets
$\Uparrow [Ca^{2+}]_{cyt}$
CaM
CMLs
CBLs
CDPKs
CCaMK
Physiological Response
gene expression, metabolism

Figure I-2. Biotic and abiotic stresses as well as developmental stimuli can trigger cytosolic and organellar $[Ca^{2+}]$ increases. Cytosolic Ca^{2+} transients are decoded by different Ca^{2+} sensors and relays, such as CaM, CMLs, CBLs proteins, CDPKs, and CCaMK that trigger precise and tailored responses altering gene expression and metabolism.

I.4 Shaping the Ca^{2+} signature: the Endoplasmic Reticulum (ER)

Besides its role in protein synthesis, maturation and sorting, the ER lumen is a major reservoir of intracellular Ca^{2+}. In animal cells, the total $[Ca^{2+}]$ is estimated to be 2 mM, and the free Ca^{2+} concentration ranges from 50 µM to 500 µM (Coe and Michalak, 2009). The molecular mechanism behind the ER contribution in Ca^{2+} homeostasis and Ca^{2+} signalling is known in detail in animals. In animals, the release of Ca^{2+} ions from the ER lumen to the cytosol is regulated by inositol triphosphate (InsP3R) and Ryanodine (RyR) receptors that are ER-localized ligand-gated Ca^{2+}-permeable channels whereas the sarcoplasmic/endoplasmic reticulum Ca^{2+}-ATPase (SERCA) pump mediates the refill of Ca^{2+} from the cytosol into the ER lumen (Lee and Michalak, 2012). *In vivo* measurements estimated that the ER resting Ca^{2+} concentration is similar between animal and plant cells, suggesting that also in plants the ER is a reservoir of Ca^{2+} (Iwano et al., 2009; Bonza et al., 2013). I*n vivo* measurements of *Arabidopsis* Ca^{2+} dynamics of both cytosol and ER lumen that I carried out in my PhD, revealed that in response to various stimuli that are known to induce a $[Ca^{2+}]_{cyt}$ elevation (i.e ATP, 1-naphtalacetic acid treatment in root cells, and leaf-wounding) an increase in the ER lumen $[Ca^{2+}]$ occurs. Interestingly, in most of the cases, the ER $[Ca^{2+}]$ accumulation temporally follows the cytosolic $[Ca^{2+}]$ increase, suggesting that in plant cells the ER works as a Ca^{2+} sink rather that a Ca^{2+} source (Resentini, Grenzi et al., 2021), confirming previous evidence (Bonza et al., 2013).

Plants possess a toolkit of ER-localized Ca^{2+}-transporters that comprises members from different classes: P-type IIA Ca^{2+}-ATPases (ACAs) and P-type IIB Ca^{2+}-ATPases (ECAs) families, as well as Cation/Ca^{2+} exchangers (CCXs) (Bonza and De Michelis, 2011; He et al., 2021; Resentini et al., 2021) (**Fig. I-3**). In the last decade, genetic evidence revealed the physiological relevance of ER-localized Ca^{2+}-transporters and Cation/Ca^{2+} exchangers in the regulation of Ca^{2+} homeostasis and signalling, as well as their importance in plant development (Costa et al., 2018; Resentini et al., 2021). The absence of *At*CCX2 activity reduces the $[Ca^{2+}]_{cyt}$ increase triggered by salt stress in *Arabidopsis*, with plants that are less salt-tolerant than wild type (Corso et al., 2018). Similarly, plants in which the *At*CCX2 activity was genetically ablated displayed a reduction in the $[Ca^{2+}]_{cyt}$ increase in response to hypo-osmotic and hyper-osmotic, as well as an exacerbation in the $[Ca^{2+}]$ elevation in the ER lumen induced by the same stresses (Corso et al., 2018). Overall, these reports pointed out the role of *At*CCX2 in regulating the Ca^{2+} fluxes between cytosol and ER in response to salt, hypo- and hyper-osmotic stress, and the importance of the ER in plant acclimatation to salt stress (Corso et al., 2018). The root bending toward the water (hydrotropism) is another important physiological aspect on which the impact of ER regulation in Ca^{2+} homeostasis was shown to be relevant. In *Arabidopsis*, it was observed that a $[Ca^{2+}]_{cyt}$ increase occurs in the root elongation zone (EZ) in response to an asymmetric decrease of the water potential. Importantly, the $[Ca^{2+}]_{cyt}$ increase was shown to positively regulate the root bending which occurs in response to this stimulus (Shkolnik et al., 2018). Both pharmacological inhibition using cyclopiazonic acid (CPA) and genetic ablation of

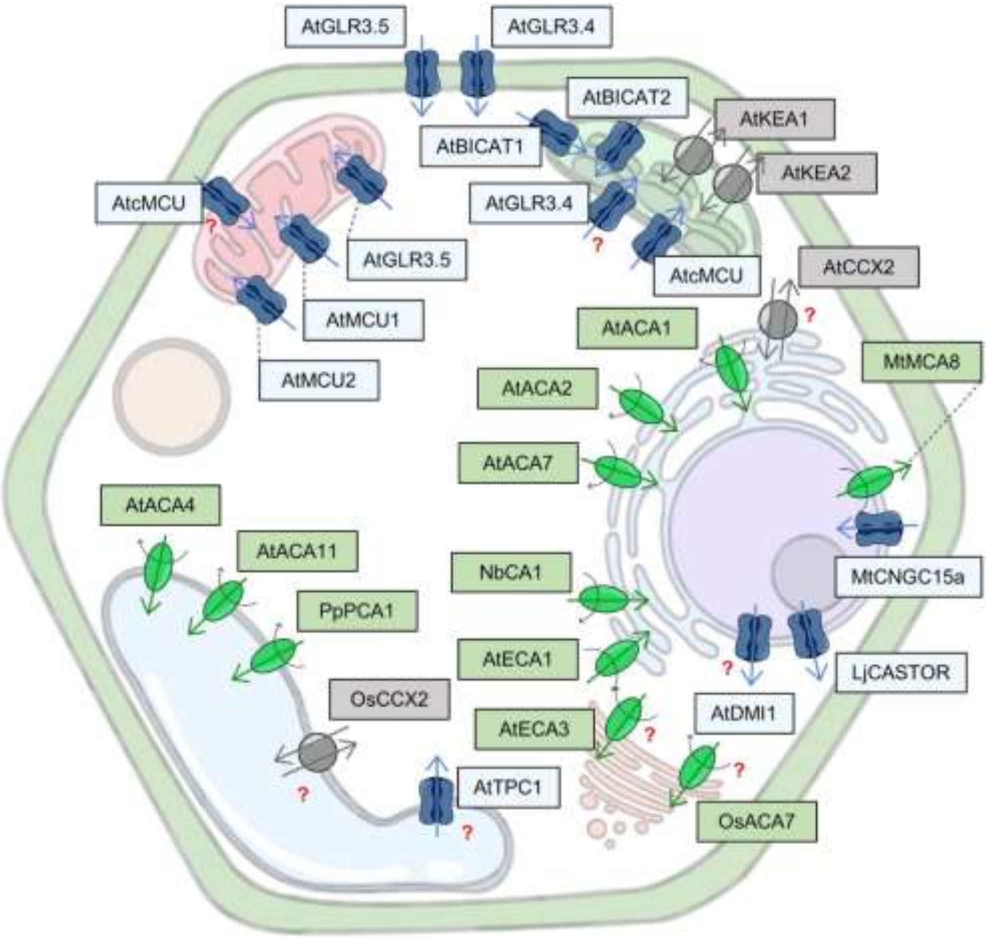
AtGLR3.5
AtGLR3.4
AtBICAT2
AtKEA1
AtBICAT1
AtKEA2
AtcMCU
AtGLR3.4
AtGLR3.5
AtcMCU
AtCCX2
AtMCU1
AtACA1
MtMCA8
AtMCU2
AtACA2
AtACA7
AtACA4
AtACA11
NbCA1
MtCNGC15a
PpPCA1
AtECA1
LjCASTOR
OsCCX2
AtECA3
AtDMI1
AtTPC1
OsACA7
?

Figure I-3. Channels and transporters localized in subcellular compartments reported to have a role in plant developmental processes and stress responses linked to the regulation of Ca^{2+} transport across membranes. The red question marks indicate that further studies are required. Channels are represented in blue, pumps in green, and cotransporters in grey. At, *Arabidopsis thaliana*; Lj, *Lotus japonicus*; Mt, *Medicago truncatula*; Nb, *Nicotiana benthamiana*; Pp, *Physcomitrium patens*; Os, *Oryza sativa.*

the *Arabidopsis At*ECA1 lead to a higher $[Ca^{2+}]_{cyt}$ increase and an exacerbation of the root bending (Shkolnik et al., 2018). The role of ER was also investigated in the front of plant immunity response. It was shown that silencing of the *Nicotiana benthamiana* ER-localized P-type IIB Ca^{2+}-ATPases *Nb*CA1 accelerates the cell death rate and increases the amplitude and duration of $[Ca^{2+}]_{cyt}$ spikes upon cryptogein treatment, a pathogen elicitor secreted by the oomycete *Phytophthora cryptogea*. *Os*XA10, a protein coded by a gene that confers resistance (*R* gene) to the bacterial blight in rice, is assembled as hexamers and is located at the ER membranes where it potentially works as a Ca^{2+} transporter (Tian et al., 2014). When expressed in rice and *Nicotiana benthamiana*, OsXA10 activity induces programmed cell death regulating the release of Ca^{2+} from the ER (Tian et al., 2014). In *Arabidopsis*, the triple *aca1/aca2/aca7* knock out (KO) mutant displays an increased amplitude and duration of the $[Ca^{2+}]_{cyt}$ increase triggered by the fragment of bacterial flagellin flg22 (Ishka et al., 2021). Moreover, this mutant is characterized by a higher $[Ca^{2+}]_{cyt}$ at resting and displays phenotypic defects (i.e smaller rosettes, high frequency of leaf lesions, compromised pollen fertility) suggesting the importance of the ER regulation of Ca^{2+} homeostasis for the proper plant development.

Regarding ER Ca^{2+} channels and the ability of ER to act as a Ca^{2+} source, direct homologues of mammalian InsP3 and Ryanodine receptors are absent in higher plant genomes (Stael et al., 2012; Edel et al., 2017). Still, since ER Ca^{2+} fluxes were measured in plants in response to voltage, Nicotinic Acid Adenine Dinucleotide Phosphate (NAADP), cyclic ADP-Ribose (cADPR) and InsP3 (Muir and Sanders, 1997; Klusener and Weiler, 1999; Navazio et al., 2000; Navazio et al., 2001) the existence of ER-localized Ca^{2+}-permeable channels can be postulated also in plants despite their molecular identity is still unknown (Stael et al., 2012; Edel et al., 2017). Up to date, the only evidence highlighting a role for a plant Ca^{2+}-permeable channels in the regulation of Ca^{2+} transport across the ER membranes comes from studies on *Medicago truncatula,* in which the *Mt*CNGC15 presumably promotes the release of Ca^{2+} from the ER lumen to the nucleoplasm to regulate nuclear-associated Ca^{2+} oscillations induced by symbiotic events (Charpentier et al., 2016). Recently, members of the GLRs family (i.e GLR2.1 in pollen, GLR3.1 in xylem contact cells, GLR3.3 in pollen and sieve elements) were identified to localize in the ER in *Arabidopsis*, but whether they are active or not in the ER, and how they work, is a question under debate (Wudick et al., 2018a; Nguyen et al., 2018).

I.5. Glutamate Receptor-Like channels (GLRs)

Animal Ionotropic Glutamate Receptors (iGluRs) are ligand-gated nonselective ion channels that mediate the excitatory neurotransmission in the central nervous system. They are found in all neuronal cell types where they assemble in homo- or heteromeric complexes and mediate the passage of ions (i.e Na^+, K^+, Ca^{2+}) upon binding of the neurotransmitters L-Glutamate, Glycine and D-Serine that are released in the synaptic space. Four classes are known, namely AMPA, NMDA, Kainate and Delta (δ) receptors, differing in the agonist that activate them as well as ionic selectivity and desensitization kinetics (Hadzic et al., 2017). They are historically studied for their role in neurotransmission, memory, and learning (Traynelis et al., 2010). It was surprising to find that genes homologous to animal iGluRs also exist in an organism not possessing a nervous system, the model plant *Arabidopsis*, which were called Glutamate Receptor-Like (*GLRs*) (Lam et al., 1998). Afterwards, the completion of the *Arabidopsis* genome sequencing project (The *Arabidopsis* Genome Initiative, 2000) enabled to uncover a family of 20 *AtGLRs* genes, which were grouped into three clades (I, II, III) based on sequence similarity (Lacombe et al., 2001; Chiu et al., 2002) (**Fig. I-4**). Due to the high sequence similarity with animal iGluRs (16-63%), the architecture, orientation, and stoichiometry of *At*GLRs are considered to be conserved (Lam et al., 1998; Chiu et al., 2002; Price et al., 2012). In iGluRs each subunit is composed of an extracellular Amino-Terminal Domain (ATD), a Ligand Binding Domain (LBD) composed of segments S1 and S2 both exposed to the external side of the plasma membrane, three transmembrane helices (M1, M3, M4) forming the channel pore plus the M2 helix that is not fully transmembrane that forms a P-loop structure regulating the channel selectivity, and the Carboxyl-Terminal Domain (CTD) constituting the cytoplasmic tail, arranged in the order ATD-S1-M1-M2-M3-S2-M4-CTD (Traynelis et al., 2010). Overall, the arrangement of plant GLRs is similar to iGluRs (Price et al., 2012; Wudick et al., 2018b; Green et al., 2021; Grenzi et al., 2021b) (**Fig. I-5**), even if several reports show a subcellular localization not only confined to the plasma membrane (Teardo et al., 2015; Wudick et al., 2018a), with some isoforms also partially localised to the ER (i.e. GLR3.3 in phloem cells) (Nguyen et al., 2018).

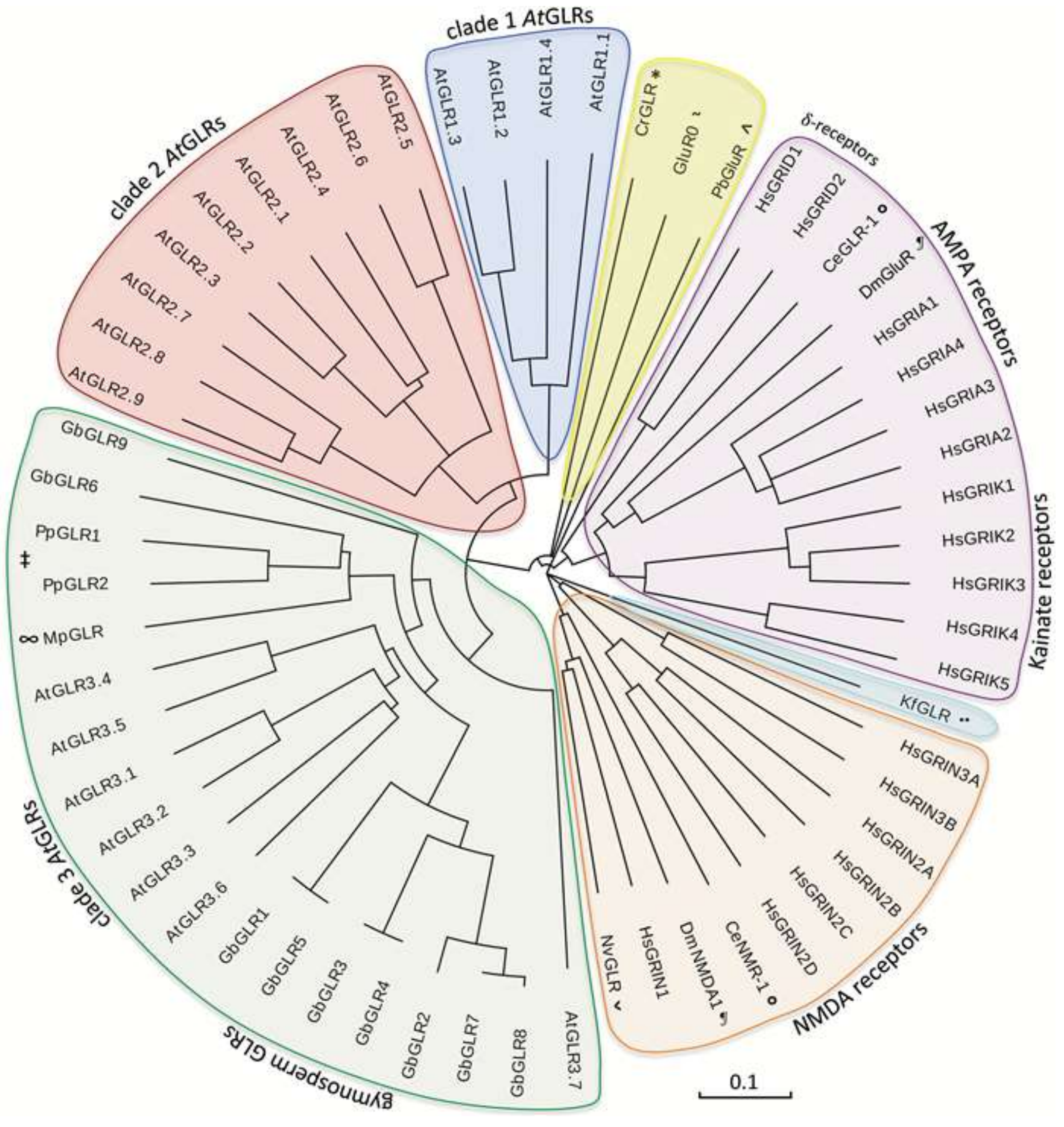
clade 1 AtGLRs
AtGLR1.3
AtGLR1.2
AtGLR1.4
AtGLR1.1
CrGLR *
GluR0 ~
PbGluR ^
δ-receptors
HsGRID1
HsGRID2
CeGLR-1 ∘
DmGluR
AMPA receptors
HsGRIA1
HsGRIA4
HsGRIA3
HsGRIA2
HsGRIK1
HsGRIK2
HsGRIK3
HsGRIK4
HsGRIK5
Kainate receptors
KfGLR ••
HsGRIN3A
HsGRIN3B
HsGRIN2A
HsGRIN2B
HsGRIN2C
HsGRIN2D
CeNMR-1 ∘
DmNMDA1
HsGRIN1
NvGLR ^
NMDA receptors
0.1
AtGLR3.7
GbGLR8
GbGLR7
GbGLR2
GbGLR4
GbGLR3
GbGLR5
GbGLR1
AtGLR3.6
AtGLR3.3
AtGLR3.2
AtGLR3.1
AtGLR3.5
AtGLR3.4
∞ MpGLR
PpGLR2
‡
PpGLR1
GbGLR6
GbGLR9
clade 3 AtGLRs
gymnosperm GLRs
clade 2 AtGLRs
AtGLR2.5
AtGLR2.6
AtGLR2.4
AtGLR2.1
AtGLR2.2
AtGLR2.3
AtGLR2.7
AtGLR2.8
AtGLR2.9

Figure I-4. **Phylogenetic relationship of Glutamate Receptors**. In this cartoon are shown selected Glutamate Receptors belonging to *Arabidopsis thaliana* (At), the nematode *Caenorhabditis elegans* (Ce), the unicellular green alga *Chlamydomonas rheinhardtii* (Cr), the fruit fly *Drosophila melanogaster* (Dm), the gymnosperm *Ginkgo biloba* (Gb), *Homo sapiens* (Hs), the filamentous green alga *Klebsormidium flaccidum* (Kf), the liverwort *Marchantia polymorpha* (Mp), the sea anemone *Nematostella vectensis* (Nv), the moss *Physcomitrella patens* (Pp) the ctenophore *Pleurobrachia bachei* (Pb), and the *cyanobacterium Synechocystis* sp. (GluR0). Cartoon from Wudick et al. (2018b)

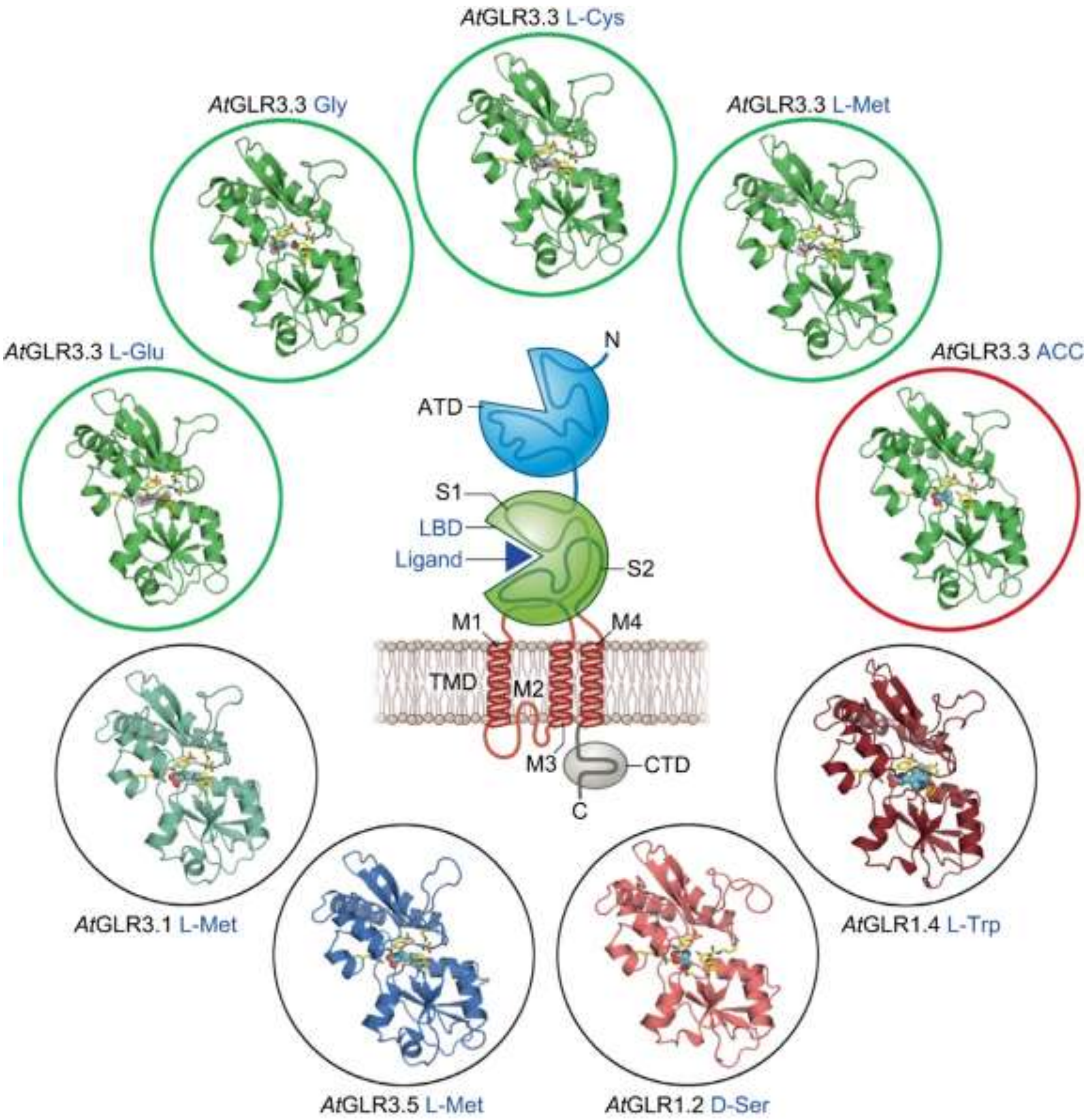

Figure I-5. Predicted architecture of plant glutamate receptor-like channels (GLRs) and structural determinants of the ligand-binding domain. The schematic drawing shows the predicted membrane structure of a single GLR subunit which hosts an extracellular amino-terminal domain (ATD), a ligand-binding domain (LBD) composed of segments S1 and S2, four membrane helices (M1 to M4, one of which – M2 – is not fully transmembrane), and a cytoplasmic tail (CTD), arranged in the order ATD-S1-M1-M2-M3-S2-M4-CTD. The four upper green-lined circles show the structures in ribbon representation of the *At*GLR3.3-LBD bound to different ligands (from the left to the right: L-Glu, Gly, L-Cys and L-Met). The atomic coordinates and structure factors are deposited in the Protein Data Bank, http://www.wwpdb.org (PDB ID codes 6R85, 6R88, 6R89 and 6R8A for the complexes of the *At*GLR3.3-LBD with L-Glu, Gly, L-Cys and L-Met, respectively). The red-lined circle shows that the same *At*GLR3.3-LBD structure is in principle able to accommodate the Aminocyclopropane-1-carboxylic acid (ACC) ligand without any obvious steric hindrance. The remaining four bottom black circles show homology modeling, based on the above-mentioned *At*GLR3.3-LBD structure, of the LBDs of other GLR isoforms. The modeling approach appears to justify the binding of their respective predicted ligands (L-Met for *At*GLR3.1 and *At*GLR3.5, D-Ser for *At*GLR1.2 and L-Trp for *At*GLR1.4) and, more generally, the preference of these isoforms for bulkier hydrophobic amino acid ligands.

Since their discovery, an increasing number of evidence highlighted the GLRs physiological relevance in various aspects of plant life including pollen tube development and plant fertility, seed germination, root development, stomatal aperture, wound response, and plant immune response (Wudick et al., 2018b). However, how GLRs work in plants is still a largely unresolved question. Although structural information can be extrapolated from the high amount of data regarding iGluRs, experimental evidence about the 3D structure of plant GLRs have been unavailable until recently, with the release of the first crystal structures of the LBD of the isoforms *At*GLR3.2 and *At*GLR3.3 (Alfieri et al., 2020; Gangwar et al., 2020) as well as the release of the full-length Cryo-EM structure of the *At*GLR3.4 (Green et al., 2021). These structural data will lead the way to dissect specific molecular features of plant GLRs and unravel their mechanisms of action in the regulation of important plant physiology aspects.

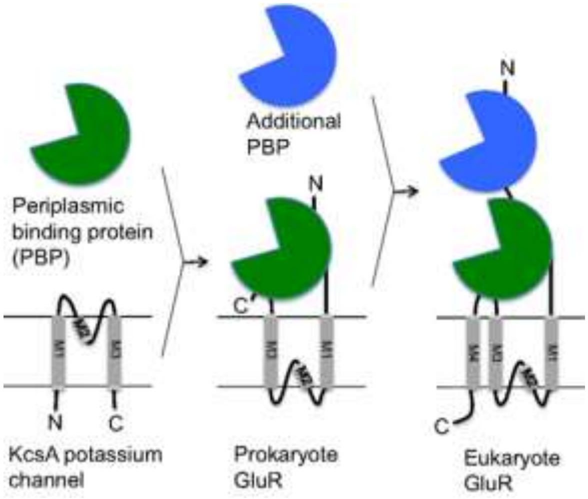

Figure I-6. Proposed origin of eukaryote glutamate receptors. Ligand Binding Domain (LBD, green), Amino Terminal Domain (ATD, blue) and the channel domain (gray). Proposed gene fusione events are indicated by arrows: a fusion event between bacterial periplasmic binding protein and potassium channel would have given rise to a prokaryotic glutamate receptor, which fusion with another periplasmic binding protein would have originate eukaryote glutamate receptors. Cartoon from Price et al. (2012).

I.6. Evolutionary origin of plant GLRs

iGluRs homologous can be identified across all kingdoms of life (Price et al., 2012). As a result of phylogenetic analysis, animal iGluRs and plant GLRs likely diverged from a common ancestor that can be traced back as far as bacteria, rather than being the result of the convergent evolution of genes coding for proteins with a similar structure and function (Chen et al., 1999; Chiu et al., 2002; Price et al., 2012). Bacterial glutamate receptors consist of the channel-forming domain, consisting of only the M1 and M3 transmembrane helices and the partial transmembrane M2 helix forming the P-loop structure, and the LBD, meanwhile the ATD is absent (Chen et al., 1999). The ATD is present only in the eukaryotic glutamate receptors (Chen et al., 1999). The bacterial channel-forming domain (M1-M3) resembles the structure of tetrameric potassium channels (e.g KcsA) with an inverted topology, whose N-terminus and C-terminus exposed normally in the cytosol are instead exposed to the external side of the plasma membrane (MacKinnon, 2003) (**Fig. I-6**). The LBD is characterized by high sequence similarity with the bacterial Periplasmic Binding Proteins (PBPs) (Price et al., 2012), proteins that are produced within the periplasmic space of gram-negative bacteria that bind targets molecules (e.g amino acids, inorganic ions, vitamins, sugars) and mediate their transport into the cytosol through the interaction with membrane-spanning transducers and transporters (Edwards, 2021). Thus, from an evolutionary point of view, these sequence similarities suggest that eukaryotic glutamate receptors may originate from a fusion event between bacterial PBPs and a potassium channel with an inverted topology. Moreover, since the ATD is similar in sequence and structure to the bacterial PBPs, it is likely that a second fusion event has equipped with the ATD the eucaryotic iGluRs (Price et al., 2012) (**Fig. 6**). In plants, *GLRs* would have evolved from an original group called *GLR0* that is present in algae (Chen et al., 2016). During the evolution then, there would have been an increase in the gene copies coding for GLRs. De facto, only one sequence coding for glutamate receptors can be identified in prokaryotes, one and two sequences in the bryophytes *Marchantia polymorpha* (hepatica) and *Physcomitrella patens* (moss), and an explosion of gene redundancy in the vascular plants (De Bortoli et al., 2016). In angiosperms, such an explosion has led to the diversification of four different *GLRs* clades (I, II, III, IV) that are already found in *Amborella trichopoda*, a plant that is placed at the evolutionary basis of modern angiosperms (De Bortoli et al., 2016). Phylogenetic analysis revealed that clade III is phylogenetically more related to the clade 0, and therefore would be more ancient than both clades I and II. Clade IV is not found in brassicales, at which *Arabidopsis* belongs (Chen et al., 2016). Interestingly, the association between the evolution of vascular plants and the increase in the number of GLRs coding genes is likely not simply a correlation, since several GLRs belonging to clade III were found to be expressed in vascular tissues in *Arabidopsis* and rice, where they are involved in the generation and transmission of long-distance electrical and Ca^{2+} signals (Nguyen et al., 2018; Toyota et al., 2018; Yu et al., 2021).

I.7. GLRs at the crossroads of long-distance signalling in plants

The nervous system, a dense network of nerve cells constituting complex electrical circuits, allows animals to operate the fast transmission of information between different parts of the body in the form of electrical signals. Plants do not possess neurons, yet they evolved sophisticated mechanisms to transfer information throughout the plant body including long-distance propagation of electrical, Ca^{2+}, Reactive Oxygen Species (ROS), and hydraulic signals (Christmann et al., 2013; Hedrich et al., 2016; Gilroy et al., 2016). The discovery of electrical signals in plants dates to the end of the XIX century when Burdon-Sanderson observed an action potential (AP – sudden, fast and transitory change of the membrane potential) upon the stimulation of a *Dionaea* leaf. In the XX century, partly thanks to the parallel development of animal electrophysiology, the field of plant electrophysiology expanded rapidly, and electrical signals were recorded in various plant species. The discovery of ion channels, the basis of APs in animals, had to wait until 1984 in plants (Schroeder et al., 1984). Since then, whether electrophysiological properties in animals and plants arise from the activity of a similar set of ion channels was a constant question. Meantime, electrical signals were associated with an onset of numerous physiological effects (From and Lautner, 2006; Li et al., 2021). Citing a few, i) the increase in the respiration rate of electro-stimulated thalli of the hepatica *Conocephalum conicum* (Dziubinska et al; 1989), ii) the increase in the concentration of Jasmonic Acid (JA) and Abscisic Acid (ABA), iii) the enhancement in the *PinII* (*Proteinase Inhibitor II*) gene expression in systemic not-treated leaves of Tomato upon wounding or heating (Herde et al., 1999), and iv) the transient reduction in photosynthesis of systemic leaves of Poplar in response to burning (Lautner et al., 2005). A breakthrough discovery came from Farmer's group, with the demonstration that the wounding of a leaf, by triggering the propagation of electrical signals, induces the accumulation of JA and the expression of genes involved in JA signalling in systemic leaves that share vascular connections (parastichies) with the wounded one in *Arabidopsis* (Mousavi et al., 2013). Moreover, some of the molecular actors involved in the transmission of long-distance electrical signals in plants were identified for the first time, the GLRs. Specifically, Farmer's group observed that in the absence of *At*GLR3.3 and *At*GLR3.6 activity the propagation of electrical signals in systemic tissues was completely abolished, as well as the JA accumulation and the expression of JA-responsive genes (Mousavi et al., 2013). Thus, fifteen years after their discovery the GLRs were found to accomplish a function in plants similar to the one their animal counterparts fulfil in neurons (iGluRs), namely to mediate the transmission of electrical signals over long distances. *At*GLR3.3 and *At*GLR3.6 were then identified to be expressed in different vascular tissues, in phloem and xylem parenchyma cells respectively, demonstrating that both phloem and xylem are involved in the electrical signal transmission (Nguyen et al., 2018). The anatomy of the phloem should theoretically enable the generation and modification of electrical signals (Hedrich et al., 2016). Indeed, phloem-selective recording demonstrated that wounding triggers phloem-propagating electrical signals that are dependent on the activity of *At*GLR3.3 and *At*GLR3.6, with a speed in the range of approximately

1mm/sec (Salvador Recatala, 2016). However, critical anatomical restrictions (i.e., sieve plates constitute a resistance for the diffusion of an electrical signal by reducing the cable surface; companion cells dissipate part of the electrical signals) limit the ability of the phloem to propagate electrical signals over long distances suggesting the existence of a more complex scenario (Hedrich et al., 2016). Whatever the exact mechanisms, the role of GLRs in long-distance signalling seems to be evolutionarily conserved. In tomato, *St*GLR3.5 is required for the transmission of electrical signals and the accumulation of JA in systemic leaves upon the infection with the plant-parasitic roundworm *Meloidogyne incognita* (root-knot nematode) (Wang et al., 2019). In rice, *Os*GLR3.4, which is localized in vascular bundles like other GLRs belonging to clade III, is involved in the expression of the JA-responsive gene *OsJAZ8* in systemic leaves upon root injury (Yu et al., 2021). In the Venus flytrap *Dionaea muscipula*, *DmGLR3.6* is expressed in the trigger hairs of the prey leaf suggesting that *Dm*GLR3.6 activity is likely associated with the trigger hair's sensory function and bending-induced AP generation (Iosip et al., 2020).

I.8. How do plant GLRs work?

At synapses of the animal nervous system, the glutamate (hence after Glu) released by the presynaptic cell is bound by the LBD of glutamate-receptor channels (iGluRs) in the postsynaptic cell, thus promoting the opening of the channels and the influx of Na^+, K^+ and Ca^{2+} ions. The resulting membrane depolarization propagates the nerve impulse (Dingledine et al., 1999; Madden, 2002) (**Fig. I-7a**). Several studies have plausibly adopted the model of regulation/activation of the animal iGluRs for plant GLRs. In plants, the first observation that various amino acids (AA) trigger a membrane depolarization comes from the work of Etherton and Rubinstein in oat coleoptiles in 1978 (Etherton and Rubinstein, 1978). Years later, it was demonstrated in *Arabidopsis* that glutamate and glycine induce a transient membrane depolarization that is accompanied by a large change in $[Ca^{2+}]_{cyt}$ due at least in part to a Ca^{2+} influx across the plasma membrane (Dennison and Spalding, 2000). Moreover, patch-clamp studies in *Arabidopsis* protoplasts revealed that glutamate can increase cation currents (Na^+, Ca^{2+}) in the plasma membrane of plant cells (Demidchik et al., 2004). The sensitivity of these Glu-induced cation currents to typical blockers of non-selective cation channels (La^{3+}, Gd^{3+}, quinine) suggested that these currents were the results of the activity of one or more types of non-selective cation channels (Demidchik et al., 2004). Genetic evidence found that the *At*GLR3.3 activity regulates both the membrane depolarization and the $[Ca^{2+}]_{cyt}$ increase in response not only to glutamate but also to other 5 AAs (Glycine, Cystein, Asparagine, Serine, Alanine) in *Arabidopsis* root cells, responses that are completely abolished in *glr3.3* knock out mutants (Qi et al., 2006; Alfieri et al., 2020) (**Fig. I-7b**). This evidence supports that GLRs activity regulates the ionic responses to Glu and other AAs in plants, reinforcing the hypothesis that plant GLRs may work as animal iGluRs but with a broader agonist profile (Qi et al., 2006; Alfieri et al., 2020). A series of works demonstrated later that GLRs can act as ion channels. Tapken and Hollman replaced the pore domain of an animal iGluR with the pore domain of seventeen different *Arabidopsis* GLRs and expressed these chimaeras in *Xenopus* oocytes. They found that the pore domains of *At*GLR1.1 and *At*GLR1.4 mediate the influx of Na^+, K^+ and Ca^{2+} ions upon Glu treatment (Tapken and Hollman, 2008). The Ca^{2+}-permeability was demonstrated for different GLRs (e.g *Pp*GLR1, *At*GLR3.2, *At*GLR3.3, *At*GLR3.1/*At*GLR3.5, *At*GLR3.4, *At*GLR3.6, *Os*GLR2.1) (Vincil et al., 2012; Kong et al., 2016; Ni et al., 2016; Ortiz-Ramirez et al., 2017; Wudick et al., 2018a; Shao et al., 2020; Gangwar et al., 2021). The release of the crystal structures of the two plant isoforms *At*GLR3.2 and *At*GLR3.3 provided a considerable leap forward in the understanding of the mechanism of action of plant GLRs (Alfieri et al., 2020; Gangwar et al., 2020). *In vitro* binding experiments performed on *At*GLR3.3-LBD revealed its ability to bind and accommodate several amino acids with affinities in the µM range (L-Cys, L-Met, L-Glu, L-Ala, L-Asn, L-Ser, Gly) (Alfieri et al., 2020). Four solved crystal structures of the *At*GLR3.3-LBD in complex with L-Glu, Gly, L-Cys and L-Met were released (**Fig. 5**). This promiscuity characterizes the *At*GLR3.3-LBD from the LBD of prokaryotic and other eukaryotic iGluRs where a restricted preference for 1 or 2 L-AA is usually observed (Alfieri et al., 2020). Importantly, *in vitro* binding affinities mirror the different extents of $[Ca^{2+}]_{cyt}$ increases evoked by different amino acids that I recorded in *Arabidopsis* root during my PhD (Alfieri et al., 2020). Specifically, at 50 µM L-Cys was more effective than L-Glu and Gly in triggering the $[Ca^{2+}]_{cyt}$ increase, as well as *in vitro* the *At*GLR3.3-LBD affinity for L-Cys is higher than L-Glu and Gly (Alfieri et al., 2020). Structural data of *At*GLR3.2 and modelling analyses predict that other *Arabidopsis* GLRs also show 'ligand promiscuity'. As an example, D-Ser or bulkier hydrophobic AAs can be potentially accommodated by the LBD of *At*GLR1.2, *At*GLR1.4, and *At*GLR3.1/*At*GLR3.5, and it was found that the non-proteinogenic amino acid 1-Aminocyclopropane-1-Carboxylic Acid (ACC) is another possible *At*GLR3.3 ligand (**Fig. 5**) (Grenzi et al., 2021b; Mou et al., 2020). Recently, the first full-length cryo-EM structure of the *At*GLR3.4 solved with the LBD bound to L-Glu was reported (Green et al., 2021). Notably, the *At*GLR3.4-ATD was found to be bound to glutathione (GSH) and a significant GSH-induced potentiation of L-Glu-induced *At*GLR3.4 currents was observed in the COS-7 mammalian cells used as a heterologous system where express the channel (Green et al., 2021). A modelling approach revealed that GSH-induced conformational changes, due to the GSH binding to the ATD of the *At*GLR3.4, might contribute to the gating of the channel. These conformational changes would be made possible by a strong connection between the ATD and LBD which ensures that conformational changes in the ATD are allosterically transmitted to the LBD, an interaction that appears to be highly specific to plant GLRs (Green et al., 2021). Overall, these pieces of evidence highlight how plant GLRs are indeed amino acid-receptors. However, an outstanding question is how GLRs are activated and regulated *in planta*, and in particular in long-distance signalling events. *In Arabidopsis*, simultaneous measurements of both the surface leaf potential and $[Ca^{2+}]_{cyt}$ revealed that systemic wounding-induced electrical signals are associated with propagating

Ca^{2+} waves, of which the maximum Ca^{2+} increase temporally follows the depolarization (Nguyen et al., 2018). Like systemic electrical signals, propagating Ca^{2+} waves are dependent on the activity of *At*GLR3.3 and *At*GLR3.6 (Nguyen et al., 2018; Toyota et al., 2018; Shao et al., 2020).

In analogy with iGluRs activation, we can foresee that in plants, mechanical wounding or insect chewing might induce the release of Glu or other AAs in the apoplast thus activating, through direct binding, the GLRs with a consequent Ca^{2+} influx into the cytosol (**Fig. I-7c**). This scenario is supported by data showing that wounding triggers the accumulation of Glu in the apoplast of the wounded leaf (Toyota et al., 2018), and that treatment of *Arabidopsis* leaves or roots with a high amount of glutamate (50-100 mM) induced propagating long-distance Ca^{2+} waves dependent on the activity of both *At*GLR3.3 and *At*GLR3.6 (Toyota et al., 2018; Shao et al., 2020; Moe-Lange et al., 2021). We must say that the model is complicated by localization data of *At*GLRx-Venus chimeric proteins. *At*GLR3.1- and *At*GLR3.3-VENUS chimeric proteins localize at the ER in the xylem contact cells and in the phloem cells, respectively, meanwhile the *At*GLR3.6-Venus localizes at the tonoplast (Nguyen et al., 2018). These localization data hardly reconcile with a model in which plant GLRs are activated by the binding to Glu (and other AAs) in the apoplast, but artefacts due to the use of chimeric proteins cannot be excluded. Moreover, it is not known if the activation of GLRs in systemic tissues is preceded by an increase of apoplastic Glu and that this event is required for the downstream GLR-mediated responses. One plausible alternative mechanism responsible for the systemic GLRs activation has been called the ‘squeeze cell hypothesis’, in which rapid axial changes in xylem hydrostatic pressure, occurring for example in response to wounding, lead to radially dispersed pressure changes that activate the GLRs channels (Farmer et al., 2014; 2020). Indeed, it is known that systemically-propagating hydraulic pressure waves depart from the wounding site following the disruption of the tissues (Malone and Stankovic, 1991; Stahlberg and Cosgrove, 1992), and Moe-Lange and colleagues recently reported, in the distal wound signaling, that besides GLRs there is an involvement of mechanosensitive anion channels (Moe-Lange et al., 2021). Nonetheless, it must be reported that already in 1916, Ricca proposed that a chemical agent (Ricca’s factor) transported from the wounding site would be responsible to initiate systemic electrical signals (Ricca, 1916). Mathematical modelling concluded that hydraulic waves can potentially sustain the systemic mass flow of a chemical agent through the xylem, explaining available experimental data (Blyth and Morris, 2019). If so, this would suggest that Glu may be a prime candidate for Ricca’s factor (Blyth and Morris, 2019).

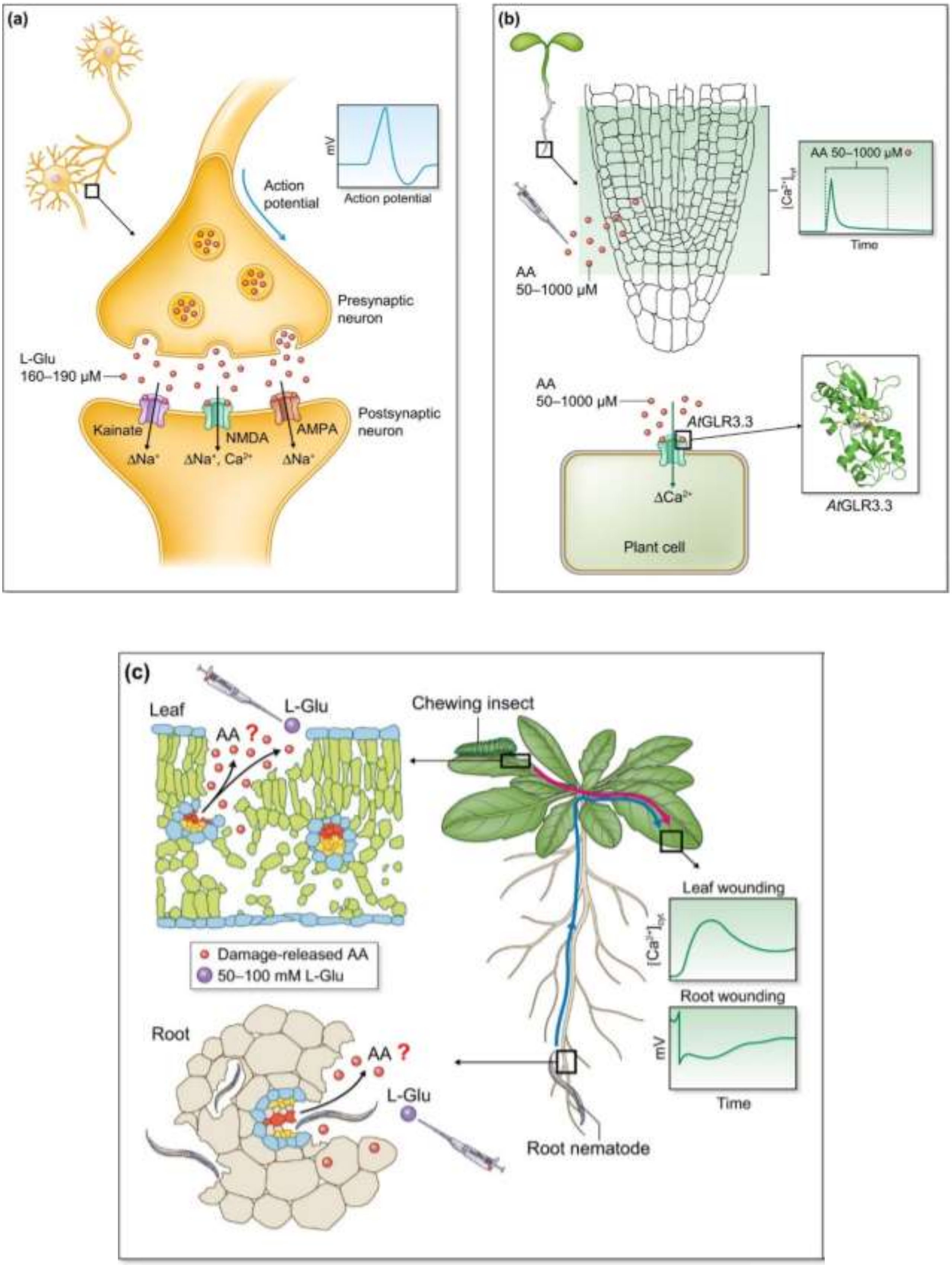
(a)
Action potential
mV
Action potential
Presynaptic neuron
L-Glu 160–190 µM
Kainate
NMDA
AMPA
Postsynaptic neuron
ΔNa⁺
ΔNa⁺, Ca²⁺
ΔNa⁺
(b)
AA 50–1000 µM
[Ca²⁺]cyt
AA 50–1000 µM
Time
AA 50–1000 µM
AtGLR3.3
ΔCa²⁺
Plant cell
AtGLR3.3
(c)
Leaf
AA ?
L-Glu
Chewing insect
Damage-released AA
50–100 mM L-Glu
Leaf wounding
[Ca²⁺]cyt
Root wounding
mV
Time
Root
AA ?
L-Glu
Root nematode

Figure I-7. Functional comparison of iGluRs and glutamate receptor-like channels (GLRs) activation in animal and plant cells. (a) The accepted model of iGluR activation mechanism in an animal synapse. An action potential in the presynaptic neuron triggers the release of Glu (µM range of concentrations) (Dzubay & Jahr, 1999) with the following activation of the plasma membrane-localized Kainate, NMDA and AMPA receptors in the postsynaptic neuron, allowing the passage of sodium (Na^+) and calcium (Ca^{2+}). **(b)** In the plant root tip cells, exogenous administration of L-Glu and other amino acids (AA) in a µM concentration range (50–1000 µM with a maximum response to 500 µM) triggers a transient increase in the free cytosolic Ca^{2+} concentration that in Arabidopsis is dependent on the presence of the *At*GLR3.3 isoform (for which the *in vitro* K_d for L-Glu is 2.2 µM). **(c)** Leaf and root wounding triggers long-distance surface potential depolarizations and free cytosolic Ca^{2+} increases that are largely dependent on clade III GLRs. Likewise, chewing insects trigger depolarization and Ca^{2+} waves from leaf to leaf, and root nematode attack elicits a depolarization wave from root to shoot. The presented model would predict that local wounding (mechanical or resulting from the interaction with pathogens) induces a local AA release that activates the GLR receptors. In support of this, the local administration of 50–100 mM L-Glu (a concentration 1000-fold higher than the one required in root tip cells) to wounded tissues (leaf or root) triggers long-distance Ca^{2+} waves. Whereas the local release of L-Glu or other amino acids in response to wounding can indeed activate the GLRs, the mechanism of their activation in distant vascular tissues is not yet defined.

I.9. A plethora of tools for the study of Ca^{2+} dynamics in vivo

The study of Ca^{2+} dynamics *in vivo* is made possible by a vast repertoire of Ca^{2+} imaging techniques. In plants, the first studies on *in vivo* Ca^{2+} dynamics (Bush and Jones, 1987; McAinsh et al., 1990; Gilroy et al., 1991) were based on the use of Ca^{2+}-sensitive dyes developed by Roger Tsien in 1980 (Tsien, 1980). Ca^{2+}-sensitive dyes paved the way to make fundamental discoveries in the important field of Ca^{2+} signalling, yet they are characterized by critical limitations: (i) they need to be loaded or injected into the cells, which can lead to an inhomogeneous amount of dye in different cells; (ii) their subcellular localization cannot be easily controlled with a tendency to be compartmentalized and eventually extruded from the cell in long-term experiments; (iii) they are by definition Ca^{2+}-buffers, and an excessive loading can affect physiological functions by binding intracellular Ca^{2+} (Paredes et al., 2008; Grenzi et al., 2021a). To overcome these disadvantages, the plant scientific community has turned toward the use of Genetically Encoded Calcium Indicators (GECIs) (Pérez Koldenkova and Nagai, 2013). The birth of GECIs originates from the discovery of aequorin, a calcium-sensitive bioluminescent protein that was isolated from the jellyfish *Aequorea Victoria* (Shimomura et al., 1962). As Shimomura wrote, "*Aequorin is an extraordinary protein that stores a large amount of energy and releases the energy when calcium is added*" (Shimomura, 2005). Aequorin is a holoprotein of 22-KDa composed of two units, the apoprotein called apoaequorin and the prosthetic group called coelenterazine. The functional holoprotein reconstitutes spontaneously in the presence of molecular oxygen. Apoaequorin contains three EF-hands motives that bind to Ca^{2+} ions. When aequorin binds to Ca^{2+} ions, it undergoes a conformational change and displays oxygenase activity, thus coelenterazine is converted into excited coelenteramide that is set free from the complex with carbon dioxide. The relaxation of the excited coelenteramide to the ground state leads to the release of energy, of which a part is released in the form of blue light ($\lambda = 469$ nm) that can be detected with a luminometer or a high-sensitivity CCD or CMOS camera (Mithofers and Mazars, 2002). From its mechanisms of action, it appears clear that a big advantage of aequorin is that it has no need to be excited with fluorescent light. In its first biological application in 1967, aequorin was microinjected in muscle fibres of barnacle where it allowed to monitor Ca^{2+} signals (Ridgway and Ashley, 1967). Years later, the knowledge of the aequorin gene and of its coding sequence (Prasher et al., 1985), allowed to recombinantly express the protein in cells and tissues of different organisms and to generate transgenic organisms stably expressing the protein. The pride of the first transgenic multicellular organisms goes to plant biology, with the generation of *Nicotiana plumbaginifolia* plants stably expressing the aequorin (Knight et al., 1991). Aequorin has been largely used to study Ca^{2+} dynamics in plants, also because its use enables the estimation of absolute Ca^{2+} concentrations (Grenzi et al., 2021a). However, no system is spurious by limitations and aequorin is no exception. Among the limitations, the most tedious is the low quantum yield (Φ, a measure of the efficiency of photon emission that is defined by the ratio between the number of photons emitted and the number of photons absorbed). To generalize, aequorin is characterized by the fact that the number of emitted photons per protein that bind Ca^{2+} is low, making the aequorin signals detectable only when there is the reaction of thousands of proteins (Baubet et al., 2000). Thus, researchers were prompted to explore a new class of GECIs. In nature, the increase of the quantum yield of bioluminescent processes is achieved through the transfer energy of the excited coelenterazine to fluorescence molecules as the green fluorescent protein (GFP) (Baubet et al., 2000). That is exactly why *Aequorea victoria* emits green light instead of blue light, the excited coelenterazine energy excites the GFP that emits green light (λ = 509 nm) when returns to its ground state (Shimomura, 2005). In most cases, the new generation of GECIs is based on the direct use of fluorescent proteins, specifically, GFP and its spectral variants (e.g. CFP, YFP, Venus), fused to a calcium-binding protein that reversibly affects the spectral properties of the associated fluorescent protein upon the binding of Ca^{2+} ions. GECIs, being made of fluorescent proteins, are characterized by a higher quantum yield than the aequorin which makes them easier to be detected. GECIs usage require an illumination system that excites the fluorescent proteins. I refer the reader to a review we have recently published for a general overview of GECIs development, history, and applications (Grenzi et al., 2021a). In the next sections, I'll introduce general characteristics of GECIs exploited in the experiments reported in this thesis.

I.10. Yellow Cameleon – A FRET-based Ratiometric Sensor

The Yellow Cameleon (YC) is a fluorescence Ca^{2+} biosensor based on the physical phenomenon of the Forster Resonance Energy Transfer (FRET) that describes the transfer of the excitation energy between two molecules, one acting as an energy donor and the other one as an energy acceptor. FRET can occur when (i) the emission spectra of the donor it is partially overlapped to the excitation spectra of the acceptor and (ii) acceptor and donor are at a distance ranging from 2 nm to 10 nm. In the Yellow Cameleon, the donor is a Cyan Fluorescent Protein (CFP) and the acceptor is a Yellow

Fluorescent Protein (YFP or cpVenus). The CFP and YFP are linked by a bridge made by the Ca^{2+}-binding protein Calmodulin (CaM) and the CaM-binding peptide (M13). When the four EF-hands motives of CaM bind to Ca^{2+} ions, the interaction of CaM with M13 is promoted and the subsequent conformational change leads to the approaching of the CFP to the YFP. As a result, since the FRET efficiency depends on the distance between the donor and the acceptor, there is an increase in the FRET efficiency. This means that when the CFP is excited (λ = 440 nm) decreases its emission intensity (λ = 440 nm) because part of the energy is transferred to the YFP, that in turn increases its emission intensity (λ = 530 nm). Thus, an increase in the FRET efficiency is linked to an increase in the Ca^{2+} concentration, which is directly proportional to the ratio between YFP and CFP emissions (Miyawaki et al., 1997; Krebs et al., 2012). The Yellow Cameleon is defined as a ratiometric sensor since its readout is based on the detection of the emissions of two fluorescence proteins and, therefore, the ratio between them. Ratiometric sensors possess many advantages: (i) the calculated Ca^{2+} increase relies on the ratio increase only, avoiding artefacts due to protein abundance (e.g., it is possible to compare Ca^{2+} levels between different genetic backgrounds in which the expression level of the protein can be different); (ii) a change of the microscope focus does not alter the readout of the ratio; (iii) changes of cellular pH, in a physiological range, have only mild effects on the indicator readout (Grenzi et al., 2021a) (**Fig. I-8a**)

I.11. R-GECO1, GCaMP3, ER-GCaMP6-210 – Intensiometric Sensors

R-GECO1 is a GECI based on a Red-Fluorescent Protein (RFP). It is made of a circularly permutated RFP (mApple) linked to both CaM and M13 peptides at its C- and N- termini, respectively. The excitation spectrum shows the maximum peak of absorption at λ = 561, whereas the emission spectrum has a maximum peak at λ = 600 (Zhao et al., 2011) (**Fig I-7b**). GCaMP3 is a GECI based on the circularly permutated GFP and, as the R-GECO1, has the M13 linked to the N-terminus and the CaM linked to the C-terminus. The excitation spectrum for the GCaMP3 shows a maximum peak of absorption at λ = 480 and the emission spectrum has a maximum peak at λ = 510 (Tian et al., 2009) (**Fig I-7c**). The mechanisms of action of the two GECIs is the same. In the absence of Ca^{2+}, the chromophore of both cpGFP and cpmApple is exposed to water, and it is in a protonated state with a minimal emission of fluorescence even if excited with the proper wavelength. When Ca^{2+} ions bind to the EF-hand motives of the CaM, the interaction of CaM with M13 promotes a conformational change that prevents water molecules from accessing the chromophore. As a result, there is a switch in the protonation state of the chromophore (deprotonation) that change its spectral properties and lead to a brighter fluorescence (Zhao et al., 2011; Tian et al., 2009). The generation of Ca^{2+} indicators with a low affinity for Ca^{2+}, combined with the use of specific targeting sequences, allows the measurement of Ca^{2+} dynamics in subcellular compartments in which the Ca^{2+} concentration is too high (µM) to be read by GECIs normally used in the cytosol which have an affinity for Ca^{2+} in the range of nM (Grenzi et al., 2021a; Resentini et al.,2021). The ER-GCaMP6-210 is an ER-localized low-affinity (*Kd* = 210 µM) Ca^{2+} variant of the intensiometric single fluorophore-based GCaMP6, that is based on the circularly permutated GFP as the GCaMP3 (Resentini, Grenzi et al., 2021) (**Fig I-7d**). Advantages of intensiometric sensors in respect to ratiometric ones are: (i) they can be used with a simple microscope setup; (ii) they are characterized by a high sensitivity and a high signal increase upon Ca^{2+} detection that allows measurements of Ca^{2+} dynamics in adult plant with low magnification objectives. Critical limitations of intensiometric sensors are: (i) the measured signal can be easily affected by a microscope focus changes; (ii) as all the fluorescent proteins are sensitive to pH, pH changes can affect the readout (in this regard, I carried out demonstrative experiments that are reported in Grenzi et al., 2021a); (iii) the expression level of the sensor can lead to different levels of emitted light, making them inappropriate to measure the resting Ca^{2+} levels among different genetic backgrounds at resting (Grenzi et al., 2021a).

I.12. Measurement of glutamate dynamics in vivo

The central role of Glu in neurotransmission prompted neurobiologists to develop technologies to visualize *in vivo* the release of Glu from neurons. In 2013, Loren Looger's lab generated the GFP-based glutamate-sensor iGluSnFR (Marvin et al., 2013). iGluSnFR is made of a circularly permutated GFP fused with the two halves of the bacterial periplasmic glutamate binding protein (GltI) at its N- and C-termini. When the GltI binds to Glu, the protein undergoes to a conformational change that leads to the deprotonation of the chromophore and to an increase in the emitted fluorescence. As the GCaMP3, the excitation spectrum shows a maximum peak of absorption at λ = 480 and the emission spectrum has a maximum peak at λ = 510. Motivated by the increasing evidence of the importance of GLRs in plant physiology, plant biologists transferred the iGluSnFR technology in plants. The iGluSnFR sensor was successfully used by Toyota and colleagues, which generated *Arabidopsis* plants expressing the iGluSnFR sensor targeted to the apoplast and measured the accumulation of Glu in this compartment in a wounded leaf (Toyota et al., 2018) (**Fig. I-8e**).

A schematic representation of genetically encoded fluorescence biosensors used in this work, with their relative subcellular localization, is shown in **Fig. I-8**.

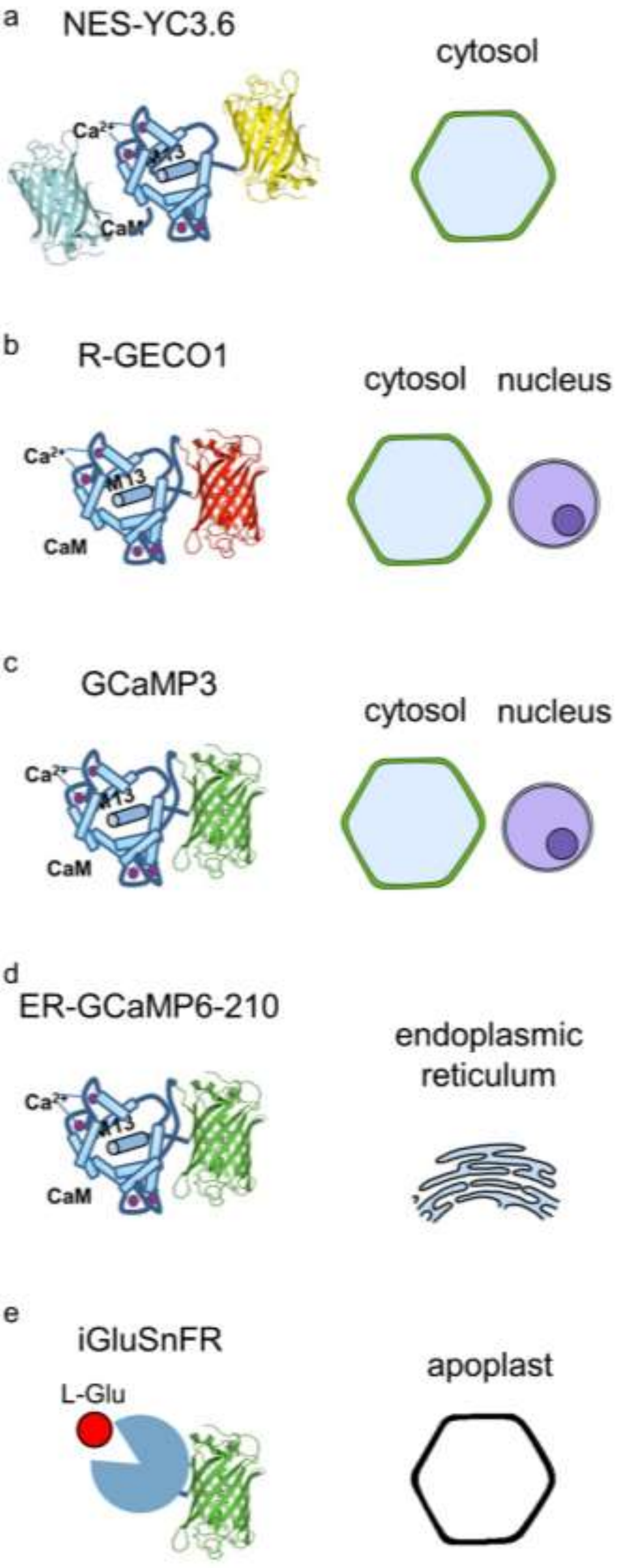
a
NES-YC3.6
Ca2+
M13
CaM
cytosol
b
R-GECO1
Ca2+
M13
CaM
cytosol
nucleus
c
GCaMP3
Ca2+
M13
CaM
cytosol
nucleus
d
ER-GCaMP6-210
Ca2+
M13
CaM
endoplasmic reticulum
e
iGluSnFR
L-Glu
apoplast

Type	ratiometric
Excitation (nm)	440
Emission (nm)	480/530
In vitro Kd (nM)	250

Type	intensiometric
Excitation (nm)	561
Emission (nm)	600
In vitro Kd (nM)	482

Type	intensiometric
Excitation (nm)	488
Emission (nm)	515
In vitro Kd (nM)	542

Type	intensiometric
Excitation (nm)	488
Emission (nm)	515
In vitro Kd (µM)	210

Type	intensiometric
Excitation (nm)	488
Emission (nm)	515
In vitro Kd (µM)	33

Figure 8-I. **Overview of genetically encoded fluorescence biosensors used in this work with their relative subcellular localization**. (a) Nuclear Export Signal (NES)-YC3.6 Ca^{2+} indicator. (b) R-GECO1 Ca^{2+} indicator. (c) GCaMP3 Ca2+ indicator. (d) Endoplasmic Reticulum (ER)-GCaMP6-210 Ca2+ indicator. (e) iGluSnFR L-Glu indicator.

Aim of the thesis

Plants are sessile organisms that evolved mechanisms to react to ever-changing environmental conditions and harmful stresses. Local damages trigger inducible defence mechanisms that are often also induced systemically in organs that, however, have not been damaged. In *Arabidopsis thaliana*, wounding and herbivore feeding trigger long-distance variation potentials (VPs) and Ca^{2+} waves that propagate from the injured leaf to systemic organs. The genetic ablation of the *At*GLR3.3 and *At*GLR3.6, as well as of the *At*GLR3.3 and *At*GLR3.1, leads to the abolishment of both wound-induced VPs and Ca^{2+} waves propagation (Mousavi et al., 2013; Nguyen et al., 2018; Toyota et al., 2018). *At*GLR3.3 and *At*GLR3.6 are expressed in different vascular tissues (phloem and xylem parenchyma cells, respectively), suggesting that both tissues are synergistically involved in the VPs and Ca^{2+} waves propagation (Nguyen et al., 2018).

GLRs are homologous of animal ionotropic glutamate receptors (iGluRs) (Lam et al., 1998; Lacombe et al., 2001; Chiu et al., 2002) which are ligand-gated Ca^{2+}-permeable ion channels mediating the excitatory neurotransmission in the central nervous system of vertebrates. iGluRs are activated by the binding of aminoacidic neurotransmitters (i.e., L-Glu, Gly, D-Ser). The binding to the LBD induces a conformational change leading to the opening of the channel (Traynelis et al., 2010). Despite the homology with animal iGluRs, little is known about the mechanism of how plant GLRs are activated *in planta*. A key question in the understanding of plant GLRs physiology is whether the binding of amino acids to their LBD is necessary or not for their activation, in both local and systemic responses. On this important aspect some contrasting pieces of evidence have been reported: (i) an *in vitro* binding assay demonstrated that the *At*GLR3.3-LBD binds several AAs with an affinity in the low micromolar range (Alfieri et al., 2020); (ii) the administration of a high amount of L-Glu (50-100 mM) to a wounded leaf triggers long-distance propagating Ca^{2+} waves that require the *At*GLR3.3 activity (Toyota et al., 2018; Shao et al., 2021). Indeed, the requirement of such a high concentration of L-Glu to induce GLRs-dependent systemic responses odds with the *in vitro* binding affinities reported for the *At*GLR3.3-LBD (mM vs. µM). Moreover, we must say that in root tip cells the *At*GLR3.3 is activated at L-Glu concentration as low as 50 µM (Alfieri et al., 2020). The recently released crystal structures of the *At*GLR3.2-LBD and *At*GLR3.3-LBD (Gangwar et al., 2020; Alfieri et al., 2020) represent a rational tool to define the functional role of GLR ligands which is still unclear.

In such a scenario, the goal of the present study was to investigate whether it is possible to demonstrated if the "ligand-binding-driven activation" of animal iGluRs works also with plant GLRs, and more importantly to define if the sole activation of GLRs is sufficient to trigger long-distance signaling.

Chapter II. Results and discussion

II.1. Leaf wound triggers leaf-to-leaf $[\text{L-Glu}]_{apo}$ and AtGLR3.3-dependent $[Ca^{2+}]_{cyt/nuc}$ increases

In the seminal work from Farmer's and colleagues, it was reported that *Arabidopsis thaliana* double mutants carrying the *glr3.3* mutation (*glr3.1 glr3.3* and *glr3.3 glr3.6*) are strongly impaired in the wound-induced depolarization and Ca^{2+} increase in systemic leaves (Nguyen et al., 2018), suggesting a key role played by *At*GLR3.3 in this response. Since it was demonstrated that the *At*GLR3.3 binds L-Glutamate (L-Glu) in a physiological range of concentrations (Alfieri et al., 2020), we hypothesized that this isoform is responsible for the sensing of apoplastic L-Glu. In order to confirm if the activity of *At*GLR3.3 is correlated with the presence of apoplastic L-Glu ($[\text{L-Glu}]_{apo}$) *in planta*, we generated *Arabidopsis* wt and *glr3.3-1* plants co-expressing the apoplastic-localized green fluorescent iGluSnFR L-Glu sensor (Marvin et al., 2013; Toyota et al., 2018) with the red-shifted R-GECO1 Ca^{2+} indicator (Zhao et al., 2011; Keinath et al., 2015) (**Fig. 1a,b**). Of note, the analyses of Ca^{2+} dynamics were considered as a proxy for the *At*GLR3.3 activation (Nguyen et al., 2018). With the generated lines we carried out experiments where we wounded one single mature leaf with a tweezer and measured, in the same plant, the fluorescence emitted by both indicators at the level of the entire rosette by performing a dual colour imaging with a stereomicroscope. We thus analyzed the fluorescence changes in the local wounded leaf and in a systemic leaf (**Fig. 1a**). At the wounding site in both the wt and *glr3.3-1* plants a clear increase of $[\text{L-Glu}]_{apo}$ and $[Ca^{2+}]_{cyt}$ occurred almost instantaneously after the injury (**Fig. 1c-h**) with no statistical difference between the two genotypes in terms of maximum response represented as $\Delta F_{max}/F_0$ (**Fig. 1g,h**). When the fluorescence change was analyzed in the systemic leaf, the wt showed a clear increase of both $[\text{L-Glu}]_{apo}$ and $[Ca^{2+}]_{cyt/nuc}$, (**Fig. 1i- n**), whereas the *glr3.3-1* mutant showed a strongly impaired $[Ca^{2+}]_{cyt}$, increase (**Fig 1m)** but with an increase of $[\text{L-Glu}]_{apo}$ that was not statistically different from the wt (**Fig 1n**). We also quantified the speed of the leaf-to-leaf propagation of $[\text{L-Glu}]_{apo}$ and $[Ca^{2+}]_{cyt/nuc}$ increases which was 447 ± 224 µm/sec and 507 ± 340 in wt and *glr3.3-1* plants, respectively. The propagation speed of both $[\text{L-Glu}]_{apo}$ and $[Ca^{2+}]_{cyt/nuc}$ was not statistically different between the two genotypes, showing that the lack of *GLR3.3* impairs the proper elevation of $[Ca^{2+}]_{cyt/nuc}$ but does not affect neither the speed of propagation nor the $[\text{L-Glu}]_{apo}$ increase. These data demonstrated that in distal leaves wounding triggers a $[\text{L-Glu}]_{apo}$ increase that is independent from the activity of *At*GLR3.3. We therefore hypothesized that the systemic $[\text{L-Glu}]_{apo}$ increase upon wounding occurs upstream of *At*GLR3.3 activation which in turn regulates the $[Ca^{2+}]_{cyt/nuc}$ increase. Interestingly, in Nguyen et al. (2018) the wounding of one rosette leaf induced a $[Ca^{2+}]_{cyt/nuc}$ increase only in the systemic leaves sharing a vascular connection (parastichies) to the wounded ones, whereas in our case all true leaves clearly showed a $[Ca^{2+}]_{cyt/nuc}$ elevation. This difference is probably due to the fact that in the previous publication were used older plants (Nguyen et al., 2018).

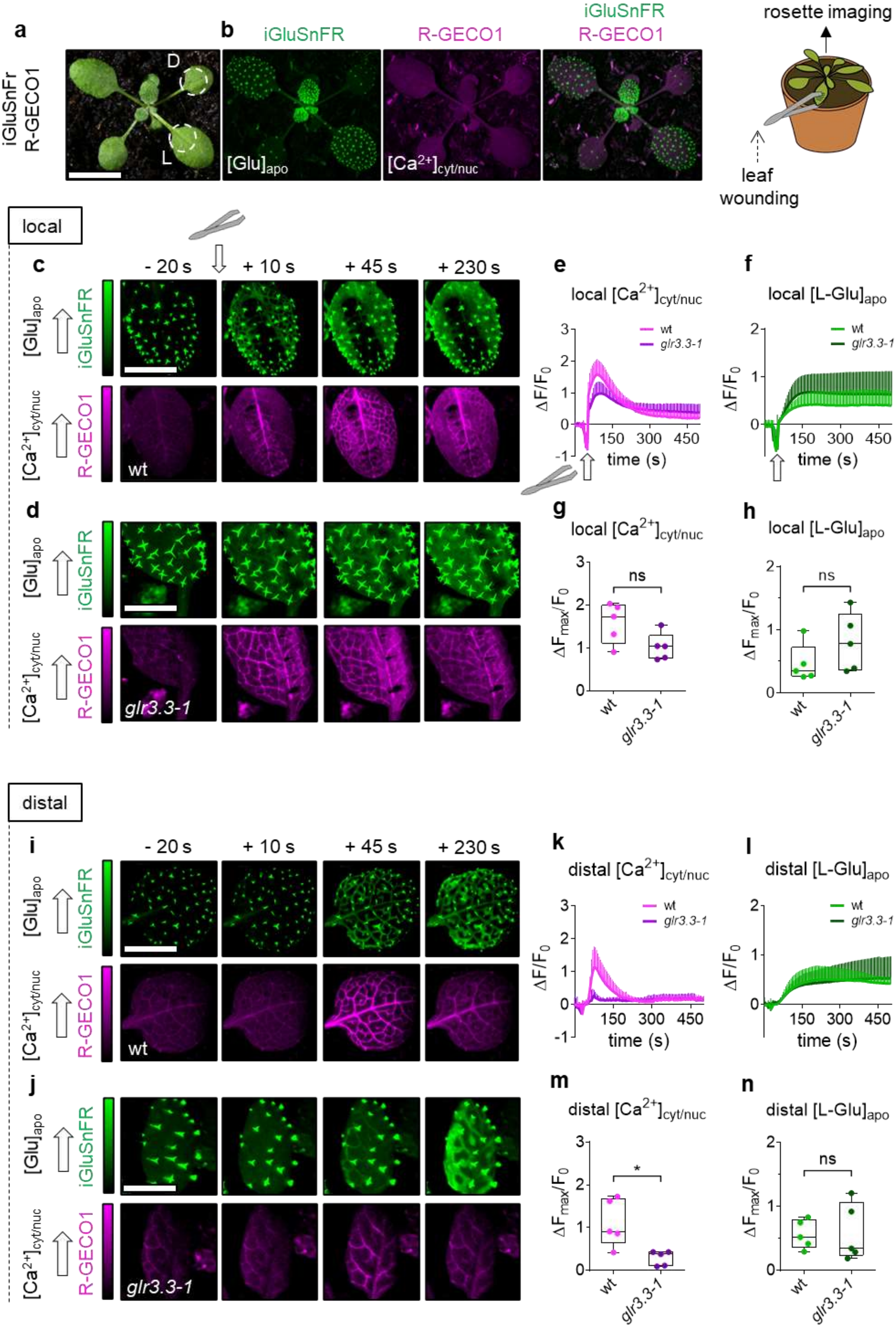
a
iGluSnFr
R-GECO1
D
L
b
iGluSnFR
R-GECO1
iGluSnFR
R-GECO1
[Glu]apo
[Ca2+]cyt/nuc
rosette imaging
leaf wounding
local
c
- 20 s
+ 10 s
+ 45 s
+ 230 s
[Glu]apo
iGluSnFR
[Ca2+]cyt/nuc
R-GECO1
wt
d
glr3.3-1
e
local [Ca2+]cyt/nuc
wt
glr3.3-1
ΔF/F0
time (s)
3
2
1
0
-1
150
300
450
f
local [L-Glu]apo
2
1
0
g
local [Ca2+]cyt/nuc
ns
ΔFmax/F0
h
local [L-Glu]apo
ns
distal
i
j
k
distal [Ca2+]cyt/nuc
l
distal [L-Glu]apo
m
distal [Ca2+]cyt/nuc
*
n
distal [L-Glu]apo
ns

Figure 1. Simultaneous apoplastic L-Glu and cytosolic Ca^{2+} concentration analyses in leaves of wt and *glr3.3-1* adult plants challenged with leaf wound. (a) Bright field image of a representative iGluSnFR x R-GECO1 mature plant and schematic drawing of the experimental design. Scale bar = 7 mm. **(b)** Fluorescence images of a representative iGluSnFR x R-GECO1 mature plant (iGluSnFR green, R-GECO1 magenta). Scale bar = 7 mm. **(c)** Examples of false-colour images illustrate iGluSnFR (green) and R-GECO1 (magenta) in a local wounded leaf (L) of a wt plant. Scale bar = 7 mm. **(d)** Examples of false-colour images illustrate iGluSnFR (green) and R-GECO1 (magenta) in a local wounded leaf (L) of a *glr3.3-1* plant. Scale bar = 7 mm. **(e)** R-GECO1 normalized fluorescence change of the local leaf (L) over the time after its wound (white arrow) in wt and *glr3.3-1* plants. **(f)** iGluSnFR normalized fluorescence change of the local leaf (L) over the time after its wound (white arrow) in wt and *glr3.3-1* plants. **(g)** Maximal peaks of the R-GECO1 fluorescence signal in the local leaf of wt and *glr3.3-1* plants after wound. **(h)** Maximal peaks of the iGluSnFR fluorescence signal in the local leaf of wt and *glr3.3-1* plants after wound. **(i)** Examples of false-colour images illustrate iGluSnFR (green) and R-GECO1 (magenta) in a distal leaf (D) of a wt plant. Scale bar = 7 mm. **(j)** Examples of false-colour images illustrate iGluSnFR (green) and R-GECO1 (magenta) in a distal leaf (D) of a *glr3.3-1* plant. Scale bar = 7 mm. **(k)** R-GECO1 normalized fluorescence change of the distal leaf (D) over the time after wound (white arrow) in wt and *glr3.3-1* plants. **(l)** iGluSnFR normalized fluorescence change of the distal leaf (D) over the time after wound (white arrow). **(m)** Maximal peaks of the R-GECO1 fluorescence signal in the distal leaf of wt and *glr3.3-1* plants after wound. **(n)** Maximal peaks of the iGluSnFR fluorescence signal in the distal leaf of wt and *glr3.3-1* plants after wound. n ≥ 5. Error bars = SD. $^{*}P < 0.05$, ns = not significant *(Student t test)*

II.2 Burn induce systemic increase in $[\text{L-Glu}]_{apo}$ precedes subsequent $[Ca^{2+}]_{cyt/nuc}$ rise

The spatial and temporal resolution offered by the stereomicroscope was not sufficient to establish the temporal hierarchy between $[\text{L-Glu}]_{apo}$ and $[Ca^{2+}]_{cyt/nuc}$ increases. Thus, we designed a protocol to better evaluate systemic responses by performing the multi-parametric imaging at single cells with a high sampling rate. Specifically, we choose to image cells of the flower receptacle in the primary inflorescence of adult *Arabidopsis* plants, imaged with a spinning disk confocal microscope. The Inflorescence of a wt plant was mounted on an imaging chamber and $[\text{L-Glu}]_{apo}$ and $[Ca^{2+}]_{cyt/nuc}$ dynamics of single flower receptacle cells were analyzed after the application of a mechanical stress to one rosette leaf (**Fig. 2a,b**) The distance between the imaged cells and the site of application of the stress was on average 12 ± 1.4 cm. The intensity of the damaging stimulus defines amplitude of the variation potential and the distance at which it can travel (Vodeneev et al., 2015) and, alongside wounding, various mechanical injuries are able to induce VPs (Stahlberg et al., 2006; Opritov et al., 1991; Zimmermann et al., 2009). Burning is one of the most used stimuli to induce VPs in different plant species (Malone et al., 1991; Boari et al., 1993; Stahlberg et al., 1996; Stankovic et al., 1997). We therefore assayed the ability of burning to induce a systemic leaf-to-flower response. Upon leaf-burning both iGluSnFR ($[\text{L-Glu}]_{apo}$) and R-GECO1 ($[Ca^{2+}]_{cyt/nuc}$) fluorescence emissions rose up in the flower receptacle cells. The average time required to see the change of fluorescence was 57 ± 30 sec (**Fig. 2c-e**). Intriguingly, the improved spatial and temporal resolution allowed us to clearly identify that the increase of $[\text{L-Glu}]_{apo}$ occurred before a detectable change in the $[Ca^{2+}]_{cyt/nuc}$ (**Fig. 2f**) that occurred only when the iGluSnFR fluorescence reached a value of $\Delta F/F_0 = 0.11 \pm 0.03$ (**Fig. 2g**). Thus, this latter result supports the hypothesis that in systemic tissues an increase of $[\text{L-Glu}]_{apo}$ may anticipate the rise in $[Ca^{2+}]_{cyt/nuc}$, and also that leaf burning induces a wounding-like systemic response. Therefore, we monitored by qRT-PCR the expression of the Jasmonic Acid (JA) marker gene *JAZ10* (Gasperini et al., 2015) in the primary inflorescence of young bolting plants after the burning of one rosette leaf (**Fig. 2h**). 15 min after burning we detected a 15-fold increase in the *JAZ10* transcript level that progressively decreased at 30 and 60 min (**Fig. 2h**). To orthogonally support this observation we employed the JA-responsive *pJAZ10::GUS* (β-glucuronidase) marker line (Gasperini et al., 2015). Plants were subjected to the burning of one rosette leaf and sampled at 1, 3 and 5 hours to evaluate the activity of the GUS enzyme. The analysis revealed that the leaf-burning triggered an increase in the *pJAZ10::GUS* reporter activity in the primary inflorescence stem

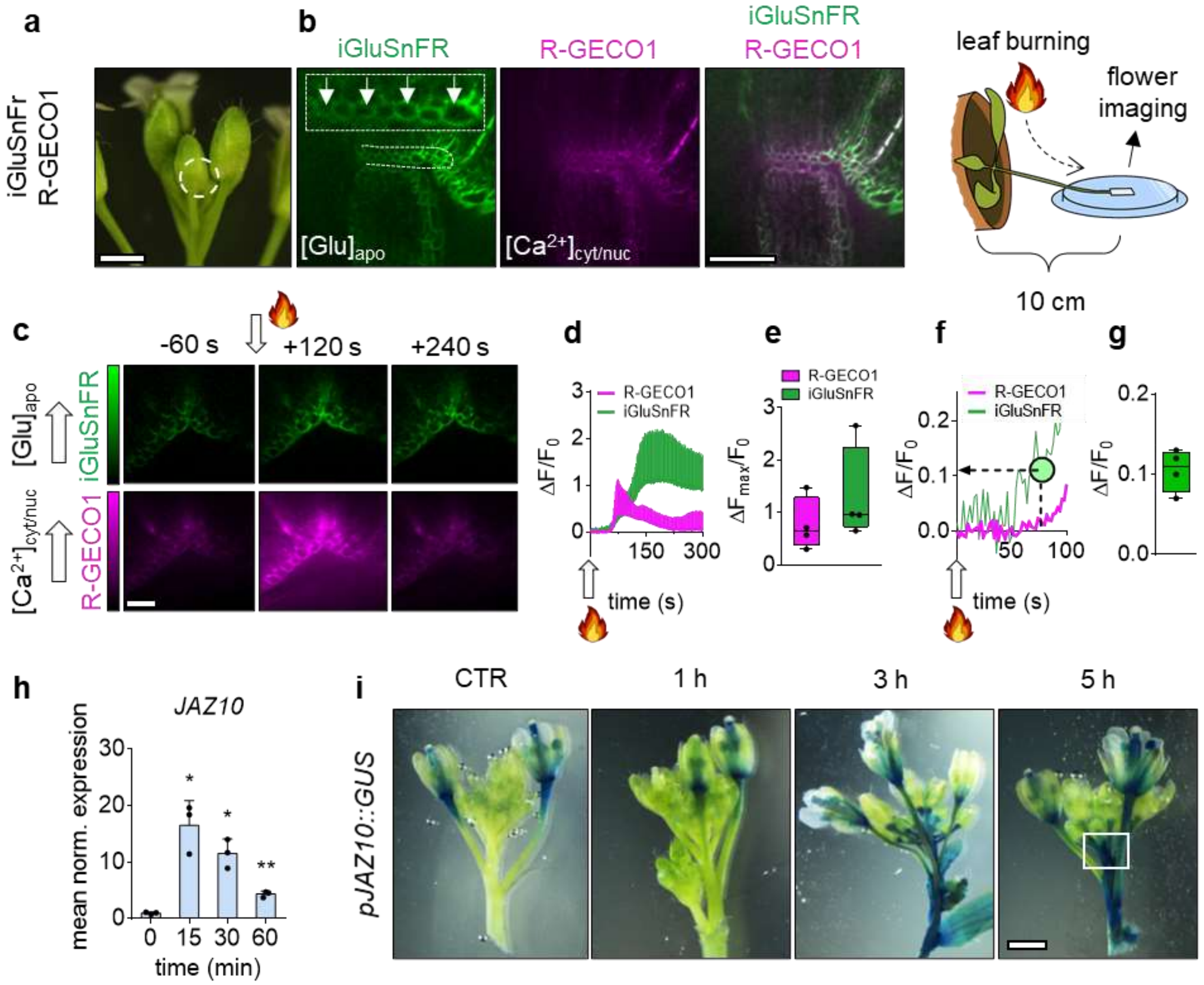

Figure 2. Simultaneous apoplastic L-Glu and cytosolic Ca^{2+} concentration analyses in flowers of wt and *glr3.3-1* adult plants challenged with leaf burn. (a) Bright field image of a representative primary inflorescence of an iGluSnFR x R-GECO1 plant and schematic drawing of the experimental design. Scale bar = 1 mm. **(b)**, False-colour fluorescence images of a representative iGluSnFR x R-GECO1 mature plant (iGluSnFR green, R-GECO1 magenta). Scale bar = 130 µm. The inset is a higher magnification of the flower receptacle. White arrows indicate the cell types chosen to perform the analysis of fluorescence at single cell resolution. **(c)** Examples of false-colour images illustrate iGluSnFR (green) and R-GECO1 (magenta) of the flower receptacle cells in response to the burn of one rosette leaf. Scale bar = 30 µm. **(d)** iGluSnFR and R-GECO1 normalized fluorescence changes of single cells over the time after the burn of one rosette leaf (white arrow). **(e)** Maximal peaks of iGluSnFR and R-GECO1 fluorescence signals in the flower receptacle cells. **(f)** Same as panel **d** but x-axis, y-axis scales, and ranges adjusted. **(g)** Mean normalized iGluSnFR fluorescence change at which an increase of the R-GECO1 fluorescence is observed. **(h)** *JAZ10* gene induction in primary inflorescence after the burn of one rosette leaf. **(i)** Representative GUS staining (n = 3) for a *pJAZ10::GUS* transcriptional reporter in the primary inflorescence before and after the burning of one rosette leaf. Scale bar = 1 mm. n ≥ 3. Error bars = SD. *$^*P < 0.05$, $^{**}P < 0.005$ (Student t test).*

and in the young flowers (**Fig 2.i**). Overall, these results show that in response to leaf-burning there is a systemic accumulation of glutamate in receptacle cells of inflorescence buds that precedes the $[Ca^{2+}]_{cyt/nuc}$ rise and the subsequent upregulation of the *JAZ10* marker gene. The data also suggest that the $[Ca^{2+}]_{cyt/nuc}$ increase occurs when the apoplastic glutamate concentration reaches a given threshold, reported by the $[L\text{-}Glu]_{apo}$ sensor with a fluorescence increase of $\Delta F/F_0 = 0.11 \pm 0.03$ (**Fig. 2g**). The ability of plant GLRs to bind several AAs, including L-Glu, was demonstrated for at least two GLRs isoforms (*At*GLR3.3 and *At*GLR3.4) (Alfieri et al., 2020; Green et al., 2021). Since *At*GLRs (*At*GLR3.3 and *At*GLR3.6) are known to regulate leaf-to-leaf $[Ca^{2+}]_{cyt}$ waves and systemic JA accumulation in response to a mechanical injury (Mousavi et al., 2013, Nguyen et al., 2018, Toyota et al., 2018, Shao et al., 2021), we can speculate that in response to wounding and burning *At*GLRs are activated in systemic tissues through the binding with an AA ligand and in turn participate in the generation of both $[Ca^{2+}]_{cyt}$ and JA responses. Since JA is known to control the development of inflorescence and flowers (Yuan et al., 2015) and *pJAZ10::GUS* reporter activity was already detectable in mature flowers before the treatment (**Fig. 2i**), additional JA marker genes characterized by a lower expression in flowers should be verified (eg. *JAZ2*, *JAZ3*, *JAZ7*) (Schmid et al., 2005).

II.3. AtGLR3.3 is needed for burn and L-Glu induced $[Ca^{2+}]_{cyt/nuc}$ increase in the phloem cells

The *At*GLRs involvement in the regulation of observed burning-induced $[Ca^{2+}]_{cyt/nuc}$ responses was firstly assessed analysing the expression pattern of *AtGLR3.3* and *AtGLR3.6* genes in the primary inflorescence. GUS staining of *pGLR3.3::GLR3.3-GUS* translational reporter line (Nguyen et al., 2018) revealed the GUS activity in the phloem of the inflorescence stem and flower tissues (**Fig. 3a,b**). In the *pGLR3.6::GUS* transcriptional reporter line (Singh et al., 2016) the GUS staining was observed only in the xylem contact cells of the stem and merely detectable in flower tissues (**Fig. 3c,d**). These data agree with previous reports by which *At*GLR3.3 and *At*GLR3.6 are expressed in the leaf phloem and xylem contact cells, respectively (Nguyen et al., 2018).

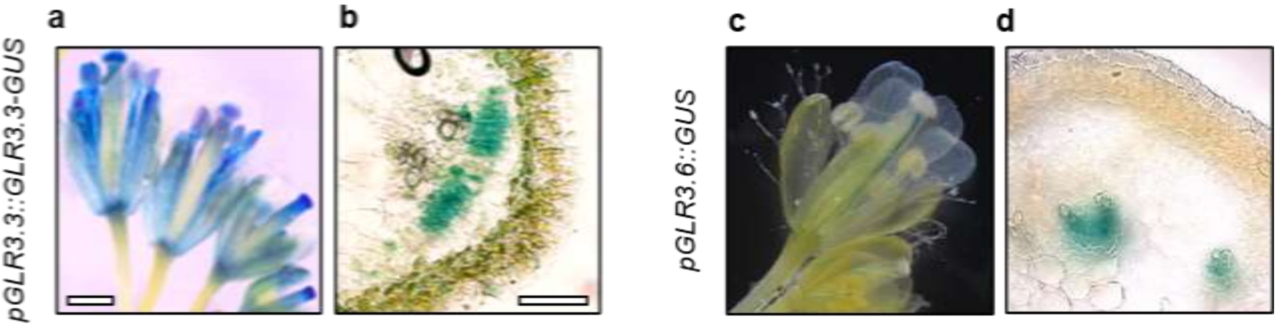

Figure 3. (a) Representative GUS staining of a *pGLR3.3::GLR3.3-GUS* translational reporter line in flowers of the primary inflorescence. Scale bar = 1 mm. **(b)** Representative GUS staining of a *pGLR3.3::GLR3.3-GUS* translational reporter line in the stem transverse section of the primary inflorescence. Scale bar = 150 µm. **(c)** Representative GUS staining of a *pGLR3.6::GLR3.6* transcriptional reporter line in flowers of the primary inflorescence. Scale bar = 1 mm. **(d)** Representative GUS staining of a *pGLR3.6::GLR3.6* transcriptional reporter line in the stem transverse section of the primary inflorescence. Scale bar = 150 µm.

Of note, the analysis of GUS reporter activity showed that only the *At*GLR3.3 is expressed at the level of flower receptacle, whereas the promoter of *AtGLR3.6* was not active, suggesting the lack of *AtGLR3.6* transcript and protein. The RNAseq data mining from Lee et al. confirmed the presence and absence of *AtGLR3.3* and *AtGLR3.6* transcripts in the flower receptacle cells, respectively (**Supplementary Table 1**) (Lee et al., 2018). We therefore hypothesized that *At*GLR3.3 could be the channel responsible for the generation of the $[Ca^{2+}]_{cyt/nuc}$ observed in flower receptacle cells after the leaf-burning potentially activated by the increase of $[L\text{-}Glu]_{apo}$. Being the *At*GLR3.3 expressed in phloem cells of leaves (Nguyen et al., 2018) and stem (**Fig. 3b**), we decided to investigate its role in the genesis of burning-induced $[Ca^{2+}]_{cyt/nuc}$ signals in this specific tissue. The ratiometric Ca^{2+} indicator Yellow Cameleon (YC) 3.6 (Nagai et al., 2004) was selectively expressed in phloem and companion cells of wt and *glr3.3-1* plants using the *SUC2* promoter, which activity is restricted to these tissues (Truernit and Sauer, 1995). The rational of using the Ca^{2+} indicator Cameleon YC3.6 was due to its ratiometric nature thus reducing possible artifacts and offering a reliable measurement also of resting conditions (see below) (Grenzi et al., 2021b). Confocal microscope image analysis of seedlings and leaves from adult plants (**Fig. 4a-c**) and widefield microscopy of flowers (**Fig. 4d**) revealed that the Cameleon fluorescence was specifically present in the vasculature. To better appreciate the specific expression of the indicator to phloem cells we also performed the confocal analysis on a transverse section from the primary inflorescence stem, which confirmed the confined expression of the Cameleon (**Fig.4 e, e'**). The analyses of $[Ca^{2+}]_{cyt/nuc}$ in phloem and companion cells in the receptacle region revealed a clear $[Ca^{2+}]_{cyt/nuc}$ rise in response to leaf-burning, a response that was completely absent in *glr3.3-1* plants (**Fig.5 a, c**). Because $[L\text{-}Glu]_{apo}$ increase anticipates $[Ca^{2+}]_{cyt/nuc}$ in the receptacle region in response to leaf-burning (**Fig.2 f**) and being *At*GLR3.3 able to bind L-Glu (Alfieri et al., 2020), we tested the response to the exogenous administration of L-Glu on the phloem cells of wt and *glr3.3-1* plants. The fact that phloem cells are buried into the stem, live imaging of this tissue is characterized by two main technical limitations: limited optical access and difficulty to perform any chemical treatment. To overcome this issue, we prepared from *pSUC::YC3.6* plants longitudinal sections of the stem inflorescence, which where mounted in the imaging chamber and covered with wet cotton. Given the invasiveness of the procedure, the sections were perfused with an imaging control solution for at least 25 min before testing the effects of L-Glu administration. Samples were then imaged and L-Glu was administered at the indicated time and pulsed for 3 min. The entire experiment was performed in continuous perfusion and L-Glu solution was prepared using the imaging control solution as solvent. When 1mM L-Glu was applied, a rapid $[Ca^{2+}]_{cyt/nuc}$ transient was observed in phloem cells of wt plants (**Fig. 5d-f**). On the contrary, the same treatment was not able to induce any detectable change in phloem cells $[Ca^{2+}]_{cyt/nuc}$ of *glr3.3-1* plants (**Fig. 5d-f**).

Overall, we demonstrated that the genesis of $[Ca^{2+}]_{cyt/nuc}$ signals induced by leaf-burning and L-Glu administration are both dependent on the activity of *At*GLR3.3. The correlation of these results with data reported above (**fig. 2d-g**) let us to hypothesize that leaf-burning induces the apoplastic accumulation of L-Glu, and possibly other AAs, that triggers a phloem $[Ca^{2+}]_{cyt/nuc}$ response through the activation of *At*GLR3.3.

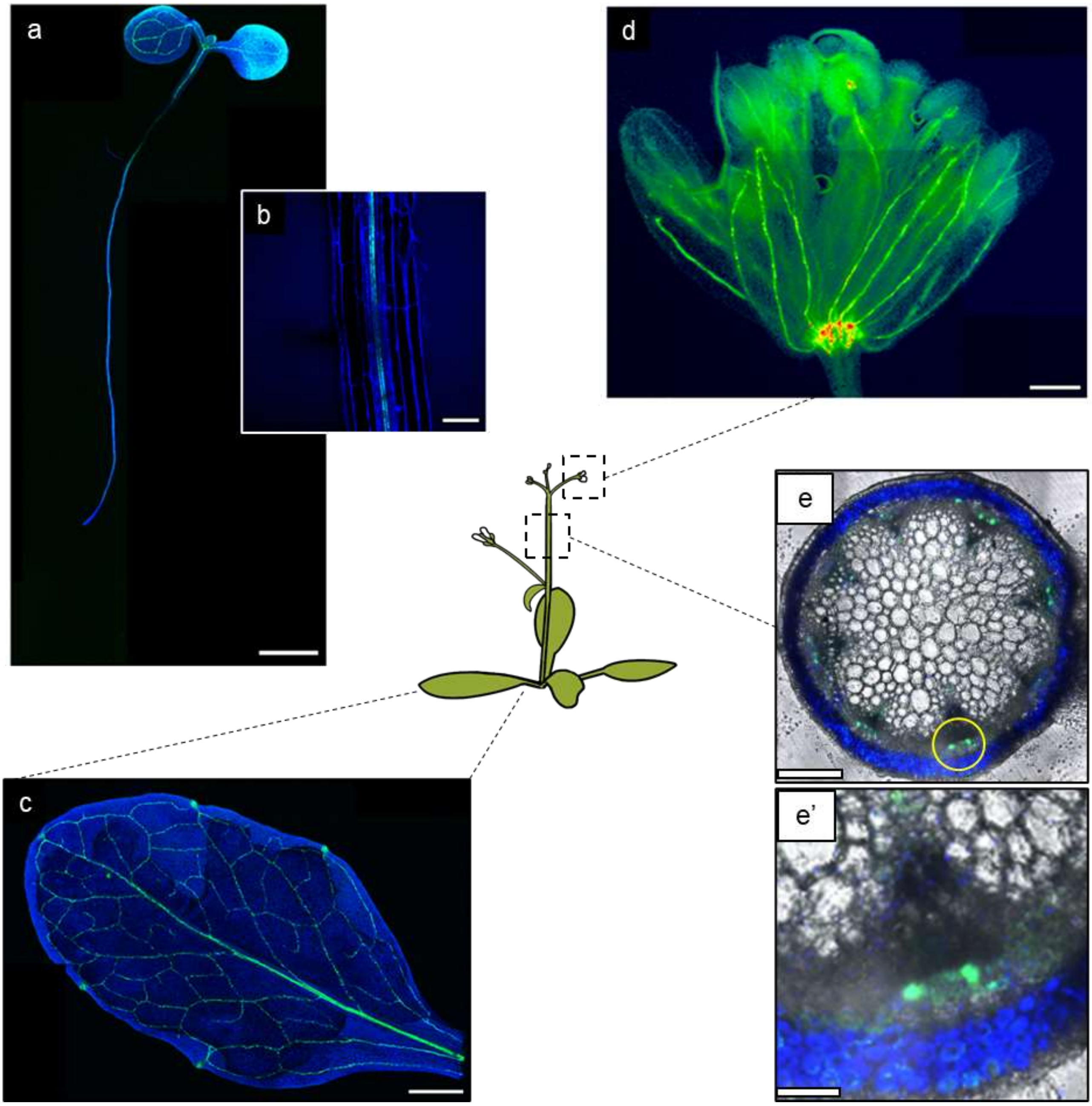

Figure 4. Expression pattern of YC3.6 in the *Arabidopsis thaliana pSUC2::YC3.6* line. (a) Cameleon (green) and chlorophyll (blue) fluorescence of a representative *pSUC2::YC3.6 Arabidopsis* wild type seedling. Scale bar = 2 mm. **(b)** higher magnification of a portion of a root from panel **a**. Scale bar = 50 µm. **(c)** Cameleon and chlorophyll fluorescence of a representative *pSUC2::YC3.6* Arabidopsis wild type mature rosette leaf. Scale bar = 1 mm. **(d)** Cameleon fluorescence of a representative *pSUC::YC3.6* Arabidopsis mature flower. Scale bar = 1 mm. **(e)** Cameleon and chlorophyll fluorescence of a *pSUC2::YC3.6* line in the stem transverse section of the primary inflorescence. Scale bar = 250 µm. **e'**, higher magnification of **e** (yellow circle) showing the confined expression of the YC3.6 to the phloem. YC3.6 (green), chlorophyll (blue), grey (bright field). Scale bar = 100 µm.

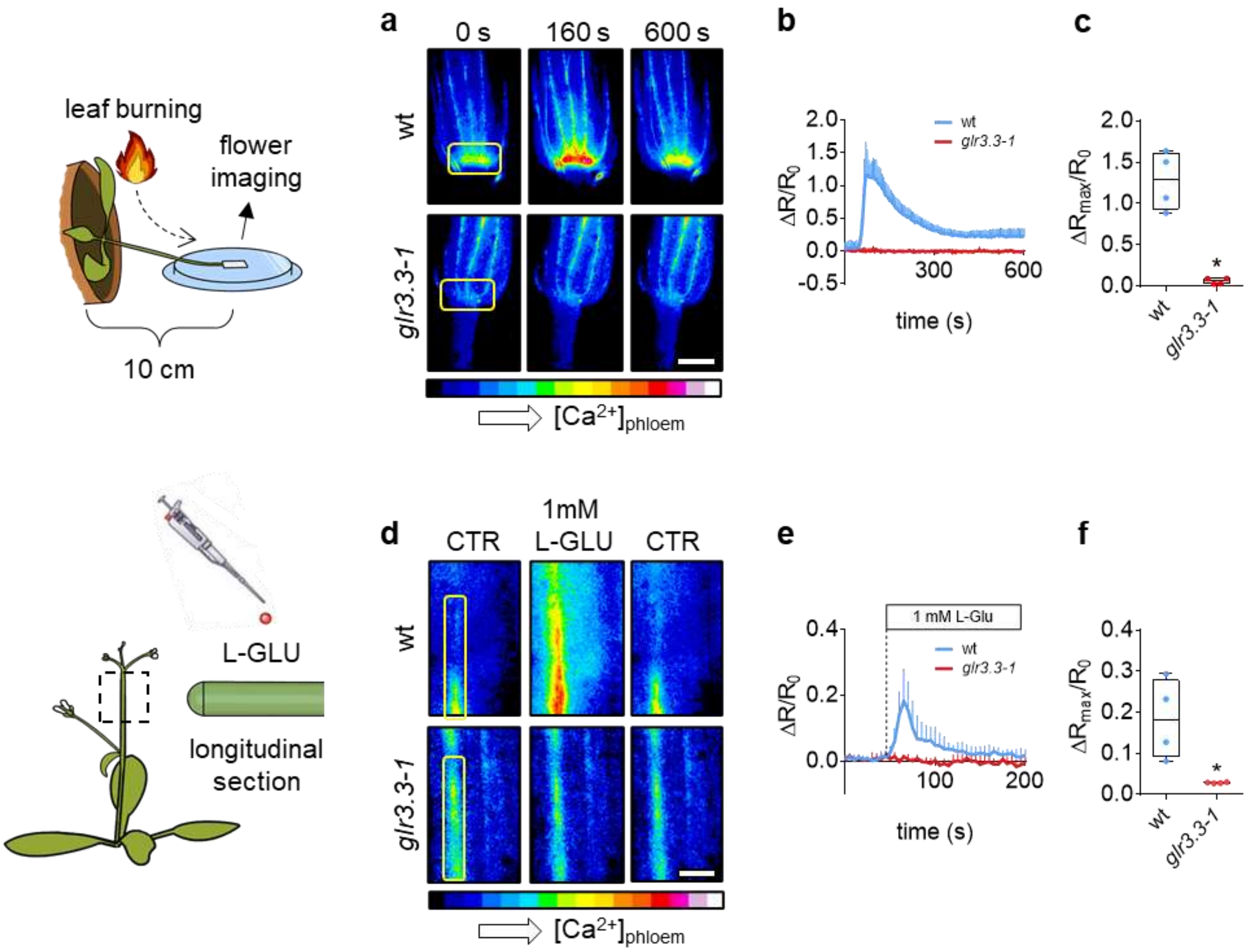

Figure 5. Burn- and L-Glu-induced cytosolic Ca^{2+} concentration increases in phloem cells of the primary inflorescence are dependent on *At*GLR3.3. (a) Schematic drawing of the experimental design and examples of false-colour images (16_colors lookup table) illustrate YC3.6 cpVenus/CFP ratio in flowers in response to the burn of one rosette leaf in the wild type (up) and *glr3.3-1* mutant (bottom) backgrounds. Scale bar = 600 µm. **(b)** YC3.6 normalized fluorescence changes over time in the flower receptacle cells (yellow rectangles) after the burn of one rosette leaf at 60 sec from the beginning of the experiment. **(c)** Maximal peaks of YC3.6 ratio in the flower receptacle cells (yellow rectangle) in the wild type and *glr3.3-1* mutant backgrounds upon burning. **(d)** Schematic drawing of the experimental design and examples of false-colour images illustrate YC3.6 cpVenus/CFP ratio in a longitudinal section of the stem of the primary inflorescence in response to the administration of 1 mM L-Glu in the wild type (up) and *glr3.3-1* mutant (bottom) backgrounds. Scale bar = 140 µm. **(e)** YC3.6 normalized fluorescence changes over time in the phloem of the stem (yellow rectangles) in response to 1 mM L-Glu. **(f)** Maximal peaks of YC3.6 ratio in the phloem of the stem (yellow rectangles) in the wild type and *glr3.3-1* mutant backgrounds upon 1mM treatment. n = 4. Error bars = SD. *$P < 0.05$ (*Student t test*).

II.4 Endoplasmic reticulum does not act as $[Ca^{2+}]_{cyt/nuc}$ sink in AtGLR3.3-dependent responses

Since *At*GLRs are putative ligand-gated ion channels (Price et al., 2012) and being the *At*GLR3.3 able to bind several AAs (Alfieri et al., 2020), the simplest scenario would be that L-Glu released in the apoplast upon leaf-burning induces a $[Ca^{2+}]_{cyt/nuc}$ elevation through the binding to PM-localized *At*GLR3.3 on the apoplastic side. However, despite numerous reports showing data compatible with the presence of *At*GLR3.3 on the plasma membrane of different cell types (Qi et al., 2006, Stephen et al., 2008, Vincill et al., 2013; Wudick et al., 2018; Alfieri et al., 2020; Mou et al., 2020), a recent publication claims that *At*GLR3.3 is localized in the Endoplasmic reticulum (ER) of phloem cells

(Nguyen et al., 2018). The presence of *At*GLR3.3 in the ER may suggest that the observed L-Glu-induced *At*GLR3.3-dependent $[Ca^{2+}]_{cyt}$ increase might be due, at least in part, to the release of Ca^{2+} from the ER lumen (Resentini, Grenzi et al., 2021). In light of this controversial, we decided to explore the role of ER for the genesis of $[Ca^{2+}]_{cyt/nuc}$ increases dependent of *At*GLR3.3 activity. Thus, we employed our recently generated ER-GCaMP6-210 x R-GECO1 *Arabidopsis* sensor line that allows the *in planta* monitoring of Ca^{2+} dynamics within the cytosol ($[Ca^{2+}]_{cyt/nuc}$) and ER lumen ($[Ca^{2+}]_{ER}$) (Resentini, Grenzi et al., 2021). $[Ca^{2+}]_{cyt/nuc}$ rises in systemic leaves and in flower receptacle cells in response to leaf-wounding and leaf-burning, respectively, were shown to be strongly dependent on the activity of *At*GLR3.3 (**Fig.1, Fig.5**). When a rosette leaf of ER-GCaMP6-210 x R-GECO1 plants was wounded, a $[Ca^{2+}]_{cyt/nuc}$ and a sustained $[Ca^{2+}]_{ER}$ increases were detected at the wounding site (**Fig. 6b-d**) and spread to systemic leaves (**Fig. 6f-h**). The $[Ca^{2+}]_{cyt/nuc}$ maxima induced by wounding preceded the $[Ca^{2+}]_{ER}$ maxima in both local and systemic leaves (**Fig. 6e, i**) suggesting that in wounding response the ER likely acts as a Ca^{2+} sink rather than a Ca^{2+} source. We then aimed at performing the leaf burning experiment with the double ER-GCaMP6-210 x R-GECO1 line to analyse in the same flower the Ca^{2+} dynamics in the two compartments. Unfortunately, in the selected line no fluorescence was detectable in flowers, an issue probably due to silencing occurring in adult plants. Nonetheless, we performed the experiment with the single ER-GCaMP6-210 and in response to leaf-burning, only a sustained rise of $[Ca^{2+}]_{ER}$ was observed both in the stem and flower receptacle (**Fig. 6l-n**). The fact that we were not able to measure in the same cells the ER-GCaMP6-210 and R-GECO1 fluoresce emissions in flower tissues, makes impossible any speculation about temporal causality between $[Ca^{2+}]_{ER}$ and $[Ca^{2+}]_{cyt/nuc}$ responses. Nevertheless, the lack of a $[Ca^{2+}]_{ER}$ decrease excludes the idea that the ER can be a Ca^{2+} source in response to burning.

To further support the hypothesis the ER is not involved in the generation of $[Ca^{2+}]_{cyt/nuc}$ transients dependent on the *At*GLR3.3 activity we performed experiments in the root tip cells of the double ER-GCaMP6-210 x R-GECO1 line. It is well known that *At*GLR3.3 plays a major role in the generation of $[Ca^{2+}]_{cyt}$ increases induced by L-Glu and other AAs in root tip cells (Qi et al., 2006, Alfieri et al., 2020), in which our previous localization data revealed the presence of *At*GLR3.3 also in endomembranes (Alfieri et al., 2020). Thereby, to further inspect the ER role in *At*GLR3.3-dependent responses, we assayed the effect of L-Glu administration on $[Ca^{2+}]_{cyt/nuc}$ and $[Ca^{2+}]_{ER}$ of *Arabidopsis* root tip cells (**Fig. 6o**). ER-GCaMP6-210 x R-GECO1 seedlings were placed in an imaging chamber and both fluorescence emissions were register at single cell resolution. Samples were continuously perfused with an imaging control solution and L-Glu treatment was pulsed for 3 min at the indicated time. 1mM L-Glu triggered a rapid $[Ca^{2+}]_{cyt/nuc}$ transient and a sustained $[Ca^{2+}]_{ER}$ increase (**Fig 6 o-q**). Moreover, the high spatial and temporal resolution revealed that the $[Ca^{2+}]_{ER}$ elevation temporally follows the $[Ca^{2+}]_{cyt/nuc}$ transient with an average delay of 4 ± 1.6 sec (**Fig 6.r, s**).

Altogether, data collected with three different experimental setups (leaf-wounding, leaf-burning, L-Glu treatment in root) suggest that *At*GLR3.3 is unlikely to be active in the ER. This is not necessarily

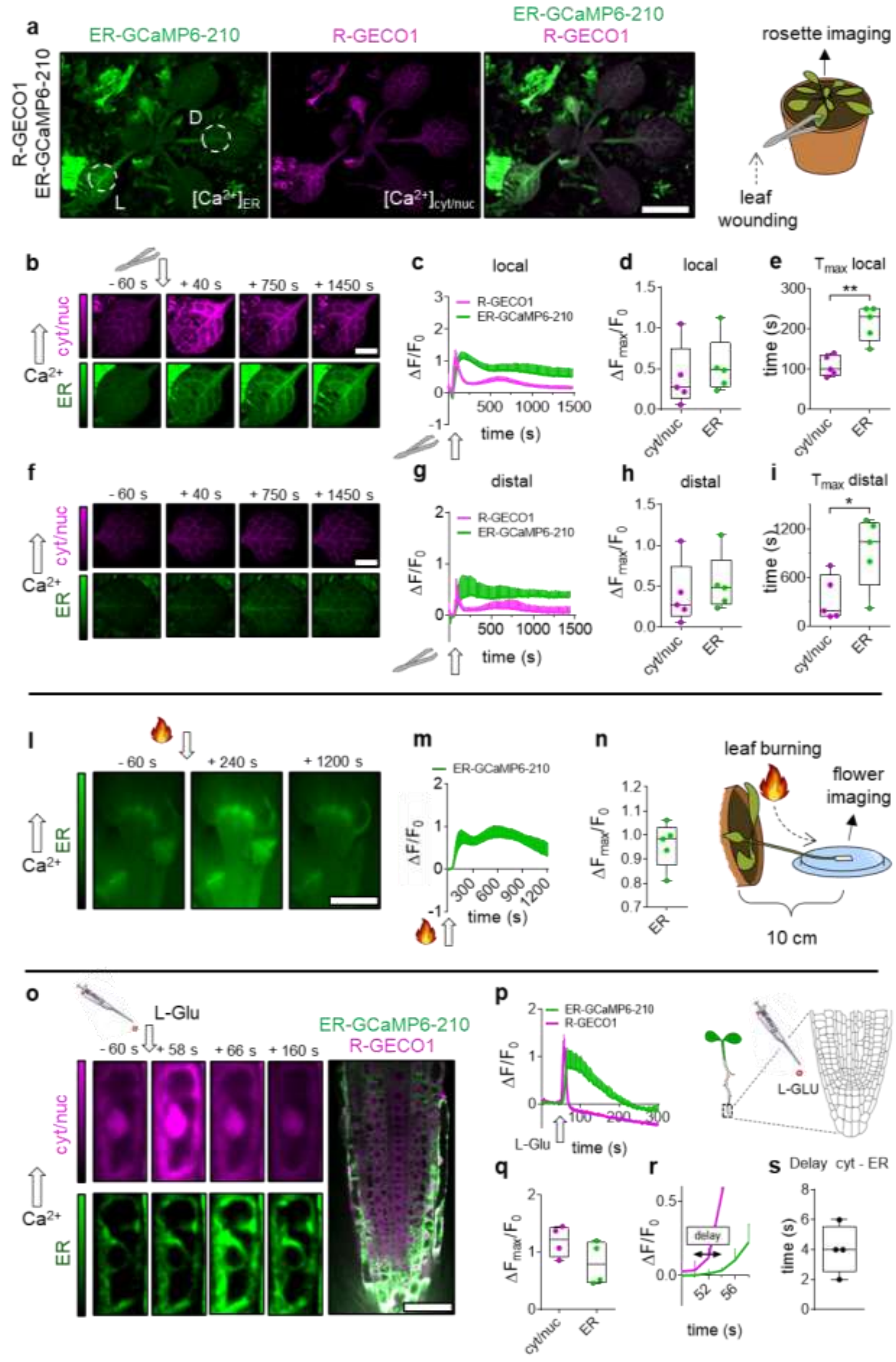
a
ER-GCaMP6-210
R-GECO1
ER-GCaMP6-210
R-GECO1
R-GECO1
ER-GCaMP6-210
D
L
$[Ca^{2+}]_{ER}$
$[Ca^{2+}]_{cyt/nuc}$
rosette imaging
leaf wounding
b
- 60 s
+ 40 s
+ 750 s
+ 1450 s
cyt/nuc
Ca^{2+}
ER
c
local
R-GECO1
ER-GCaMP6-210
$\Delta F/F_0$
time (s)
d
local
$\Delta F_{max}/F_0$
cyt/nuc
ER
e
T_{max} local
**
time (s)
f
g
distal
h
distal
i
T_{max} distal
*
l
- 60 s
+ 240 s
+ 1200 s
m
ER-GCaMP6-210
n
leaf burning
flower imaging
10 cm
o
L-Glu
- 60 s
+ 58 s
+ 66 s
+ 160 s
ER-GCaMP6-210
R-GECO1
p
L-Glu
L-GLU
q
r
delay
s
Delay cyt - ER

Figure 6. Analyses of endoplasmic reticulum (ER) and cytosolic Ca^{2+} dynamics in response to leaf wound, leaf burn, and L-Glu administration. (a) False-colour fluorescence images of a representative pUBQ10-ER-GCaMP6-210 x pUBQ10-R-GECO1 mature plant and schematic drawing of the experimental design (ER-GCaMP6-210 green, R-GECO1 magenta). Scale bar 1 cm. **(b)** Examples of false-colour images illustrate ER-GCaMP6-210 (green) and R-GECO1 (magenta) in a local wounded leaf (L). Scale bar = 7 mm. **(c)** ER-GCaMP6-210 and R-GECO1 normalized fluorescence changes of the local leaf (L) over the time after its wound (white arrow). **(d)** Maximal peaks of ER-GCaMP6-210 and R-GECO1 fluorescence signals in the local leaf (L) after wound. **(e)** Time required to reach maximal peaks of ER-GCaMP6-210 and R-GECO1 fluorescence signals in the local leaf (L) after wound. **(f)** Examples of false-colour images illustrate ER-GCaMP6-210 (green) and R-GECO1 (magenta) in a distal leaf (D). Scale bar = 7 mm. **(g)** ER-GCaMP6-210 and R-GECO1 normalized fluorescence changes of the distal leaf (D) over the time after wound (white arrow). **(h)** Maximal peaks of ER-GCaMP6-210 and R-GECO1 fluorescence signals in the distal leaf (D) after wound. **(i)** Time required to reach maximal peaks of ER-GCaMP6-210 and R-GECO1 fluorescence signals in the distal leaf (D) after wound. **(l)** exemplary false-colour images of ER-GCaMP6-210 fluorescence (green) of a representative primary inflorescence in response to the burn of one rosette leaf and schematic drawing of the experimental design. Scale bar = 300 µm **(m).** ER-GCaMP6-210 normalized fluorescence changes over the time of the selected cells (ROI, Region Of Interest) in panel **i** after the burn of one rosette leaf (white arrow). **(n)** Maximal peak of the ER-GCaMP6-210 fluorescence signal in the selected cells (ROI) after burn. **(o)** Examples of false-color images illustrate R-GECO1 (magenta) and ER-GCaMP6-210 (green) of a single cell of an *Arabidopsis* root treated with 1 mM L-Glu for 3 min, and schematic drawing of the experimental design. Scale bar = 50 µm**. (p)** ER-GCaMP6-210 and R-GECO1 normalized fluorescence changes of root tip single cells over the time after L-Glu treatment (white arrow). **(q)** Maximal peaks of ER-GCaMP6-210 and R-GECO1 fluorescence signals in the root tip cells after L-Glu treatment. **(r)** Same as panel **p** but x-axis, y-axis scales, and ranges adjusted. **(s)** Mean delay of the fluorescence increase of the ER-GCaMP6-210 compared to the fluorescence change of the R-GECO1 following 1 mM L-Glu administration. n ≥ 4. Error bars = SD. **P < 0.05, **P < 0.005 (Student t test).*

in contradiction with *At*GLR3.3 published localization data. In fact, they come from localization studies on *At*GLR3.3-VENUS (Nguyen et al., 2018, Toyota et al., 2018) and *At*GLR3.3-GFP (Vincill et al., 2013, Alfieri et al., 2020) chimeric proteins which can be affected by several issues. The principal disadvantage is that the tag may alter location and function of the native protein (Moore et al., 2009). As an example, in our hands the *At*GLR3.3-GFP chimeric protein failed to restore the AA-induced *At*GLR3.3-dependent $[Ca^{2+}]_{cyt/nuc}$ response when expressed in the *glr3.3-1* mutant background. *De facto*, one could predict that if *At*GLR3.3 was only localised in the ER it would participate in the genesis of a $[Ca^{2+}]_{cyt/nuc}$ rise by mediating the release of Ca^{2+} from the ER. On the contrary, in all the experiments performed we never detected an ER-GCaMP6-210 fluorescence decrease but only a signal increase that in root tip cells clearly followed the one of R-GECO1. We concluded that in *At*GLR3.3-dependent cytosolic Ca^{2+} increases the ER acts as Ca^{2+} sink. Therefore, we suggest that at least in part also in the phloem cells *At*GLR3.3 must be localized on the plasma membrane but this needs to be demonstrated.

II.5. The amino acid-binding by AtGLR3.3 is required for its function

To functionally characterize *in vivo* the physiological role of the L-Glu binding of *At*GLR3.3, we took advantage of the recently released 3D structure of its Ligand Binding Domain (LBD) bound to L-Glu (Alfieri et al., 2020). Exploiting the structural data, we identified the evolutionarily invariant arginine Arg550 (**Fig. 7a**) and aspartic acid Asp543 (**Fig. 7b**) as two of the key residues required for the binding of the ligand. The Arg550 chelates the α-carboxyl group of the ligand by a bidentate ionic interaction and the Asp543 side chain lies at the centre of a hydrogen-bond network that helps the

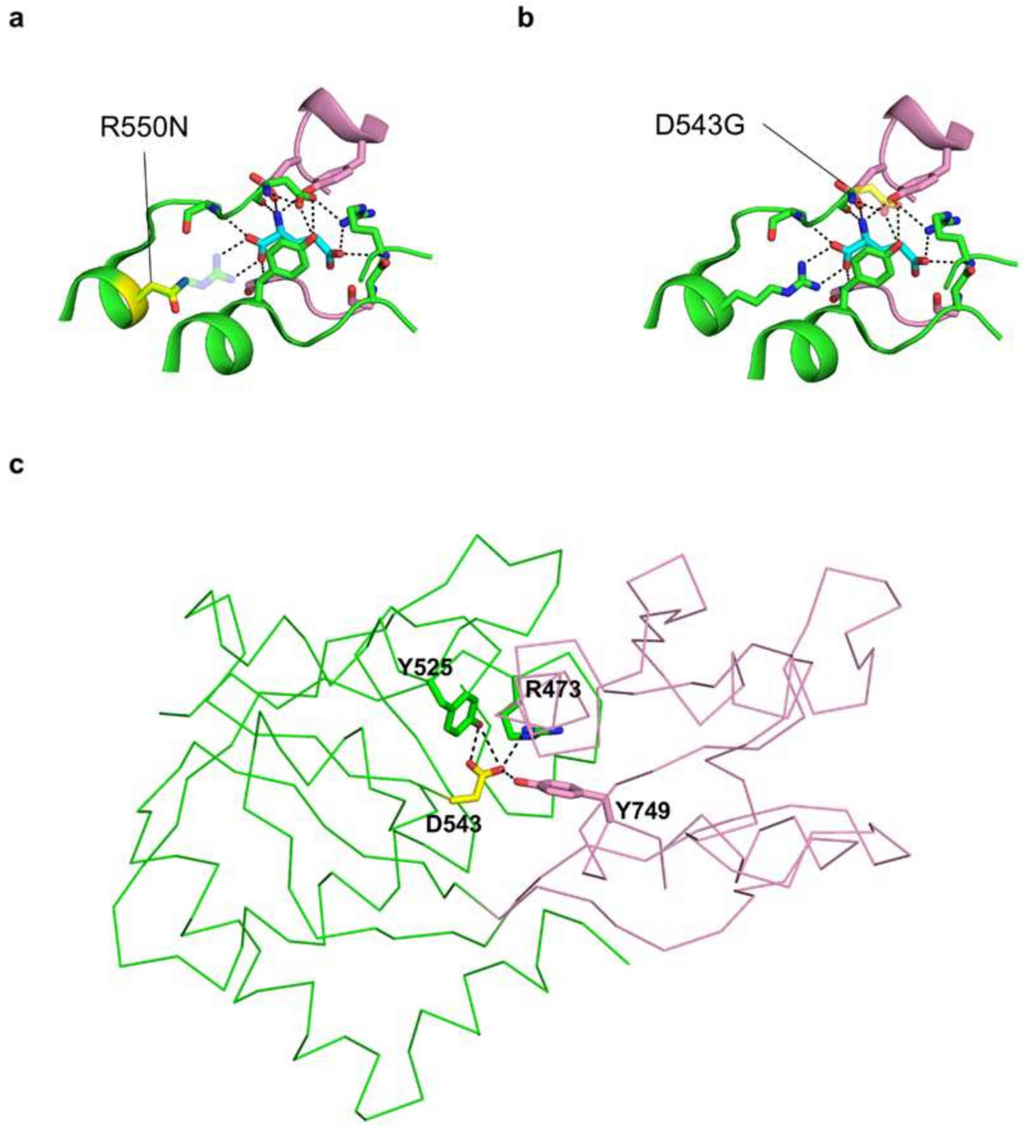

Figure 7. 3D structural representations of *At*GLR3.3 LBD mutants. a-b, close-up views of the predicted binding sites of *At*GLR3.3 LBD R550N (**a**) and D543G (**b**), where the visible portion of protein main chain is in ribbon representation and the L-Glu ligand (light blue) and relevant surrounding side chains are shown as sticks. The green and pink colours identify the portions of the protein belonging to subdomains 1 and 2 of the LBD, respectively. The Arg550 and the Asp543 side chains deleted by the R550N and D543G mutations are denoted in yellow. **c,** overall view of the *At*GLR3.3 LBD in wire representation, with a few side chains in stick representation. The figure highlights the importance of the Asp543 side chain (yellow) in engaging hydrogen-bond interactions with both subdomain 1 (S1, green) and subdomain 2 (S2, pink); therefore, Asp543 side chain is presumably important in stabilizing the locked position of the two subdomains of LBD around the ligand.

two LBD subdomains to trap the ligand (**Fig. 7c**). These pieces of evidence allowed us to reason that mutation of either of these two residues should abolish, or at least strongly reduce, the L-Glu binding capacity of *At*GLR3.3. A similar prediction has been also made for the *At*GLR3.2, where the mutation of the Arg551 residue (homologous to Arg550 in the *At*GLR3.3) prevents, in COS-7 cells, the modulation of the channel activity by Gly and L-Met keeping the channel constitutively open

(Gangwar et al., 2021). In our previous work, we attempted to independently introduce the Arg550Asp (R550N) and Asp543Gly (D543G) mutations in the isolated recombinant *At*GLR3.3 LBD (Alfieri et al., 2020). Unfortunately, the recombinant mutant LBDs did not retain sufficient solubility to be scaled up for larger production, *de facto* preventing us to experimentally test their ability to bind or not the ligands (Alfieri et al., 2020). Nevertheless, we reasoned that the same mutations could be tolerated by the entire *At*GLR3.3 protein as demonstrated by published works where single point mutations were introduced into the LBDs of different GLR isoforms (e.g. *At*GLR1.4; *At*GLR3.2) and the variants were successfully expressed in animal cells (Tapken et al., 2013, Gangwar et al., 2021). Therefore, we adopted an *in planta* functional complementation approach by introducing mutated variants of the *At*GLR3.3 LBD into two independent *glr3.3* T-DNA lines (*glr3.3-1* and *glr3.3-2*) (Qi et al., 2006) expressing the Nuclear Export Signal (NES)-YC3.6 Ca^{2+} indicator (Krebs et al., 2012; Alfieri et al., 2020). Also in this case, the choice of using the FRET-based indicator Cameleon YC3.6 was due to its superior properties for the comparison of Ca^{2+} at resting and in response to different stimuli of different genetic backgrounds. First, we fused the full-length *At*GLR3.3 coding sequence to the eGFP and introduced independently the two selected point mutations to generate the $GLR3.3_{R550N}$-eGFP and $GLR3.3_{D543G}$-eGFP variants. The expression of the different eGFP fusion proteins in *Nicotiana benthamiana* leaf epidermal cells revealed that both *At*GLR3.3 variants were efficiently expressed, showing a subcellular localization pattern similar to the one observed with the $GLR3.3_{wt}$ (**Fig. 8**). Having demonstrated that the *At*GLR3.3 full-length protein well tolerate single point mutations within its LBD, we independently made the same amino acid substitutions in the full-length genomic sequence of the *AtGLR3.3* gene to generate *pGLR3.3::gGLR3.3*$_{R550N}$ and *pGLR3.3::gGLR3.3*$_{D543G}$ constructs. The two *AtGLR3.3* genomic variants, and the wild type *pGLR3.3::gGLR3.3*$_{wt}$ as a control, were then introduced in *glr3.3-1* and *glr3.3-2* (Qi et al., 2006, Alfieri et al., 2020) (**Fig. 9a, b**). By performing qRT-PCR analysis we confirmed that the wild type and mutated *AtGLR3.3* variants were expressed in seedlings and flowers of the different generated lines (**Fig. 9b, c**). Moreover, the sequencing of RT-PCR amplicons confirmed the presence of the mutations (**Fig. 9d**). In order to see if any *At*GLR3.3 activity is present in the *glr3.3 x GLR3.3*$_{R550N}$ and *glr3.3 x GLR3.3*$_{D543G}$ lines, we made use of the well-established root tip Ca^{2+} imaging assay where L-Glu can be applied at desired concentrations and in a reliable and precise way (Alfieri et al., 2020). All the experiments were performed on two independent alleles for each genotype. Firstly, it was checked if the expression of *AtGLR3.3* variants carrying LBD mutations could affect the $[Ca^{2+}]_{cyt}$ at rest. No statistically differences of the resting cpVenus/CFP ratio (R) were observed among the different genetic backgrounds (**Fig. 10a**). We next assessed the LBD mutations effect on the ability of *At*GLR3.3 to mediate the Ca^{2+} response induced by L-Glu administration in root tip cells. When the root of a wt plant was treated with 1 mM L-Glu (pulse of 3 min in continuous perfusion) a rapid and transient $[Ca^{2+}]_{cyt}$ increase was observed, quantified in 0.52 ± 0.13 as the maximal increase in the normalized ΔR ($\Delta R_{max}/R_0$) (**Fig. 10b, c**). In *glr3.3* plants the $[Ca^{2+}]_{cyt}$ response induced by 1mM

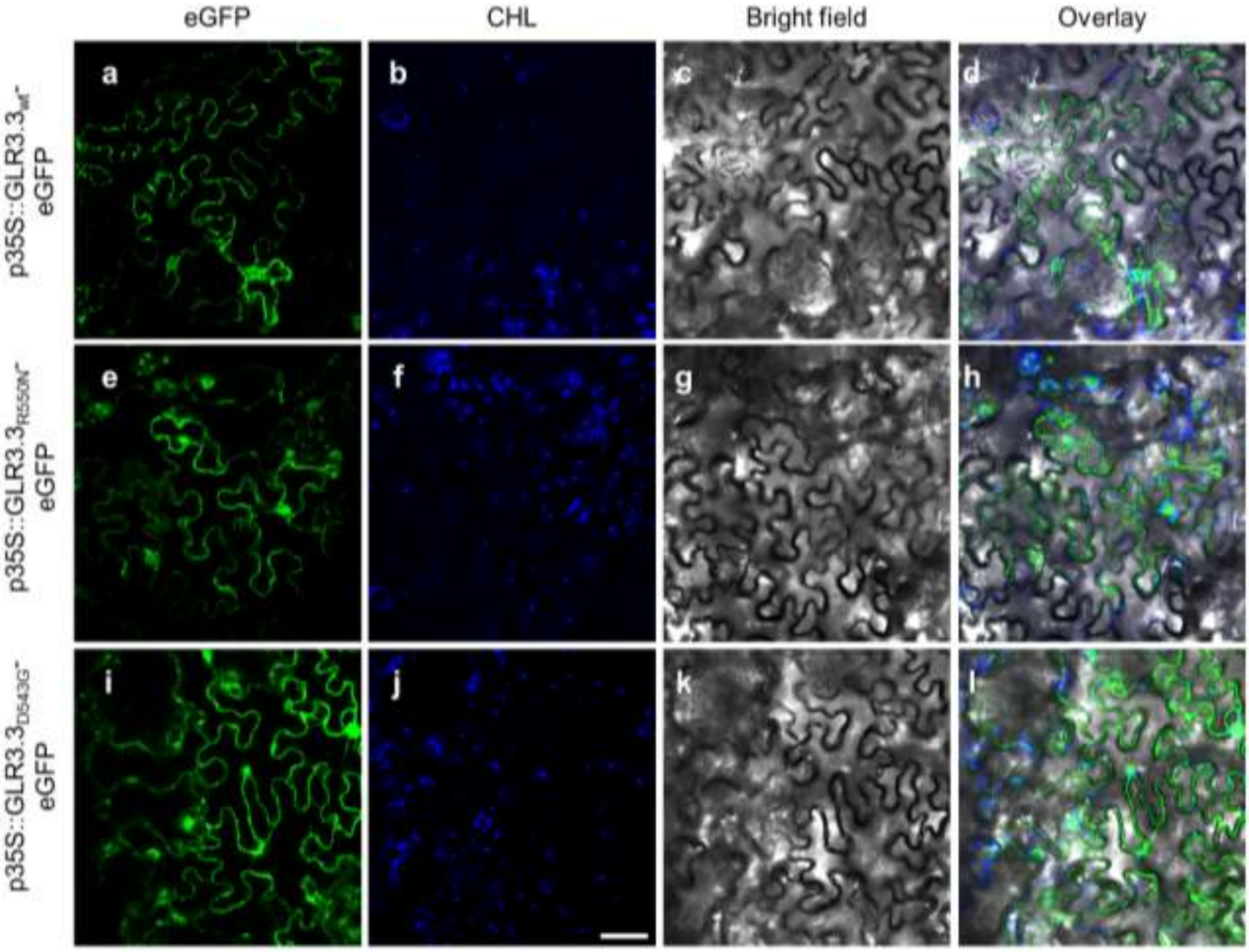

Figure 8. Subcellular distribution of wild type and mutated GLR3.3-eGFP in *Nicotiana benthamiana* leaf epidermal cells. a-d, confocal images of *N. benthamiana* agroinfiltrated epidermal cells transformed with GLR3.3$_{wt}$–eGFP under the control of the CaMV35S promoter. **a**, green: eGFP fluorescence. **b,** blue: chlorophyll autofluorescence. **c,** bright field. **d,** overlay of panels **a-c**. **e-h**, confocal images of *N. benthamiana* agroinfiltrated epidermal cells transformed with GLR3.3$_{R550N}$–eGFP under the control of the CaMV35S promoter. **e,** green: eGFP fluorescence. **f,** blue: chlorophyll autofluorescence. **g**, bright field. **h,** overlay of panels **e-g**. **i-l**, **c**onfocal images of *N. benthamiana* agroinfiltrated epidermal cells transformed with GLR3.3$_{D543G}$–eGFP under the control of the CaMV35S promoter. **i**, green: eGFP fluorescence. **j,** blue: chlorophyll autofluorescence. **k**, bright field. **l,** overlay of panels **i-k**. Scale bar = 50 µm.

L-Glu was completely abolished ($\Delta R_{max}/R_0 = 0.005 \pm 0.004$ for *glr3.3-1* and $\Delta R_{max}/R_0 = 0.016 \pm 0.002$ for *glr3.3-2*) (**Fig. 10e-f'**), whereas the phenotype was fully rescued in plants expressing the wt *At*GLR3.3 variant ($\Delta R_{max}/R_0 = 0.7 \pm 0.18$ for GLR3.3-1 and $\Delta R_{max}/R_0 = 0.34 \pm 0.08$ for GLR3.3-2) (**Fig. 10h-i'**). Plants expressing the R550N and D543G mutated variants of *At*GLR3.3 did not show clear 1mM L-Glu-induced $[Ca^{2+}]_{cyt}$ increase ($\Delta R_{max}/R_0 = 0.009 \pm 0.007$ for R550N-1 and $\Delta R_{max}/R_0 = 0.024 \pm 0.009$ for R550N-2, $\Delta R_{max}/R_0 = 0.012 \pm 0.004$ for D543G-1 and $\Delta R_{max}/R_0 = 0.038 \pm 0.011$ for D543G-2) (**Fig. 10k-l', n-o'**). This latter result allowed us to suggest that the lack of a response observed with R550N and D543G variants do not bind or have a reduction of the binding affinity for L-Glu. To test this hypothesis we performed a series of experiment were the root tip cells of the different genetic backgrounds were treated with a higher concentration of L-Glu (2.5 mM).

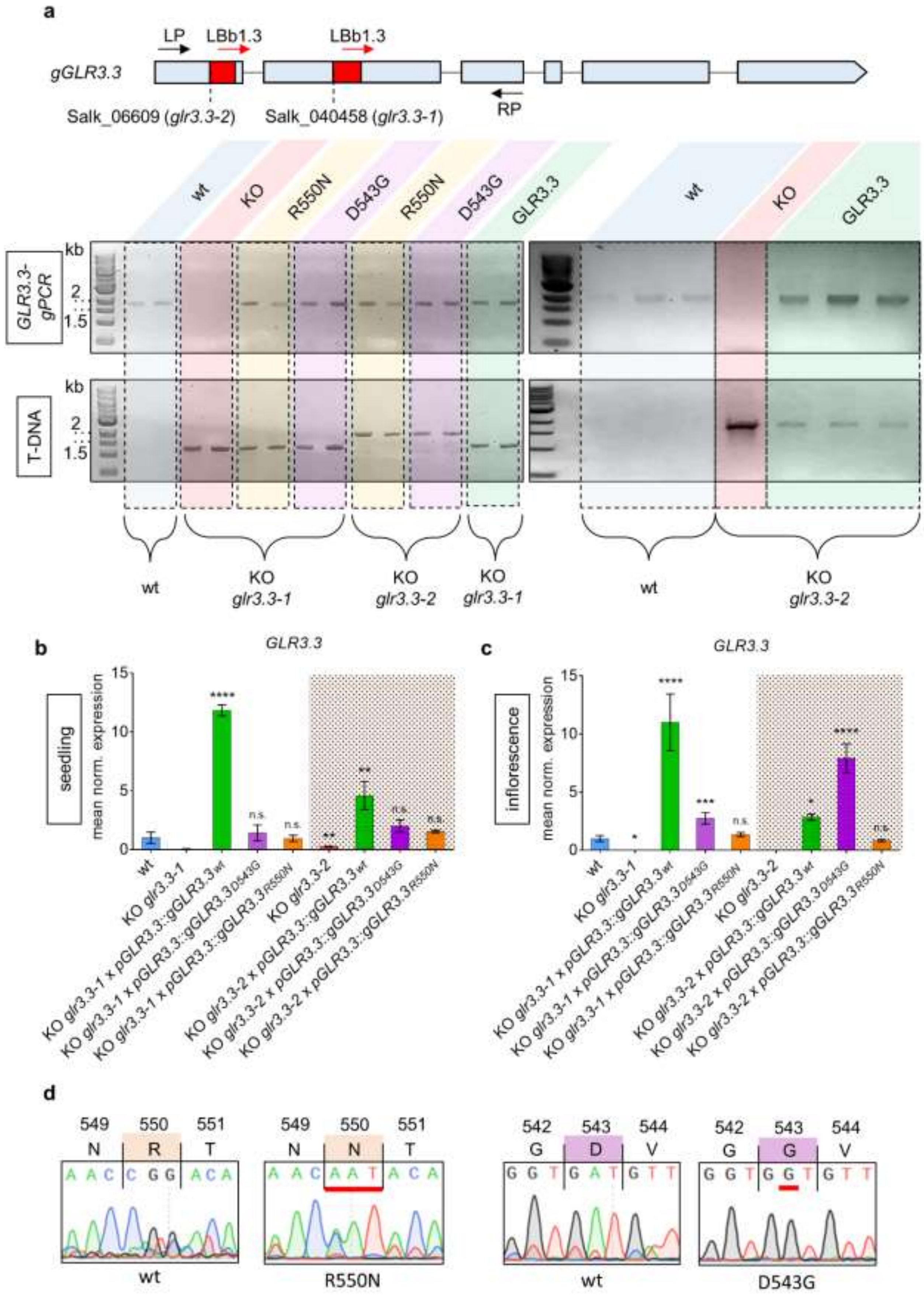
a
LP
LBb1.3
LBb1.3
gGLR3.3
RP
Salk_06609 (glr3.3-2)
Salk_040458 (glr3.3-1)
wt
KO
R550N
D543G
R550N
D543G
GLR3.3
wt
KO
GLR3.3
kb
2
1.5
GLR3.3-gPCR
T-DNA
kb
2
1.5
wt
KO glr3.3-1
KO glr3.3-2
KO glr3.3-1
wt
KO glr3.3-2
b
GLR3.3
seedling
mean norm. expression
15
10
5
0
****
n.s.
n.s.
**
**
n.s.
n.s.
wt
KO glr3.3-1
KO glr3.3-1 x pGLR3.3::gGLR3.3wt
KO glr3.3-1 x pGLR3.3::gGLR3.3D543G
KO glr3.3-1 x pGLR3.3::gGLR3.3R550N
KO glr3.3-2
KO glr3.3-2 x pGLR3.3::gGLR3.3wt
KO glr3.3-2 x pGLR3.3::gGLR3.3D543G
KO glr3.3-2 x pGLR3.3::gGLR3.3R550N
c
GLR3.3
inflorescence
mean norm. expression
15
10
5
0
*
****
***
n.s.
*
****
n.s.
wt
KO glr3.3-1
KO glr3.3-1 x pGLR3.3::gGLR3.3wt
KO glr3.3-1 x pGLR3.3::gGLR3.3D543G
KO glr3.3-1 x pGLR3.3::gGLR3.3R550N
KO glr3.3-2
KO glr3.3-2 x pGLR3.3::gGLR3.3wt
KO glr3.3-2 x pGLR3.3::gGLR3.3D543G
KO glr3.3-2 x pGLR3.3::gGLR3.3R550N
d
549 550 551
N R T
A A C C G G A C A
wt
549 550 551
N N T
A A C A A T A C A
R550N
542 543 544
G D V
G G T G A T G T T
wt
542 543 544
G G V
G G T G G T G T T
D543G

Figure 9. Generation and validation of the *glr3.3-1* and *glr3.3-2* complemented lines and expression analysis of *AtGLR3.3* in the different genetic backgrounds. a, genotyping of *glr3.3-1* and *glr3.3-2* knock out (KO) mutants and mutants complemented with the wild type *pGLR3.3::gGLR3.3*$_{wt}$, *pGLR3.3::gGLR3.3*$_{R550N}$, and *pGLR3.3::gGLR3.3*$_{D543G}$ genomic sequences. PCRs were performed with specific primers (listed in Supplementary Table 2) using genomic DNA for *GLR3.3* (upper panels), and T-DNA (bottom panels) as a template. Two independent plants for the same selected genotype were tested. **b**, *GLR3.3* expression by qRT-PCR in 6-day-old Arabidopsis seedlings for Col-0 wild type, *glr3.3-1*, *glr3.3-1* x *pGLR3.3::gGLR3.3*$_{wt}$, *glr3.3-1 x pGLR3.3::gGLR3.3*$_{R550N}$, *glr3.3-1 x pGLR3-3::gGLR3.3*$_{D543G}$, *glr3.3-2*, *glr3.3-2* x *pGLR3.3::gGLR3.3*$_{wt}$, *glr3.3-2 x pGLR3.3::gGLR3.3*$_{R550N}$, *glr3.3-2 x pGLR3-3::gGLR3.3*$_{D543G}$ genetic backgrounds. The transcript abundances were quantified by qRT-PCR relative to that of TUBULIN (At5g44340, TUB). n = 3. Primers are listed in Supplementary Table 2. **c**, *GLR3.3* expression by qRT-PCR in 5-week-old Arabidopsis primary inflorescence for Col-0 wild type, *glr3.3-1*, *glr3.3-1* x *pGLR3.3::gGLR3.3*$_{wt}$, *glr3.3-1 x pGLR3.3::gGLR3.3*$_{R550N}$, *glr3.3-1 x pGLR3-3::gGLR3.3*$_{D543G}$, *glr3.3-2*, *glr3.3-2 x pGLR3.3::gGLR3.3*$_{R550N}$, *glr3.3-2 x pGLR3-3::gGLR3.3*$_{D543G}$ genetic backgrounds. The transcript abundances were quantified by qRT-PCR relative to that of TUBULIN (At5g44340, TUB). n = 3. Primers are listed in Supplementary Table 2. **d**, chromatograms of the RT-PCR *GLR3.3* sequenced amplicons obtained from the different lines in the *glr3.3-1* genetic background. Primers are listed in Supplementary Table 2. Error bars ± SD. ns = not significant, *$P < 0.05$, **$P < 0.01$, ***$P < 0.001$,

2.5 mM Glu triggered in wt plants a $[Ca^{2+}]_{cyt}$ increase ($\Delta R_{max}/R_0 = 0.56 \pm 0.18$) (**Fig. 10d, q**) not dissimilar from what reported with 1 mM L-Glu. Plants expressing the wt variant of *At*GLR3.3 showed the same response to the wt ($\Delta R_{max}/R_0 = 0.57 \pm 0.18$ for GLR3.3-1 and $\Delta R_{max}/R_0 = 0.56 \pm 0.22$ for GLR3.3-2) (**Fig. 10j, j', q**). Surprisingly, plants expressing the *At*GLR3.3 D543G showed a clear $[Ca^{2+}]_{cyt}$ increase in response to 2.5 mM L-Glu ($\Delta R_{max}/R_0 = 0.037 \pm 0.017$ for D543G-1 and $\Delta R_{max}/R_0 = 0.056 \pm 0.22$ for D543G-2) (**Fig. 10p-u**) which was, however, still absent in both *glr3.3* and R550N plants (**Fig. 10g, g', m, m', k-u**). Overall, these experiments highlighted that the mutation of key residues for the AA binding in the LBD of *At*GLR3.3 strongly affected the L-Glu response. In particular, we can predict that the R550N mutation strongly impairs the L-Glu binding whereas the D543G still retains a residual binding. Specifically, the replacement of the Arg550 with the Asn should cause the loss of two hydrogen bonds directly involved in the binding with the ligand (**Fig. 7a**). Asp543 instead coordinates the hydrogen bonds with other LBD residues, and these hydrogen bonds are not directly involved in the amino acid-binding (**Fig. 7b, c**). Hence, it can be inferred that the D543G reduction of binding affinity is plausibly due to a general disruption of the binding pocket architecture that affect the accommodation of the ligand even though the residues directly involved in the binding remain unaltered. These data are compatible with a model according to which the direct sensing of L-Glu by the *At*GLR3.3 LBD is necessary for the L-Glu-induced $[Ca^{2+}]_{cyt}$ influx mediated by *At*GLR3.3 in root tip cells.

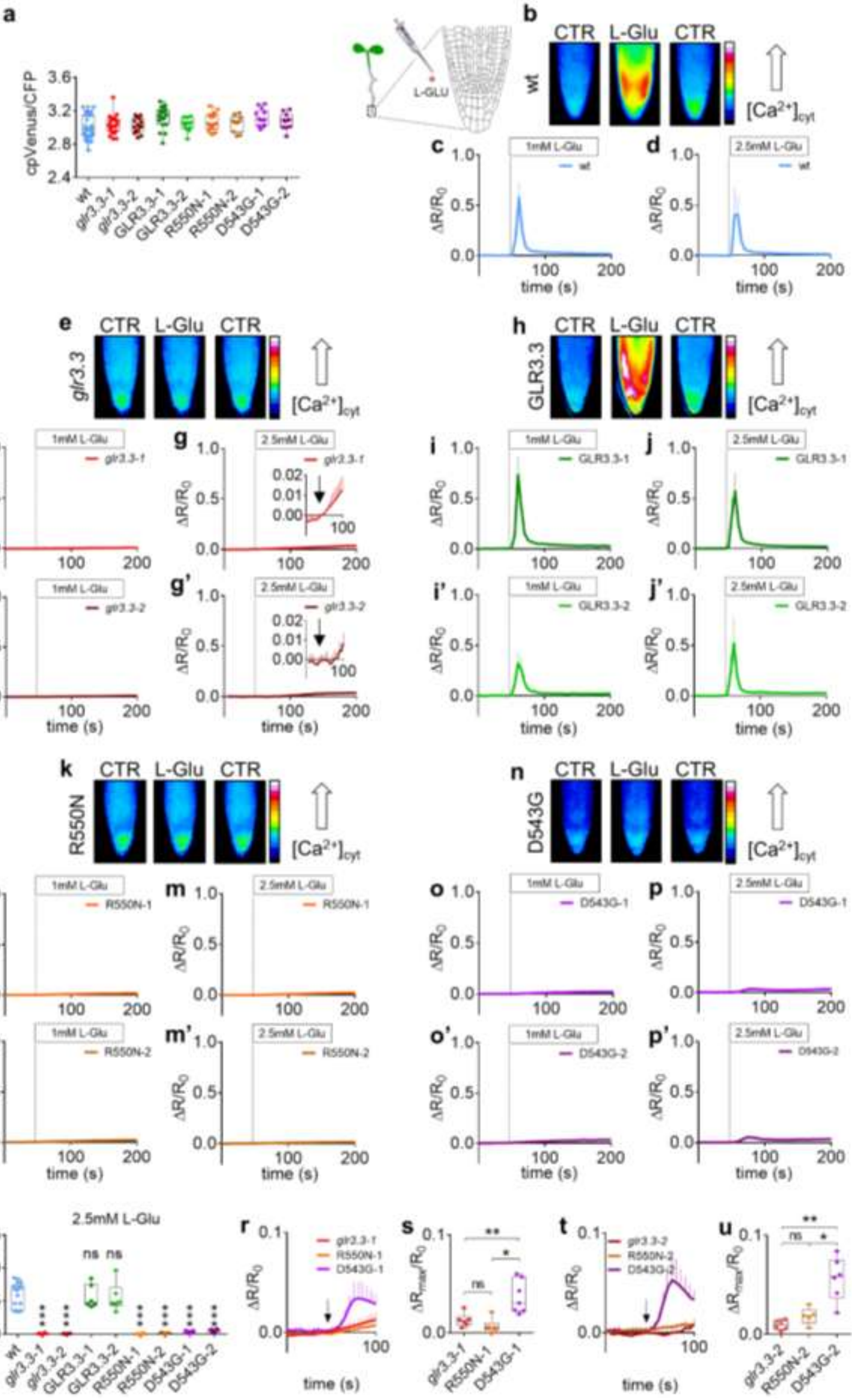
a
cpVenus/CFP
3.6
3.2
2.8
2.4
wt
glr3.3-1
glr3.3-2
GLR3.3-1
GLR3.3-2
R550N-1
R550N-2
D543G-1
D543G-2
L-GLU
b
CTR
L-Glu
CTR
wt
[Ca2+]cyt
c
1mM L-Glu
wt
ΔR/R0
time (s)
d
2.5mM L-Glu
wt
e
glr3.3
f
glr3.3-1
g
f'
glr3.3-2
g'
0.02
0.01
0.00
h
GLR3.3
i
GLR3.3-1
j
i'
GLR3.3-2
j'
k
R550N
l
R550N-1
m
l'
R550N-2
m'
n
D543G
o
D543G-1
p
o'
D543G-2
p'
q
2.5mM L-Glu
ΔRmax/R0
ns
***
r
s
**
*
t
u

Figure 10. *In planta* functional analysis of the role of *At*GLR3.3 LBD in the root local response to L-Glu. (a) Schematic drawing of the experimental design and NES-YC3.6 cpVenus/CFP steady-state ratios in root tip cells for Col-0 (wt, light blue), *glr3.3-1* (red), *glr3.3-2* (dark red), *glr3.3-1* x *pGLR3.3::gGLR3.3*$_{wt}$ (GLR3.3-1, dark green), *glr3.3-2* x *pGLR3.3::gGLR3.3*$_{wt}$ (GLR3.3-2, light green), *glr3.3-1 x pGLR3.3::gGLR3.3*$_{R550N}$ (R550N-1, orange), *glr3.3-2 x pGLR3.3::gGLR3.3*$_{R550N}$ (R550N-2, dark orange), *glr3.3-1 x pGLR3-3::gGLR3.3*$_{D543G}$ (D543G-1, purple) and *glr3.3-1 x pGLR3-3::gGLR3.3*$_{D543G}$ (D543G-2, dark purple) genetic backgrounds. **(b)** Representative ratiometric images of wt seedling root tips for three selected time points in response to 2.5 mM L-Glu. **(c)** NES-YC3.6 normalized ratio changes of wt root tip cells over the time acquired under continuous perfusion and after treatment with 1 mM L-Glu for 3 min, as indicated by the white empty box on the x-axis. **(d)** NES-YC3.6 normalized ratio changes of wt root tip cells over the time acquired under continuous perfusion and after treatment with 2.5 mM L-Glu for 3 min, as indicated by the white empty box on the x-axis. **(e)** Representative ratiometric images of *glr3-3-1* seedling root tips for three selected time points in response to 2.5 mM L-Glu. **(f)** NES-YC3.6 normalized ratio changes of *glr3.3-1* and **(f')** *glr3.3-2* root tip cells over the time acquired under continuous perfusion and after treatment with 1 mM L-Glu for 3 min, as indicated by the white empty box on the x-axis. **(g)** NES-YC3.6 normalized ratio changes of *glr3.3-1* and **(g')** *glr3.3-2* root tip cells over the time acquired under continuous perfusion and after treatment with 2.5 mM L-Glu for 3 min, as indicated by the white empty box on the x-axis. **(h)** Representative ratiometric images of GLR3.3-1 seedling root tips for three selected time points in response to 2.5 mM L-Glu. **(i)** NES-YC3.6 normalized ratio changes of GLR3.3-1 and **(i')** GLR3.3-2 root tip cells over the time acquired under continuous perfusion and after treatment with 1 mM L-Glu for 3 min, as indicated by the white empty box on the x-axis. **(j)** NES-YC3.6 normalized ratio changes of GLR3.3-1 and **(j')** GLR3.3-2 root tip cells over the time acquired under continuous perfusion and after treatment with 2.5 mM L-Glu for 3 min, as indicated by the white empty box on the x-axis. **(k)** Representative ratiometric images of R550N-1 seedling root tips for three selected time points in response to 2.5 mM L-Glu. **(l)** NES-YC3.6 normalized ratio changes of R550N-1 and **(l')** R550N-2 root tip cells over the time acquired under continuous perfusion and after treatment with 1 mM L-Glu for 3 min, as indicated by the white empty box on the x-axis. **(n)** Representative ratiometric images of D543G-1 seedling root tips for three selected time points in response to 2.5 mM L-Glu. **(o)** NES-YC3.6 normalized ratio changes of D543G-1 and **(o')** D543G-2 root tip cells over the time acquired under continuous perfusion and after treatment with 1 mM L-Glu for 3 min, as indicated by the white empty box on the x-axis. **(p)** NES-YC3.6 normalized ratio changes of D543G-1 and **(p')** D543G-2 root tip cells over the time acquired under continuous perfusion and after treatment with 2.5 mM L-Glu for 3 min, as indicated by the white empty box on the x-axis. **(q)** Maximal peaks of NES-YC3.6 ratio signals for root tip cells after 2.5 mM L-Glu administration. **(r)** same as panel **g**, **m** and **p** but y-axis scales, and ranges adjusted to compare the *glr3.3-1*, R550N-1 and D543G-1 genetic backgrounds. **(s)** Same as panel **q** but y-axis scales, and ranges adjusted showing data only for the *glr3.3-1*, R550N-1 and D543G-1 genetic backgrounds. **(t)** same as panel **g'**, **m'** and **p'** but y-axis scales, and ranges adjusted to compare the *glr3.3-1*, R550N-1 and D543G-1 genetic backgrounds. **(u)** Same as panel **q** but y-axis scales, and ranges adjusted showing data only for the *glr3.3-2*, R550N-2 and D543G-2 genetic backgrounds. Error bars ± SD. ns = not significant, **P* < 0.05, ***P* < 0.01, ****P* < 0.001, *(Student t test)* in comparison to the wt.

The same *Arabidopsis* mutant and complemented lines expressing the NES-YC3.6 were also used to assess the requirement of a functional *At*GLR3.3 LBD in systemic responses. Specifically, we assayed the effect of *At*GLR3.3 LBD mutations on the burning-induced $[Ca^{2+}]_{cyt}$ increase in flower receptacle cells that we showed to be dependent on the activity of *At*GLR3.3 (**Fig. 5f-h**). In response to leaf-burning, a sustained $[Ca^{2+}]_{cyt}$ increase occurred in flower receptacle cells of wt plants ($\Delta R_{max}/R_0$ = 0.2 ± 0.1) (**Fig.11 a, g , h**), confirming the results obtained with the R-GECO1 Ca^{2+} indicator. We then calculated the speed of the signal generating a $[Ca^{2+}]_{cyt}$ increase in the flowers upon leaf burning which was quantified in 1050 ± 560 µm/s. Both *glr3.3-1* and *glr3.3-2* and plants expressing the mutant variants of *At*GLR3.3 (R550N and D543G) showed almost no response to burning (**Fig. 11 b, b', d-e', g ,h**) whereas *glr3.3* mutants complemented with wt *At*GLR3.3 fully rescued the phenotype ($\Delta R_{max}/R_0$ = 0.17 ± 0.09 for GLR3.3-1 and $\Delta R_{max}/R_0$ = 0.3 ± 0.11 for GLR3.3-2) (**Fig. 11c, c', g, h**). With the exception of D543G-2 plants that showed a slightly slower cpVenus/CFP ratio, no statistical differences in the steady-state resting $[Ca^{2+}]_{cyt}$ were observed among the different genetic backgrounds indicating that the presence of *At*GLR3.3 mutated variants does not alter the cytosolic $[Ca^{2+}]_{cyt}$ homeostasis at resting.

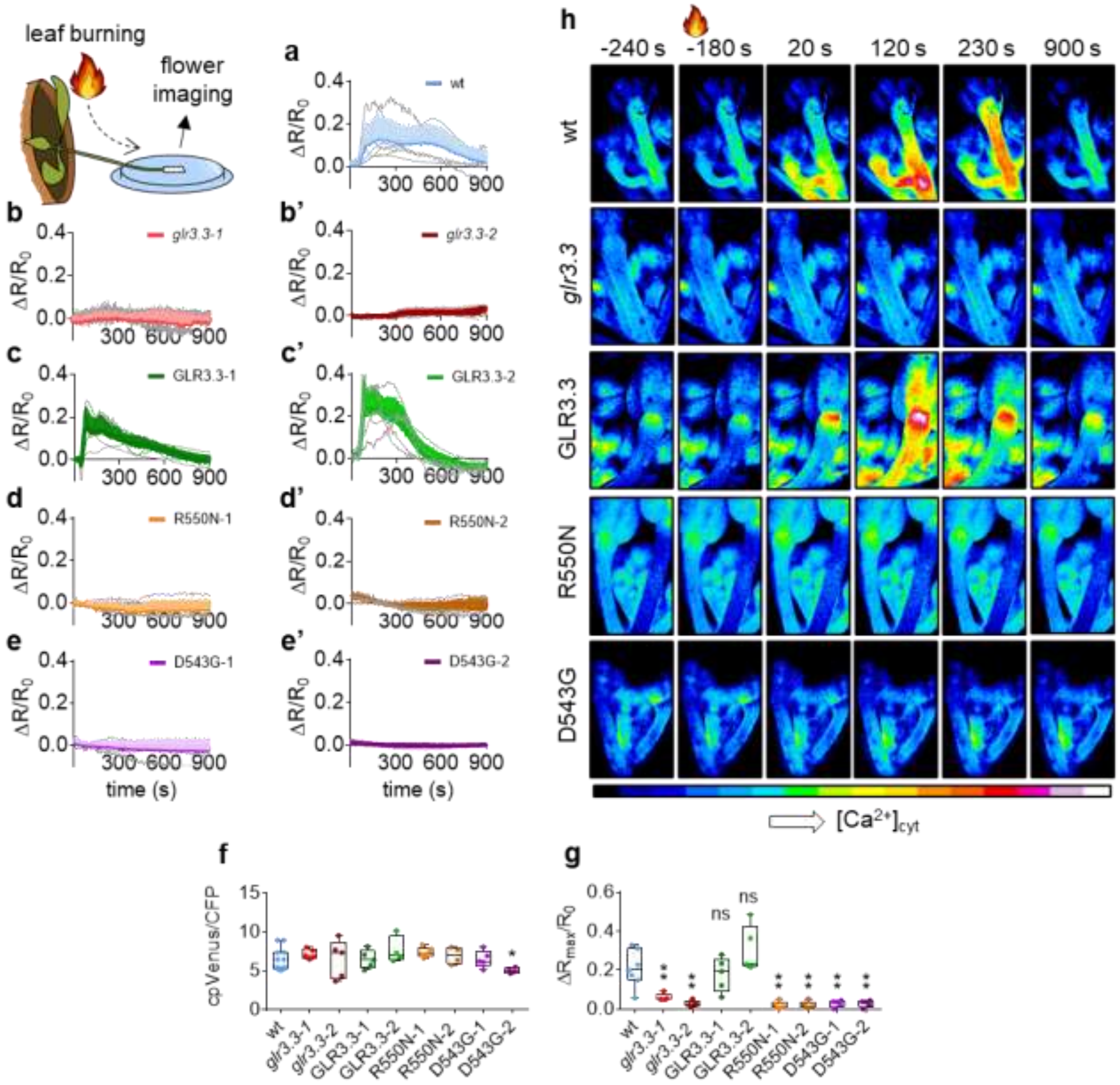

Figure 11. *In planta* functional analysis of the role of *At*GLR3.3 LBD in systemic response to leaf burn. (f) NES-YC3.6 cpVenus/CFP steady-state ratios in root tip cells for Col-0 (wt, light blue), *glr3.3-1* (red), *glr3.3-2* (dark red), *glr3.3-1* x *pGLR3.3::gGLR3.3*$_{wt}$ (GLR3.3-1, dark green), *glr3.3-2* x *pGLR3.3::gGLR3.3*$_{wt}$ (GLR3.3-2, light green), *glr3.3-1 x pGLR3.3::gGLR3.3*$_{R550N}$ (R550N-1, orange), *glr3.3-2 x pGLR3.3::gGLR3.3*$_{R550N}$ (R550N-2, dark orange), *glr3.3-1 x pGLR3-3::gGLR3.3*$_{D543G}$ (D543G-1, purple) and *glr3.3-1 x pGLR3-3::gGLR3.3*$_{D543G}$ (D543G-2, dark purple) genetic backgrounds. **(a)** Schematic drawing of the experimental design and NES-YC3.6 normalized ratio changes of the primary inflorescence for the wt background over the time acquired in response to the burn of one rosette leaf applied at 60 sec from the beginning of the measurement. **(b)** Same as panel **a** but for the *glr3.3-1* background. **(b')** Same as panel **a** but for the *glr3.3-2* background. **(c)** Same as panel **a** but for the GLR3.3-1 background. **(c')** Same as panel **a** but for the GLR3-32 background. **(d)** Same as panel **a** but for the R550N-1 background. **(d')** Same as panel **a** but for the R550N-2 background. **(e)** Same as panel **a** but for the D543G-1 background. **(e')** Same as panel **a** but for the D543G-2 background. **(g)** Maximal peaks of NES-YC3.6 ratio signals of receptacle cells of the primary inflorescence after the burn of one rosette leaf. **(h)** Representative ratiometric images of primary inflorescences for six selected time points with low cpVenus/CFP ratios, in response to the burn of one rosette leaf at 60 sec from the beginning of the measurement. of the measurement. n ≥ 5. Error bars = SD. ns = not significant, *P < 0.05, **P < 0.005 (*Student's t test*).

In conclusion, the data collected so far supported that the *At*GLR3.3 LBD binding bears a functional relevance to the genesis of *At*GLR3.3-dependent $[Ca^{2+}]_{cyt}$ changes induced by both local administration of L-Glu and in the systemic response to leaf-burning. We should assume that the concentration L-Glu reaches in the apoplast of receptacle cells upon leaf-burning is below 2.5 mM, since this quantity is sufficient to activate the $GLR3.3_{D543G}$ variant in root tip cells and any burning-induced $[Ca^{2+}]_{cyt}$-increase in receptacle cells was not observed. It must be said that although qRT-PCR analysis revealed that mutated *At*GLR3.3 variants are expressed in both seedlings and flowers, it cannot be ruled out that the lack of any burning-induced $[Ca^{2+}]_{cyt}$ increase may be due to the lack of the *At*GLR3.3 proteins. This last point should be verified by assessing the presence of *At*GLR3.3 variants (R550N, and D543G) by immunoblot or other proteomic analyses. However, the partial complementation observed in the two *glr3.3* mutant alleles complemented with the $GLR3.3_{D543G}$ variant suggests the presence of a partially active channel at least in root cells.

II.6. In vivo iGluSnFR characterization suggests µM concentrations of L-Glu accumulate systemically in response to mechanical damage

The pioneering work from Gilroy's lab firstly demonstrated that in *Arabidopsis* the mechanical damage of a leaf induces an increase of L-Glu in the apoplast, suggesting that this AA can act as a Damage-associated molecular patterns (DAMPs) that exerts its role trough the *At*GLRs activity to induce a long-distance systemic Ca^{2+} propagation, defence gene expression and JA and JA-ile accumulation (Toyota et al., 2018). In that work, the visualization of the apoplastic release of L-Glu was achieved by using the apoplastic-localized green fluorescent iGluSnFR L-Glu sensor (Marvin et al., 2013) that we also employed for the experiments described above. Based on the *in vivo* calibration performed by the authors they suggested that the concentration of L-Glu required to activate the *At*GLRs ranges from 50 to 100 mM (Toyota et al., 2018), values that are 50-100 times higher than what required in root tip cells (**Fig. 10**). Thus, there are critical issues that must be considered. In general, a calibration curve aims to find a linear relationship between concentration (independent variable) and response (dependent variable) (Moosavi and Ghassabian, 2017) and only the linear part of the calibration curve should be considered. Nevertheless, Toyota et al. extrapolated the $[L\text{-}Glu]_{apo}$ data referring to the non-linear part of the calibration curve they made (Toyota et al., 2018). Moreover, in the original work Marvin et al., performing the *in vitro* calibration of the indicator, demonstrated that the iGluSnFR has a non-linear response with L-Glu concentrations above 1 mM (Marvin et al., 2013). Besides these technical observations, we should also consider the biological aspect. *In vivo*, treatment of *Arabidopsis* leaves or roots with a high concentration of L-Glu (50-100 mM) triggered long-distance Ca^{2+} waves that are dependent on the *At*GLR3.3 activity (Toyota et al., 2018; Shao et al., 2020). The requirement of a so high $[L\text{-}Glu]_{apo}$ (50-100 mM) to induce systemic *At*GLRs-dependent responses odds with both the fact that

*At*GLR3.3-LBD binds L-Glu and other AAs in the low micromolar range and that *in vivo* concentrations as low as 50 µM L-Glu can induce Ca^{2+} increase in *Arabidopsis* root cells (Stephens et al., 2008; Alfieri et al., 2020). Last but not least, the lack of burning-induced $[Ca^{2+}]_{cyt}$ response in receptacle cells of plant expressing the $GLR3.3_{D543G}$ variant, which is activated at 2.5 mM L-Glu, suggests that $[L\text{-}Glu]_{apo}$ reached in the apoplast is well below the concentration considered necessary (50 mM) to activate *At*GLRs. To shed light on these discrepancies, we performed an *in vivo* calibration of iGluSnFR by performing a dose-dependent response in *Arabidopsis* root tip cells. iGluSnFR seedlings were placed in an imaging chamber and the L-Glu was administered at different concentrations (10, 50, 100, 250, 500, 1000, 5000 µM) by mean of a perfusion system to finely control the AA concentration. A clear increase in the iGluSnFR fluorescence was observed for every tested concentration in root tip cells, with a progressive increase of the normalized fluorescence change from 10 µM ($\Delta F/F_0 = 0.08 \pm 0.01$) to 250 µM ($\Delta F/F_0 = 0.58 \pm 0.11$) (**Fig. 12a, b**). No statistical differences were observed at concentrations above 500 µM (**Fig. 12a, b**). We conclude that in our hands the iGluSnFR sensor is already saturated at concentrations ranging from 250 µM to 500 µM and cannot correctly report higher $[L\text{-}Glu]_{apo}$. Importantly our data are in good agreement with the *in vitro* analysis reported by Marvin et al. (Marvin et al., 2018). We then decided to use the dose-dependency data obtained in root to roughly evaluate the amount of L-Glu necessary to activate *in vivo AtGLRs* in systemic tissues upon mechanical damage. The data from the dose-dependent response were used to produce a fluorescence titration curve for the iGluSnFR sensor. This way of plotting the data showed that the sensor has *in vivo* a linear response, evaluated as $\Delta F/F_0$ increase, from 10 µM to 100 µM L-Glu (**Fig. 12c**). In the experiments described above, in response to leaf-burning a clear increase in $[Ca^{2+}]_{cyt}$ of flower receptacle cells was observed when the fluorescence change ($\Delta F/F_0$) of the iGluSnFR reached values of 0.11 ± 0.03 (**Fig. 2g**). Thus, based on our *in vivo* calibration of the iGluSnFR a $\Delta F/F_0 = 0.11$ corresponds to tens of µM of L-Glu (**Fig. 12d**), which is orders of magnitude lower than what previously suggested (Toyota et al., 2018; Shao et al., 2020; Grenzi et al., 2021a). These data agree with the lack of any detectable $[Ca^{2+}]_{cyt}$ increase in the cells of the flower receptacle of plant expressing the $GLR3.3_{D543G}$ variant subjected to leaf burning, since with this line, in root tip cells, a response was observed after the administration of 2.5 mM L-Glu. Nonetheless, a value of tens of µM of L-Glu better correlates with the *in vitro* binding affinity data of *At*GLR3.3-LBD (L-Glu $K_d = 2.2 \pm 0.5$µM) (Alfieri et al., 2020), and with the requirement of as low as 50 µM L-Glu required to trigger a $[Ca^{2+}]_{cyt}$ increase in the root cells of wt plants (Alfieri et al., 2020). Overall, despite the fact that the *in vivo* calibration is affected by uncertainty, we tentatively suggest that in response to leaf-burning there is a rise in the $[L\text{-}Glu]_{apo}$ of flower receptacle cells in the high micromolar range.

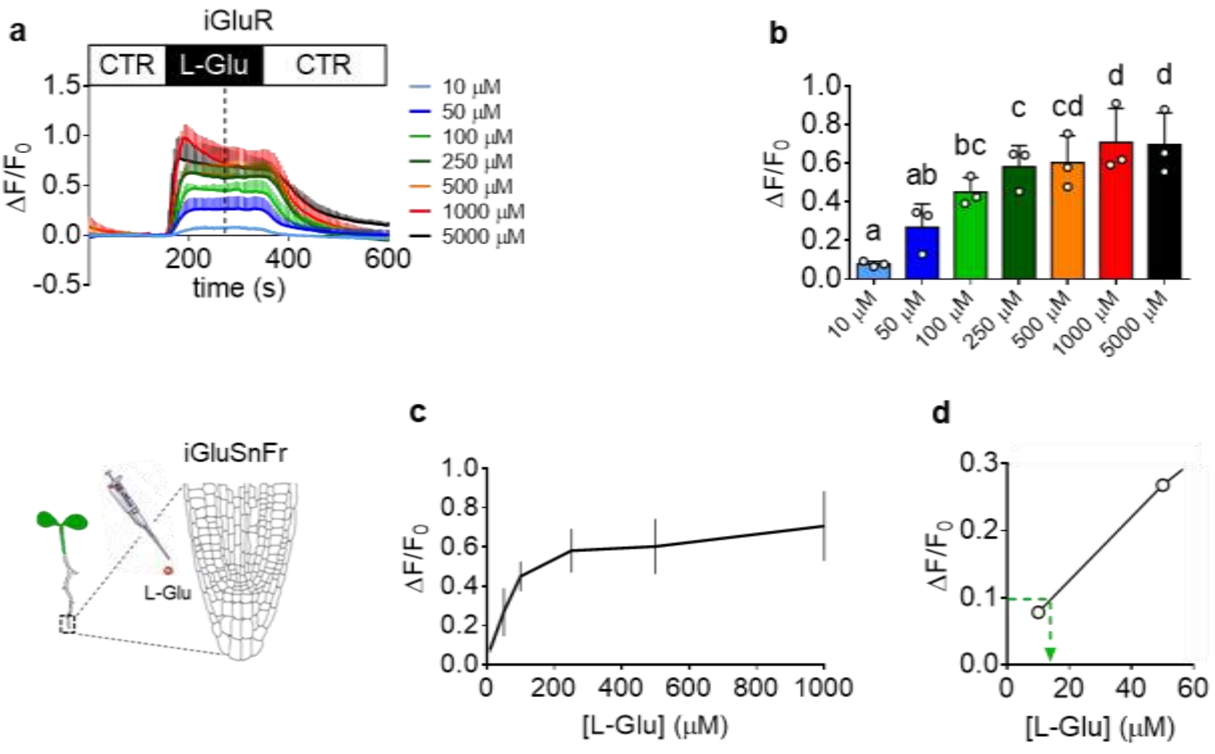

Figure 12. ***In vivo*** **calibration of iGluSnFR in root tip cells in seedlings of** ***Arabidopsis thaliana*****. (a)** Schematic drawing of the experimental design and normalized iGluSnFR fluorescence changes in *Arabidopsis thaliana* root tip cells in response to pulses of different concentrations of L-Glu. **(b)** Dose-dependency of the iGluSnFR signal in root cells. Values were taken from panel **a** at 90 sec after the L-Glu administration. **(c)** same as panel **b** represented as a trace. **(d)** same as panel **c** but x-axis, y-axis scales, and ranges adjusted. n ≥ 5. Error bars = SD. Bars marked with different letters are significantly different (*P < 0.05*) by one-way ANOVA with Tukey-Kramer test.

II.7. Local delivery of µM concentrations of L-Glu into leaf tissues does not trigger systemic propagating $[Ca^{2+}]_{cyt}$ waves

As reported above we previously demonstrated that the recombinant *At*GLR3.3 LBD binds L-Glu with an affinity of 2.2 ± 0.5 µM *in vitro* and as low as 50 µM of L-Glu triggers a local, *At*GLR3.3-dependent $[Ca^{2+}]_{cyt}$ increase in *Arabidopsis* root tip cells (Alfieri et al., 2020). Moreover, our rough estimations predict that in flowers the leaf burning induces $[L\text{-}Glu]_{apo}$ increase in the range of hundreds of µM. However, in previous works the administration of 50 to 100 mM of exogenous L-Glu to pre-wounded *Arabidopsis* leaf or root tissues showed to induce long-distance Ca^{2+} waves (Toyota et al., 2018; Shao et al., 2020; Moe-Lange et al., 2021). To investigate whether exogenous µM concentrations of L-Glu can trigger propagating Ca^{2+} waves *per se*, we employed a system that allows to administer L-Glu to a leaf of *Arabidopsis* minimizing side effects due to wounding. To do so we made use of an implantable bioelectronic device, the capillary-based organic electronic ion pump (c-OEIP, schematically reported in **Fig. 13a**), which enables the electrophoretic delivery of charged molecules without liquid flow in the leaf avoiding a significant wound response (Bernacka-Wojcik et al., 2019). Thanks to an optimised c-OEIP addressing protocol (adjustment of pH of source electrolyte and operating at low delivery current), the miniaturised c-OEIP with a tip diameter of 150 µm, has significantly higher L-Glu delivery efficiency than standard planar OEIPs (Simon et al., 2009). The mass spectrometry analyses showed that the c-OEIP operating at a constant current of 150 nA was able to deliver 111.61 ± 1.09 pmol/min of L-Glu (**Fig. 13b**) *in vitro*. At first, to assess the existence of any possible damage of the leaf tissues associated with the c-OEIP implantation, we performed a series of analyses. By inserting the c-OEIP in the proximity of the primary vasculature of *Arabidopsis* mature leaves expressing the Ca^{2+} indicator R-GECO1 (**Fig. 13c, d**) we observed a $[Ca^{2+}]_{cyt/nuc}$ rise ($\Delta F/F_0 = 0.25 \pm 0.12$) that covered an area of 3.24 ± 0.33 mm^2 around the insertion site (**Fig. 13d-g**). Analysis of a region of interest distant 3 mm in basipetal direction from the insertion site did not show any $[Ca^{2+}]_{cyt/nuc}$ increase (**Fig. 13 c, e, f**). This result shows that the c-OEIP implantation induces a small localised $[Ca^{2+}]_{cyt/nuc}$, without triggering a systemic $[Ca^{2+}]_{cyt/nuc}$ response, which is observed when a larger area is wounded (**Fig. 1**). Next, we implanted the c-OEIP in *Arabidopsis* mature plant leaves expressing both the iGluSnFR and the R-GECO1 indicators and assessed the effect of the active L-Glu delivery. With the electrical potential application to the c-OEIP the L-Glu should start to be delivered and accumulate in the leaf apoplast. Indeed upon the c-OEIP activation an increase in the $[\text{L-Glu}]_{apo}$ was observed ($\Delta F/F_0 = 0.38 \pm 0.25$) (**Fig. 13h-k**). The $[\text{L-Glu}]_{apo}$ fluorescence emission increase remained confined to an area of 1315 ± 315 µm around the implantation site (L), suggesting that L-Glu delivered does not diffuse to regions distant (D) from the implantation site. Importantly, delivery of D-Glu enantiomer, of which mass spectrometry analyses showed an *in vitro* delivery efficiency similar to L-Glu (**Fig. 13b**), did not induce any change in the iGluSnFR fluorescence (**Fig. 13k**). This pointed out that the registered L-Glu-induced change of iGluSnFR fluorescence was not due to artefacts and that c-OEIP efficiently delivers L-Glu *in vivo*. Similarly, the delivery of L-Glu triggered a clear R-GECO1 fluorescence increase in L (**Fig. 13l-o**) that went over the $[Ca^{2+}]_{cyt/nuc}$ increase induce by the sole c-OEIP implantation (**Fig. 13d-f**). On the contrary, in the ROI D no L-Glu-induced $[Ca^{2+}]_{cyt/nuc}$ increase was detected (**Fig. 13l-o**). The R-GECO1 fluorescence was not affected by the c-OEIP delivery of D-Glu, indicating the specificity of the response to L-Glu (**Fig. 13o**). Altogether these data show that the local delivery of low amount of L-Glu (111.61 ± 1.09 pmol/min) in the leaf apoplast is sufficient to induce a local $[Ca^{2+}]_{cyt/nuc}$ increase but not a propagating Ca^{2+} wave. Despite the genetic evidence is still lacking, the involvement of GLRs in the observed L-Glu-induced $[Ca^{2+}]_{cyt/nuc}$ increase can be postulated. If this were the case, it would mean that the local GLRs activation is not *per se* sufficient to trigger a systemic Ca^{2+} response but that other factors besides the local wound-induced release of L-Glu are involved.

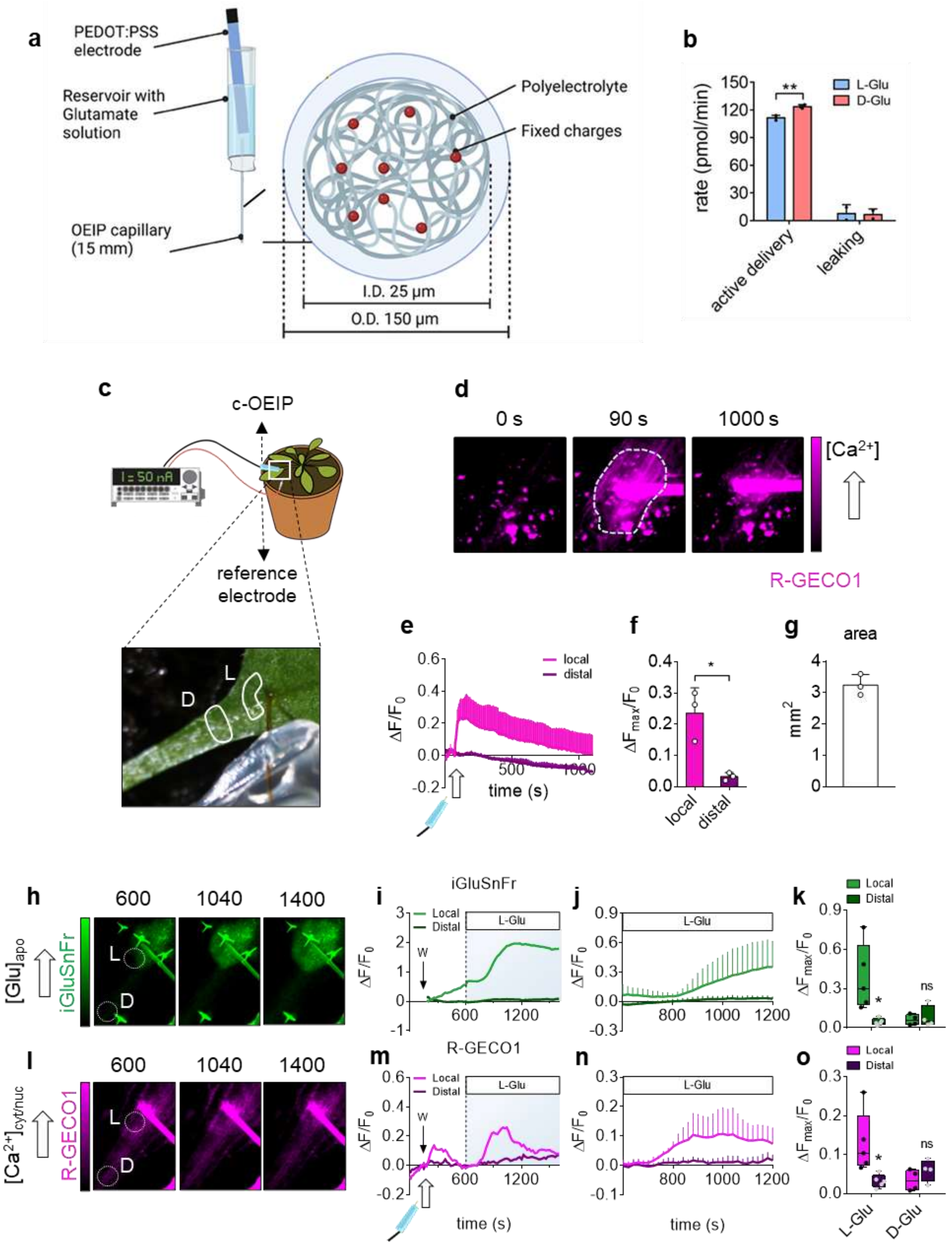
a
PEDOT:PSS electrode
Reservoir with Glutamate solution
OEIP capillary (15 mm)
Polyelectrolyte
Fixed charges
I.D. 25 µm
O.D. 150 µm
b
rate (pmol/min)
150
120
90
60
30
0
**
L-Glu
D-Glu
active delivery
leaking
c
c-OEIP
I = 50 nA
reference electrode
L
D
d
0 s
90 s
1000 s
[Ca2+]
R-GECO1
e
ΔF/F0
0.6
0.4
0.2
0.0
-0.2
local
distal
500
1000
time (s)
f
ΔFmax/F0
0.4
0.3
0.2
0.1
0.0
*
local
distal
g
area
mm2
4
3
2
1
0
h
600
1040
1400
[Glu]apo
iGluSnFr
L
D
i
iGluSnFr
Local
Distal
L-Glu
W
ΔF/F0
3
2
1
0
-1
600
1200
j
L-Glu
ΔF/F0
0.9
0.6
0.3
0.0
-0.3
800
1000
1200
k
Local
Distal
ΔFmax/F0
0.9
0.6
0.3
0.0
*
ns
l
600
1040
1400
[Ca2+]cyt/nuc
R-GECO1
L
D
m
R-GECO1
Local
Distal
L-Glu
W
ΔF/F0
0.6
0.4
0.2
0.0
-0.2
600
1200
time (s)
n
L-Glu
ΔF/F0
0.3
0.2
0.1
0.0
-0.1
800
1000
1200
time (s)
o
Local
Distal
ΔFmax/F0
0.3
0.2
0.1
0.0
*
ns
L-Glu
D-Glu

Figure 13. Delivery of L-Glu with an Implantable Organic Electronic Ion Pump (c-OEIP) induces local cytosolic Ca^{2+} concentration increase. (a) Schematic of the implanted c-OIEP into Arabidopsis leaf. The capillary is fixed to a shrinking tube that contains the water-based solution of D- or L-Glu. The cross-section of the c-OEIP is also shown, illustrating the polyelectrolyte matrix with the exposed fixed (positive) charges. **(b)** c-OEIP delivery rate for L- and D-Glu, as quantified with Mass Spectrometry, for operation current at 150 nA for 30 minutes and during leakage for 10 minutes as a control. The leakage delivery was assessed without applying any current on the c-OEIP. One over three measurements for the quantification of the leakage delivery for both L-Glu and D-Glu were under the limit of detection, therefore, only two measurements are shown in the graph. **(c)** Experimental setup for *in vivo* delivery of L-Glu using c-OEIP in intact leaves. **(d)** Examples of false-colour images illustrate R-GECO1 fluorescence (magenta) in one rosette leaf implanted with an empty c-OEIP capillary. **(e)** R-GECO1normalized fluorescence changes in local (L) and distal (D) Regions of interest (ROIs) (indicated in **c**) over the time after the c-OEIP implantation. **(f)** The maximal peak of R-GECO1 normalized fluorescence in L and D after the empty c-OEIP implantation. **(g)** Area showing an increase in the R-GECO1 fluorescence upon c-OEIP implantation (white dashed line in **d**). **(h, l)** Examples of false-colour images illustrate iGluSnFR (green) and R-GECO1 (magenta) in one rosette leaf implanted with the c-OEIP capillary. **(i)** iGluSnFR normalized fluorescence changes of the local (L) and distal (D) Regions of Interest over the time after the c-OEIP implantation and starting of L-Glu delivery as indicated by the white empty box on the x-axis. **(j)** Same as **i** but x-axis, y-axis scales, and ranges adjusted **(k)** Maximal peaks iGluSnFR normalized fluorescence after the c-OEIP L-Glu and D-Glu delivery.**(m)** R-GECO1 normalized fluorescence changes of the local (L) and distal (D) Regions of Interest over the time after the c-OEIP implantation and starting of L-Glu delivery as indicated by the white empty box on the x-axis. **(n)** Same as **i** but x-axis, y-axis scales, and ranges adjusted **(o)** Maximal peaks R-GECO1 normalized fluorescence after the c-OEIP L-Glu and D-Glu delivery. n = 4. Error bars = SD. ns = not significant, $*P < 0.05$, $**P < 0.005$ *(Student's t-test)*.

II.8. Leaf-burning induces the bending of the stem independently from AtGLR3.3 activity

The data presented so far support a model according to which mechanical damage, such as wounding and burning, trigger an apoplastic accumulation of L-Glu in systemic tissues that in turn it is bound by the LBD of *At*GLR3.3, which is required for the $[Ca^{2+}]_{cyt/nuc}$ increase. At the damaged site, it is easy to think that the cell damage can lead to the release in the apoplast of the intracellular content (Vega-Muñoz et al., 2020), as suggested by Toyota et al. (Toyota et al., 2018). However, the events underlying the systemic activation of GLRs and specifically the mechanisms leading to the accumulation of apoplastic L-Glu in systemic tissues (and possibly other molecules) are unknown. Nevertheless, a clue came by the observation that in response to leaf-burning a clear bending of the primary inflorescence occurred, suggesting that the leaf damage can lead to a change in the plant turgidity. In order to better characterize this event and link it to the GLRs activation and the Ca^{2+} increase, *Arabidopsis* mature plants at the bolting stage expressing the Ca^{2+} indicator GCaMP3 (Vincent et al., 2017) were challenged by leaf-burning and then imaged with a stereomicroscope with a 5 sec frame rate acquisition (**Fig. 14a**). Such an experimental design allowed us to perform $[Ca^{2+}]_{cyt}$ imaging analysis while at the same time looking and quantifying the movement of the primary stem. We observed that the primary inflorescence stem underwent a flexion toward the burned leaf, with a massive $[Ca^{2+}]_{cyt/nuc}$ increase propagating through the entire plant body (**Fig. 14a**). The extent of the bending (defined as ΔX in **Fig. 14b**) was then quantified by performing the image registration using as reference a region of interest (ROI) at the base of the inflorescence stem (yellow square in **Fig. 14a**). Moreover, in the same ROI the GCaMP3 fluorescence (reported as $\Delta F/F_0$) was measured in order to solve the temporal hierarchy between the stem bending and the $[Ca^{2+}]_{cyt/nuc}$ response (**Fig. 14a-c'**). Correlation of the two parameters (ΔX and $\Delta F/F_0$) revealed that

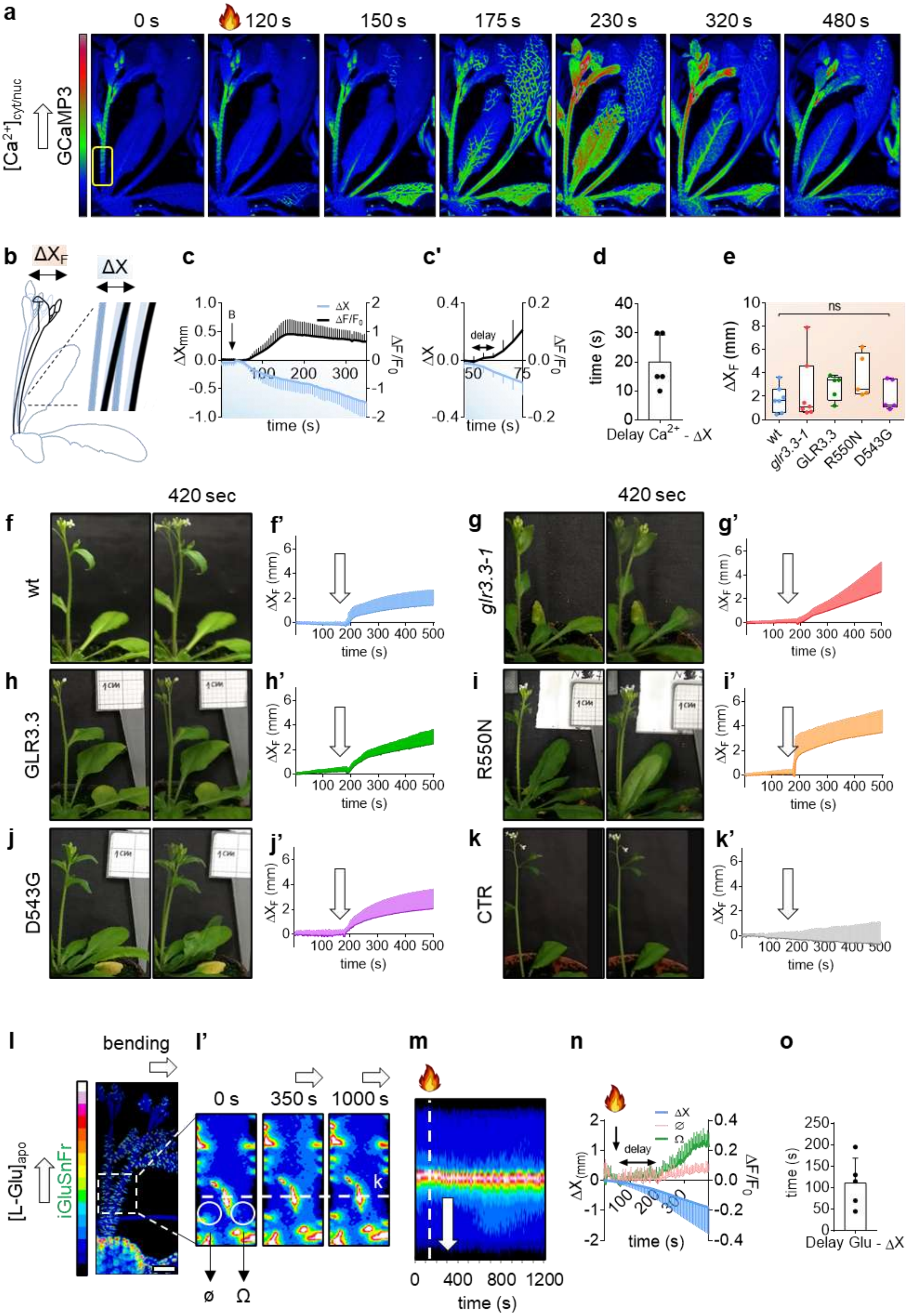
a
0 s
120 s
150 s
175 s
230 s
320 s
480 s
$[Ca^{2+}]_{cyt/nuc}$
GCaMP3
b
ΔX_F
ΔX
c
B
ΔX
$\Delta F/F_0$
ΔX_{mm}
1.0
0.5
0.0
-0.5
-1.0
100 200 300
time (s)
2
1
0
-1
-2
c'
0.4
0.0
-0.4
delay
50 75
0.2
0.0
-0.2
d
40
30
20
10
0
time (s)
Delay Ca^{2+} - ΔX
e
10
8
6
4
2
0
ΔX_F (mm)
ns
wt
glr3.3-1
GLR3.3
R550N
D543G
420 sec
f
wt
f'
g
glr3.3-1
g'
h
GLR3.3
h'
i
R550N
i'
j
D543G
j'
k
CTR
k'
1 cm
ΔX_F (mm)
6
4
2
0
100 200 300 400 500
time (s)
l
bending
$[L\text{-}Glu]_{apo}$
iGluSnFr
l'
0 s
350 s
1000 s
k
ø
Ω
m
0 400 800 1200
time (s)
n
ΔX
ø
Ω
delay
$\Delta X_{(mm)}$
2
1
0
-1
-2
100 200 300
time (s)
0.4
0.2
0.0
-0.2
-0.4
$\Delta F/F_0$
o
250
200
150
100
50
0
time (s)
Delay Glu - ΔX

Figure 14. The *At*GLR3.3 dependent cytosolic Ca^{2+} concentration increase temporally follows the primary inflorescence stem movements, induced by the burn of one rosette leaf. (a) Examples of false-colour images illustrate GCaMP3 fluorescence (green fire blue lookup tables) of the basal rosette and primary inflorescence in response to the burn of one leaf applied at 120 sec. Scale bar = 4 mm. **(b)** schematic drawing showing the approach followed to evaluate the movement at the base of the stem (yellow rectangle in **a** and reported as ΔX in **c** and **h**) or at the top of the inflorescence (ΔX_F in **e**) induced by the burn of one rosette leaf. **(c)**, GCaMP3 normalized fluorescence changes and ΔX movement quantified in the region indicated by the yellow rectangle over the time after the burn of one rosette leaf (B). **(c)'** Same as panel **c** but x-axis, y-axis scales, and ranges adjusted. **(d)** Mean delay of the fluorescence increase of the GCaMP3 following the start of the stem movement after the burn of one rosette leaf. **(e)** Quantification in different genetic backgrounds of the stem movement, reported as ΔX_F, induced by the burn of one rosette leaf. **(f, h, j, g, l, k)** Representative images at different time points of 5-weeks-old *Arabidopsis* plants subjected to the burn of one rosette leaf in different genetic backgrounds. **(f', h', j', g', l. k')** ΔX_F quantification of the movement of the primary inflorescence stems over the time after the burn of one rosette leaf represented as averages of traces from all single experiments in the different genetic backgrounds. **(l)** Examples of false-colour images illustrate iGluSnFR fluorescence (16_colors lookup tables) of the primary inflorescence stem in response to the burn of one leaf applied at 120 sec. Scale bar = 1 mm. **l',** magnification of **l** at different time points. ø and § right and left sides Regions of Interest (white circles) of the stem considered for the quantification of the iGluSnFR fluorescence emission changes over time reported in **n**. The bright spots correspond to the trichomes. **(m)** Kymograph extracted from iGluSnFR fluorescence signals frames by observing the temporal evolution of the pixel with dashed line shown in **l'**. **(n),** iGluSnFR normalized fluorescence changes and ΔX movement quantified in the ø and § regions indicated by the white circles over the time after the burn of one rosette leaf. **(o)** Mean delay of the fluorescence increase of the iGluSnFR following the start of the stem movement after the burn of one rosette leaf. n ≥ 5. Error bars = SD. ns = not significant, *(Student's t-test)*

stem bending precedes the $[Ca^{2+}]_{cyt/nuc}$ increase by 20 ± 9 sec (**Fig. 14c-d**). Being the systemic burning-induced $[Ca^{2+}]_{cyt/nuc}$ increase dependent on the *At*GLR3.3 activity, at least in flower receptacle cells (**Fig. 11b, b', g**), we hypothesized that stem bending can occurs upstream of *At*GLR3.3 activation. In addition, by repeating the same experiment with the iGluSnFR line, we observed that in response to the leaf burning the stem bending anticipated an asymmetric $[L\text{-}Glu]_{apo}$ increase (**Fig. 14l-o**). Noticeably, the $[L\text{-}Glu]_{apo}$ increase occurred on the same side of the stem bending direction (**Fig- 14l-m**). To confirm the hypothesis that the *At*GLR3.3 activation is downstream of both stem bending and $[L\text{-}Glu]_{apo}$ increase, we compared the extent of the burning-induced bending of wt plants with that of both *glr3.3-1* and plants expressing the different *At*GLR3.3 variants. In this case, the extent of the bending (defined as ΔX_F in **Fig. 14b**) was measured by image registration of a reference ROI drawn at the inflorescence apex. When challenged by leaf-burning, the stem of wt plants bended toward the treated leaf and the movement of the inflorescence apex was quantified as $\Delta X_F = 1.77 \pm 1.1$ mm (**Fig. 14e-f'**). No statistical differences were observed in the pattern and the entity of the bending among the different genetic backgrounds ($\Delta X_F = 1.58 \pm 1.51$ for *glr3.3-1*, $\Delta X_F = 2.78 \pm 1.1$ for GLR3.3-1, $\Delta X_F = 3.7 \pm 1.9$ for R550N-1, $\Delta X_F = 2.1 \pm 1.3$ for D543G-1) (**Fig. 14e-k'**). Overall, we demonstrated that in response to leaf-burning the bending of the inflorescence stem occurs upstream of the $[Ca^{2+}]_{cyt/nuc}$ increase and that it is independent from the *At*GLR3.3 activity. We therefore thought that bending could correlate to the systemic *At*GLRs activation.

II.9. Hypo-osmotic stress triggers systemic root-to-shoot [L-Glu]$_{apo}$ and AtGLR3.3-dependent [Ca^{2+}]$_{cyt/nuc}$ waves

Malone & Stankovic (1991) demonstrated that in wheat, localized burning of a leaf causes an increase in turgor pressure in epidermal cells of systemic leaves and that this phenomenon was due to a rapid propagation, throughout the seedling, of a hydraulic pressure wave from the site of wounding. It has also been reported that leaf burn triggers a change in the stem thickness and deformation in *Nicotiana tabacum*[35]. Moreover, Kurenda and colleagues[16] demonstrated that in *Arabidopsis* the petioles of undamaged leaves undergo minute deformations when herbivory insects feed on the other leaves. It is reasonable to suppose that the wound- or burn-induced change in the hydraulic pressure that is responsible for the reported leaf movement and deformation could be also responsible for the increase of [L-Glu]$_{apo}$ in systemic tissues. Basu and Haswell developed a protocol to induce cell swelling by applying to *Arabidopsis* seedling a huge hypo-osmotic stress. (Basu and Haswell, 2020). Cell swelling was shown to induce programmed cell death, ROS accumulation, the transient elevation of cytoplasmic Ca^{2+}, and the expression of mechano-inducible genes (Basu and Haswell, 2020). Motivated by the possibility that changes in hydraulic pressure may be the cause of the apoplastic L-Glu accumulation, we implemented the protocol developed by Basu and Haswell to assess the direct effect of osmotic stress on both [L-Glu]$_{apo}$ and [Ca^{2+}]$_{cyt/nuc}$ dynamics in mature plants (**Fig. 15a**). Mature iGluSnFR x R-GECO1 wt and *glr3.3-1* plants grown for 3 weeks in hydroponic solution (Gibeaut et al., 1997) were transferred for 4 hours in the same hydroponic solution with the addition of 500 mM D-Sorb. To test the effect of the hypo-osmotic stress, the osmolyte was quickly removed by using a perfusion system. To assess the effects of this stress on systemic tissues, the plants were imaged with the stereomicroscope and the fluorescence emissions of both R-GECO1 and iGluSnFR were recorded in the rosette leaves during the washout of the osmolyte (**Fig. 15a, b**). At first, within a few seconds after the D-Sorb washout the [L-Glu]$_{apo}$ increased in the rosette leaves of both wt and *glr3.3-1* plants (**Fig. 15b-e**). At second, once the iGluSnFR fluorescence emission reached a $\Delta F/F_0 = 0.08 \pm 0.02$ in wt plants a clear [Ca^{2+}]$_{cyt/nuc}$ increase was observed (**Fig. 15c, f-h**), whereas the [Ca^{2+}]$_{cyt/nuc}$ rise was completely abolished in *glr3.3-1* plants (**Fig. 15d-f**). Notably, the iGluSnFR fluorescence increase of $\Delta F/F_0 = 0.08 \pm 0.02$ was close to the value measured in flowers in response to leaf burning ($\Delta F/F_0 = 0.11 \pm 0.03$). Overall this experiment shows that an hypo-osmotic stress applied to the root is able to induce systemically an increase of both [L-Glu]$_{apo}$ and [Ca^{2+}]$_{cyt/nuc}$, where the systemic Ca^{2+} increase is dependent on the activity of *At*GLR3.3 (**Fig 15e**). However, by looking at the iGluSnFR fluorescence emission in the wt It was interesting to observe that the apoplastic L-Glu increase was biphasic, with a first phase (**0-250 seconds in Fig.15i, l**) that anticipated the [Ca^{2+}]$_{cyt/nuc}$ increase (magenta line in **Fig. 15i**) and a second one that followed it with a more rapid slope reaching the maximum peak at around 600 seconds (**Fig. 15 c, i, l**). In the first phase, no statistical differences in the [L-Glu]$_{apo}$ of wt and *glr3.3-1* were observed meanwhile *glr3.3-1* plants did not show the second phase of apoplastic L-Glu accumulation (**Fig. 15i, l**).

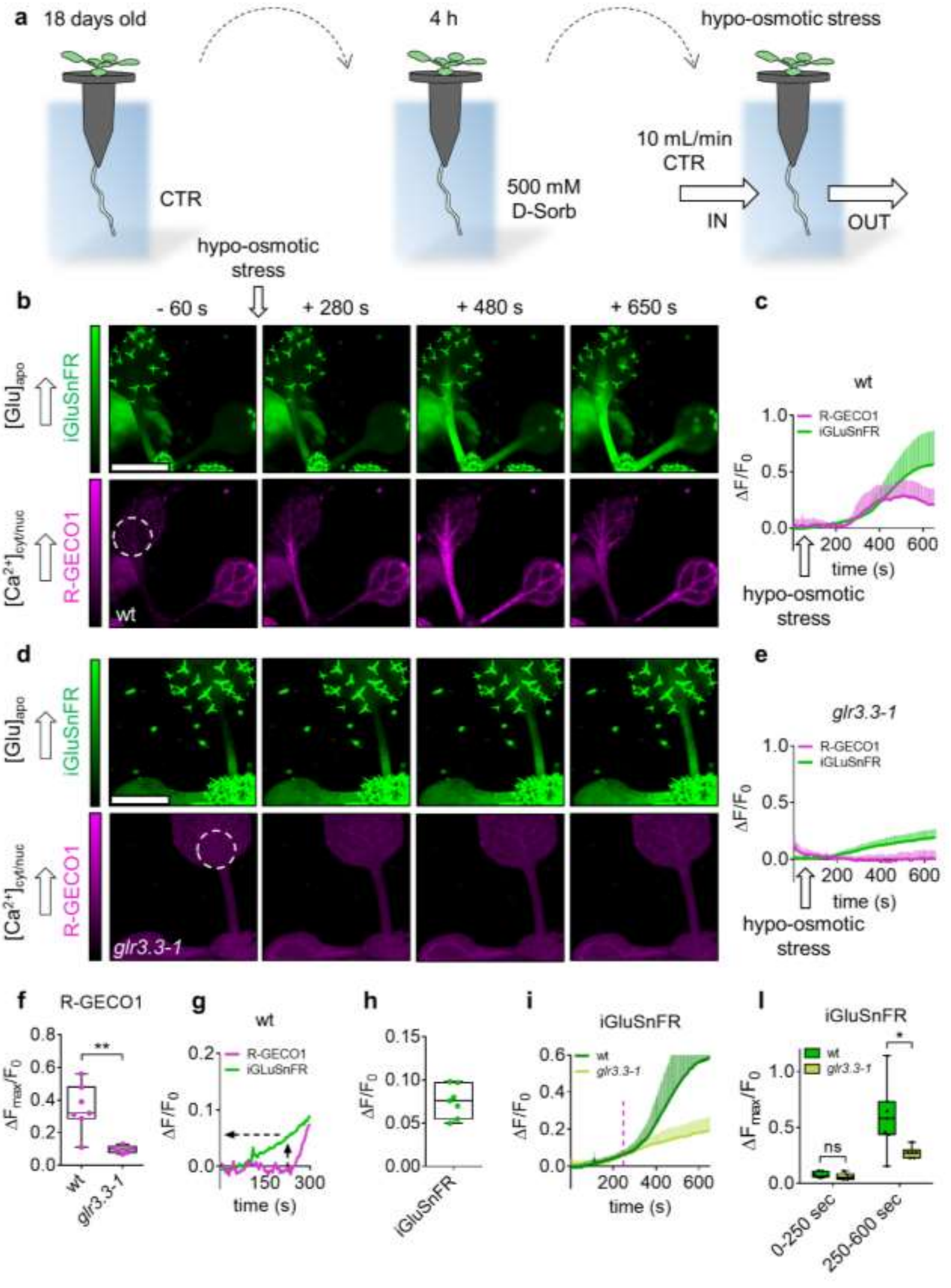
a
18 days old
4 h
hypo-osmotic stress
CTR
500 mM D-Sorb
10 mL/min CTR
IN
OUT
hypo-osmotic stress
b
- 60 s
+ 280 s
+ 480 s
+ 650 s
[Glu]apo
iGluSnFR
[Ca2+]cyt/nuc
R-GECO1
wt
c
wt
R-GECO1
iGLuSnFR
ΔF/F0
1.0
0.5
0.0
200
400
600
time (s)
hypo-osmotic stress
d
[Glu]apo
iGluSnFR
[Ca2+]cyt/nuc
R-GECO1
glr3.3-1
e
glr3.3-1
R-GECO1
iGLuSnFR
ΔF/F0
1.0
0.5
0.0
200
400
600
time (s)
hypo-osmotic stress
f
R-GECO1
ΔFmax/F0
0.8
0.6
0.4
0.2
0.0
**
wt
glr3.3-1
g
wt
R-GECO1
iGLuSnFR
ΔF/F0
0.2
0.1
0.0
150
300
time (s)
h
ΔF/F0
0.15
0.10
0.05
0.00
iGluSnFR
i
iGluSnFR
wt
glr3.3-1
ΔF/F0
0.6
0.4
0.2
0.0
200
400
600
time (s)
l
iGluSnFR
wt
glr3.3-1
ΔFmax/F0
1.0
0.5
0.0
*
ns
0-250 sec
250-600 sec

Figure 15. Hypo-osmotic stress triggers systemic root-to-shoot [L-Glu]$_{apo}$ and *At*GLR3.3-dependent [Ca^{2+}]$_{cyt/nuc}$ waves (a) schematic drawing of the experimental desig. Plants grown in hydroponic (CTR) were transferred for 4 hours in the same hydroponic solution with the addition of 500 mM D-Sorb, subsequently the osmolyte was rapidly washed out by using a perfusion system. **(b)** Examples of false-colour images illustrate iGluSnFR (green) and R-GECO1 (magenta) in a leaf of a wt plant treated with hypoosmotic stress. Scale bar = 7 mm. **(c)** iGluSnFR and R-GECO1 normalized fluorescence changes in a Region of Interes (ROI) of a leaf (white dashed circle) over the time of a wt plant after hypoosmotic stress (white arrow).**(d)** Same as **b** but in the *glr3.3-1* genetic background. **(e)** Same as **c** but in the *glr3.3-1* genetic background.**(f)** Maximal peaks of the R-GECO1 fluorescence signal in the a leaf of wt and *glr3.3-1* plants after hypoosmotic stress. **(g)** Same as **c** but x-axis, y-axis scales, and ranges adjusted. **(h)** Mean normalized iGluSnFR fluorescence change at which an increase of the R-GECO1 fluorescence is observed in wt plants. **(i)** iGluSnFR normalized fluorescence changes in a Region of Interes (ROI) of a leaf (white dashed circle) over the time of wt and glr3.3-1 plant after hypoosmotic stress (white arrow). **(l)** Maximal peaks of the iGluSnFR fluorescence signal in a leaf of wt and *glr3.3-1* plants after hypoosmotic stress calculated over different time windows.

This latter result needs to be considered with caution but it could represent an interesting observation that will deserve further analyses. Indeed, we can exclude a reduced functionality of iGluSnFR in the *glr3.3-1* genetic background, since in response to wounding the readout was the same of wt plants (**Fig. 1h, p**). On the other hand it is known that Ca^{2+} signals are intimately connected with pH changes (Behera et al., 2018) and we cannot rule out that pH changes following the [Ca^{2+}]$_{cyt/nuc}$ increase may affect the iGluSnFR fluorescence, for which a pH sensitivity has been shown (Marvin et al., 2013). Excluding technical artefacts, the possibility that [Ca^{2+}]$_{cyt/nuc}$ signals induce a further release of L-Glu in a self-sustained mechanism would be an astonishing scenario on which more efforts need to be made.

Chapter III. Conclusions and future perspectives

Permanently restricted to their site of germination, plants evolved mechanisms to react to ever-changing environmental conditions and harmful stresses. Local damage triggers inducible defence mechanisms that are often induced systemically in organs that are not damaged yet. In *Arabidopsis thaliana*, wounding and herbivore feeding trigger long-distance variation potentials (VPs) and Ca^{2+} waves that propagate from the injured leaf to systemic organs. Long-distance VPs and Ca^{2+} waves propagation are dependent on GLRs, whose activity is required to guide the biosynthesis of the defence hormone JA in unharmed tissues. Despite considerable genetic evidence on GLRs requirement in long-distance signalling, their mechanism of action in plants is not defined. Since the animal homologous iGluRs are PM-located ligand-gated non-selective cation channels activated by the binding to L-Glu, we investigated whether a similar scenario could govern the activation of plant GLRs. Here we showed that in response to wounding L-Glu appears to accumulate in the apoplast at the wounded leaf, as well as in systemic leaves. As opposed to the increase in $[Ca^{2+}]_{cyt/nuc}$, the L-Glu accumulation in systemic tissues is independent of the *AtGLR3.3* activity. A novel protocol designed to study long-distance signalling in *Arabidopsis* inflorescence at a high spatiotemporal resolution revealed that in flower receptacle cells leaf-burning triggers an $[L\text{-}Glu]_{apo}$ increase anticipating the subsequent $[Ca^{2+}]_{cyt/nuc}$. Moreover, we demonstrated that leaf-burning induces a wound-like response in systemic tissues that induces the expression of the JA-responsive *JAZ10* marker gene. *AtGLR3.3* was found to be expressed in flower receptacles and in the phloem of the primary inflorescence stem, in which it acts as a molecular determinant of the burning-induced systemic $[Ca^{2+}]_{cyt}$ increase. In fact, the cytosolic Ca^{2+} increase of flower receptacle cells upon leaf-burning was strongly impaired in the *glr3.3* mutants. Moreover, we demonstrated that *AtGLR3.3* regulates $[Ca^{2+}]_{cyt/nuc}$ transients of phloem cells triggered by exogenously administered 1mM L-Glu. Notably, ER Ca^{2+} dynamics measurements in a series of different *AtGLR3.3*-regulated responses suggested that *AtGLR3.3* activity is unlikely to occur at the level of the ER, in which instead it was reported to localize (Nguyen et al., 2018)

The causative link between the systemic *AtGLR3.3* activation and the accumulation of glutamate in the apoplast was assessed by mutating specific *At*GLR3.3-LBD residues to impair its ability to accommodate the L-Glu. Exploiting the structural data of the recently released crystal structure of the *At*GLR3.3-LBD (Alfieri et al., 2020), we identify two key residues required for the binding of the ligand. Thus, transgenic lines expressing *At*GLR3.3 variants harbouring mutations in the LBD were generated (i.e., $GLR3.3_{R550N}$ and $GLR3.3_{D543G}$). Here we give the first genetic demonstration *in planta* that the *At*GLR3.3 is activated by the binding of its LBD to L-Glu and possibly to other AAs in both local and systemic responses. In fact, (i) the L-Glu induced $[Ca^{2+}]_{cyt}$ increase in root tip cells, an event known to be dependent on the *At*GLR3.3 activity (Qi et al., 2006; Sthephens et al., 2008; Alfieri et al., 2020), was strongly impaired and completely abolished in the GLR3.3$_{D543G}$ and GLR$_{R550N}$, respectively and (ii) the leaf-burning induced $[Ca^{2+}]_{cyt}$ increase in flower receptacle cells was completely abolished in both the two mutated variants. Since in root tip cells the GLR3.3$_{D543G}$ is able to mediate a $[Ca^{2+}]_{cyt}$ transient in response to 2.5 mM L-Glu, the lack of any $[Ca^{2+}]_{cyt}$ response in flower receptacle cells of GLR3.3$_{D543G}$ plants suggests that in systemic tissues the amount of L-Glu that accumulate in the apoplast in response to leaf burning is lower than 2.5 mM. This conjecture is corroborated by the *in vivo* calibration of the iGluSnFR L-Glu sensor used to monitor the $[L\text{-}Glu]_{apo}$ dynamics which suggested that in flower receptacle cells µM concentrations of L-Glu accumulates in the apoplast before the genesis of the burning-induced Ca^{2+} response. This is indeed a concentration more in accordance with the *At*GLR3.3-LBD binding affinity for L-Glu measured *in vitro* which is in the low µM range (Alfieri et al., 2020), compared instead to what was reported by Toyota and colleagues that claimed that concentrations up to 100 mM of L-Glu would be required to induce a systemic GLR dependent signalization (Toyota et al., 2018).

Delivery of a low amount of L-Glu (111.61 ± 1.09 pmol/min) at the level of the primary vein of a leaf was able to induce a local $[Ca^{2+}]_{cyt/nuc}$ transient, but not any $[Ca^{2+}]_{cyt/nuc}$ in systemic tissues. Thus, it is unlikely that the sole L-Glu that possibly activates GLRs at the site of wounding is sufficient to initiate propagating VPs and Ca^{2+} waves in systemic tissues. Importantly, an important property of VPs is their ability to propagate beyond dead parts of the plant (Vodeneev et al., 2015). Thus, since the electrical activity is based on the action of ion channels in viable cells, it is plausible that systemic VPs originate from another primary signal that is not of electric nature.

We observed that leaf-burning induces the bending of the primary inflorescence towards the treated leaf. The stem-bending anticipated both the $[Ca^{2+}]_{cyt/nuc}$ and $[L\text{-}Glu]_{apo}$ increases and was found to be independent of the *At*GLR3.3 activity.

In plants, the primary force driving rapid movements is a change in hydrostatic pressure (Mano and Masabe, 2021). Several reports showed that in various plant species burning is able to induce increases in xylem pressure (Malone et al., 1991; Boari et al., 1993; Stahlberg et al., 1996; Stankovic et al., 1997). We thus investigated whether a change in the hydraulic pressure could be responsible for the increase of $[L\text{-}Glu]_{apo}$ in systemic tissues. Employing a novel perfusion-based protocol to assess the effect of root treatment in the rosette of adult *Arabidopsis* plants grown in hydroponics, we demonstrated that hypo-osmotic stress, which regains cell turgor, induce the apoplastic accumulation of L-Glu and a subsequent $[Ca^{2+}]_{cyt/nuc}$, where the systemic Ca^{2+} increase is dependent on the activity of *At*GLR3.3.

Taking all pieces of evidence together, we propose a model in which a mechanical damage (wounding and burning) triggers propagating hydraulic waves that induce the accumulation of µM amounts of L-Glu (and possibly other AAs) in the apoplast of systemic tissues by yet unidentified mechanism. The accumulation of L-Glu in the apoplast activates in turn GLRs Ca^{2+}-permeable channels through the binding to their LBD, a step that is required for the generation of the systemic $[Ca^{2+}]_{cyt}$ increase. *De facto*, it is possible that VPs and Ca^{2+} waves are not propagating signals *per se*, but rather L-Glu-activated GLRs-dependent local responses that are induced in systemic tissues by the propagation of a primary signal of another nature, plausibly a hydraulic signal. In this scenario, L-Glu could be considered, together with other possible factors, one of the components of the long-sought Ricca's factor, a transported wound substance of unknown nature that was postulated to initiate electrical signals in systemic tissues (Ricca, 1916; Malone, 1992; Vodeneev et al., 2012) (**Fig. 16**)

The proposed model would predict the presence of *At*GLR3.3 on the plasma membrane, where it can bind with its LBD the L-Glu accumulated in the apoplast. However, no *At*GLR3.3 subcellular localization data were presented in this work, even if several reports show the presence of *At*GLR3.3 activity in the plasma membrane of several cell types (ref, Mou et al., 2020). Nonetheless, in some works *At*GLR3.3 was reported to be localized at the endomembranes and not at the plasma membrane (Wudick et al., 2018; Nguyen et al., 2018) but data in pollen demonstrated that the *At*GLR3.3 is subjected to a complex trafficking regulation (Wudick et al., 2018) and it is possible that only a low amount of protein can reach the plasma membrane, possibly to an amount difficult to be detected with a fluorescent tag. To shed light on this critical point, immunogold labelling with specific GLR antibodies should be pursued.

Last but not least, although this work is focused mainly on the *At*GLR3.3 isoform, it is well known that other GLRs isoforms are involved in the propagation of wounding-induced electrical signals and Ca^{2+} waves propagation. In particular, *glr3.1/glr3.3* and *glr3.3/glr3.6* double mutants showed no electrical signals in systemic leaves upon wounding (Mousavi et al., 2013; Nguyen et al., 2018). The possibility that *At*GLR3.1 and *At*GLR3.6 could form a heteromeric channel in phloem with *At*GLR3.3 is excluded since both *At*GLR3.1 and *At*GLR3.6 are expressed in xylem contact cells meanwhile the *At*GLR3.3 is expressed in phloem cells (sieve tubes and companion cells). In this scenario, is the binding to the LBD of both *At*GLR3.1 and *At*GLR3.6 required to adjuvate the *At*GLR3.3 in the long-distance signalling? Or is it possible that *At*GLR3.1 and *At*GLR3.6 are only involved in the local propagation of an electrical signal that must be initiated by the L-Glu-induced *At*GLR3.3-activation? Thanks to the recent publications of *At*GLRs structural data (Alfieri et al., 2020; Gangwar et al., 2020; Green et al., 2021), the generation of transgenic lines expressing *At*GLR3.1 and *At*GLR3.6 variants mutated in their LBDs, coupled to measurements of electrical potentials and Ca^{2+} dynamics, will help to shed light on these interrogatives.

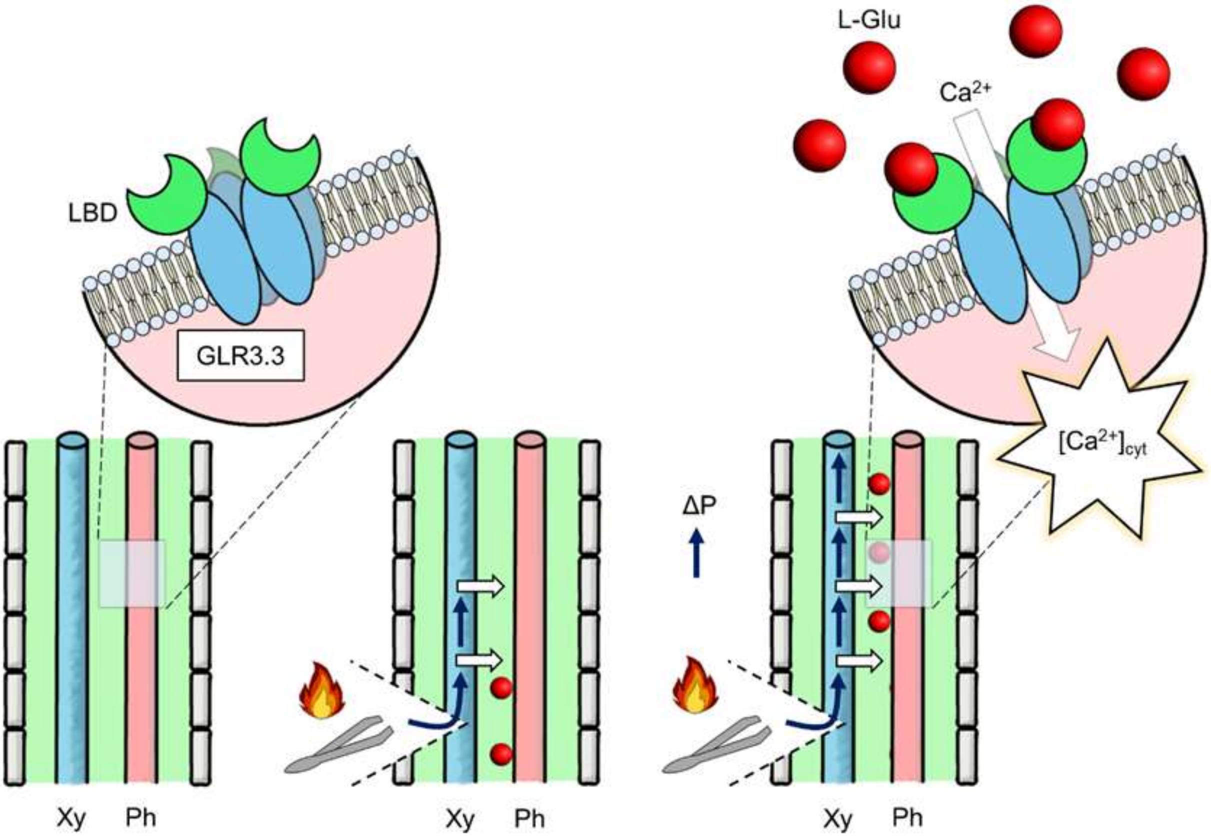

Figure 16. Model for *At*GLR3.3 activation in systemic tissues upon mechanical stress. The *At*GLR3.3 LBD is facing the apoplast in phloem tissues. Wounding or burning of one rosette leaf causes a change in tension and pressure in xylem (Xy) and phloem (Ph) cells[6,12] that consequently induces the increase of L-Glu in the apoplastic space in a µM range of concentration. The GLR3.3 LBD binds apoplastic L-Glu which, by gating the channel, triggers the downstream increase of $[Ca^{2+}]_{cyt}$.

Chapter IV. Materials and methods

IV.1. Plant material and growth conditions

Arabidopsis thaliana plants were of the ecotype Columbia 0 (Col-0). Seeds were surface-sterilized by vapour-phase sterilization (5 h exposition to fumes produced by the reaction of 100 mL of commercial (v/v) sodium hypochlorite with 3 mL 37% (v/v) hydrochloric acid). Sterilized seeds were plated in sterile conditions by means of a toothpick on half-strength Murashige and Skoog medium (MS) (Murashige and Skoog, 1962) (Duchefa, http://www.duchefa-biochemie.com/) supplemented with 0.1% (w/v) sucrose, 0.05% MES monohydrate, pH 5.8, and solidified with 0.8% (w/v) plant agar (Duchefa, http://www.duchefa-biochemie.com/). Plated seeds were stratified at 4°C for 3 days, keeping the plates horizontally. At the end of the stratification period, seeds were transferred to the growth chamber under long-day conditions (16 h light/8 h dark cycles, 100 µE m^{-2} s^{-1} of Cool White Neon lamps) at 22°C. For imaging experiments in seedlings, plants were grown in plates kept vertically and imaged 6-7 days after germination (DAG). For imaging experiments in adult plants, 14 DAG plants were transferred in soil under long-day conditions (16 h light/8 h dark cycles, 100 µE m^{-2} s^{-1} of Cool White Neon lamps) at 22°C and 75% relative humidity, and imaged after 5-7 week of growth at the bolting stage.

Nicotiana benthamiana plants were cultivated in a greenhouse under long-day conditions (16 h light/8 h dark cycles) at 22/18°C and 60% atmospheric humidity. Five-six week-old plants were used for agroinfiltration experiments.

Imaging experiment in adult plants were carried out with plants grown in soil or in hydroponic conditions. For hydroponic cultures, the samples were prepared as follows: (i) tip boxes were filled with the hydroponic growth solution prepared as described in van Wilder et al., 2008 (van Wilder et al., 2008) (1.5 mM $Ca(NO_3)_2 \times 4H_2O$, 1.5 mM KNO_3, 1.5 mM $Mg(SO_4) \times 7H_2O$, 1.5 mM KH_2PO_4, 1.5 mM $(NH_4)_2SO_4$, 0.1 mM $C_{10}H_{12}FeN_2NaO_8$, 0.15 mM $Na_2O_3Si \times 9H_2O$, 0.05 mM KCl, 0.01 mM $MnSO_4 \times H_2O$, 0.0015 mM $CuSO_4 \times 5H_2O$, 0.002 mM $ZnSO_4 \times 7H_2O$, 0.05 mM H_3BO_3, 75 nM $(NH_4)_6Mo_7O_{24}$); (ii) Seed-holders (Araponics, https://www.araponics.com/) were filled with rock wool and placed in the pipette tip rack located in the tip box filled with the hydroponic solution, making sure that the rock wool was well soaked with the solution; (iii) seeds were placed on the rock wool and stratified at 4°C for 3 days; (iv) boxes with seeds were transferred to the growth chamber under long-day conditions (16 h light/8 h dark cycles, 100 µE m^{-2} s^{-1} of Cool White Neon lamps) at 22°C and 75% relative humidity and imaged after 3 weeks of growth.

IV.2. Bacterial strains

For plasmid cloning, amplification and purification the DH5α competent *Escherichia coli* strain was used. Plant transformation was carried out using the GV3101/pMP90 *Agrobacterium tumefaciens* strain.

IV.3. Molecular cloning and plasmid constructs – pGreen0029 pSUC2::YC3.6

The coding sequence (CDS) of the Cameleon YC3.6 harbouring HindIII and EcoRI restriction sites (Nagai et al., 2004) at its 5'- and 3'-termini, respectively, was digested with HindIII/EcoRI (NEB, https://international.neb.com/) from the original *pcDNA3-YC3.6* plasmid (Nagai et al., 2004). The digested *YC3.6* CDS was ligated with the T4 DNA Ligase (NEB, https://international.neb.com/) into a modified *pGreen0029-Ter* binary vector (Ter = 19S CaMV terminator sequence) (Hellens et al., 2000) previously digested with HindIII/EcoRI (NEB, https://international.neb.com/) to generate the *pGreen0029-YC3.6-Ter*. The promoter sequence of the *SUCROSE-PROTON SYMPORTER 2* (*pSUC2*) (Truernit and Sauer, 1995) was amplified by PCR from the genomic DNA of *Arabidopsis* by means of the proofreading Phusion High-Fidelity DNA Polymerase (NEB, https://international.neb.com/). AC591 (Forward) and AC592 (Reverse) primers (**Supplementary Table 2**) used for the *pSUC2* amplification were designed to insert KpnI and HindIII sites at 5'- and 3'-termini of the *pSUC2* sequence, respectively. The obtained *pSUC2* amplicon was digested with KpnI and HindIII (NEB, https://international.neb.com/) and ligated into the *pGreen0029-YC3.6-Ter* previously digested with the same enzymes. The obtained vector was sequenced to verify the absence of mistakes.

IV.4. Molecular cloning and plasmid constructs – pB7WG2.0 p35S::GLR3.3-EGFP

For GLR3.3-eGFP subcellular localization analysis in *Nicotiana benthamiana* leaf epidermal cells, the wild type *AtGLR3.3* CDS with the silent mutations introduced by Wudick et al. (Wudick et al., 2018) was used. A Gateway™ LR Clonase™ reaction (https://www.thermofisher.com/) was employed to swap the *AtGLR3.3* cDNA from a *pDONR201-GLR3.3* vector (kindly provided by Prof. Josè Feijo, University of Maryland, USA) to the destination binary vector *pB7FWG2.0 p35S::eGFP* (kindly provided by Prof. Paolo Pesaresi, University of Milan, Italy). Site-directed mutagenesis was commissioned to Vector Builder (https://en.vectorbuilder.com/). Mutations were introduced into the *pB7FWG2.0 p35S::GLR3.3-eGFP* (GLR3.3$_{R550N}$ and GLR3.3$_{D543G}$) with the mutagenesis primers listed in **Supplementary Table 2**. All obtained vectors were sequenced to verify the absence of mistakes.

IV.5. Molecular cloning and plasmid constructs – pGreen0179 pGLR3.3::gGLR3.3

To generate the constructs for the complementation of the *glr3.3-1* and *glr3.3-2* genetic backgrounds, the *At*GLR3.3 full-length genomic sequence was cloned in the *pGreen0179* binary vector (Hellens et al., 2000). First, the *AtGLR3.3* promoter sequence (*pGLR3.3*) (1180 base pairs (bp)) was amplified by PCR from the genomic DNA of *Arabidopsis* using the proofreading Phusion High-Fidelity DNA Polymerase (NEB, https://international.neb.com/). AC564 (Forward) and AC566 (Reverse) primers (**Supplementary Table 2**) used for the *pGLR3.3* amplification were designed to insert KpnI and NotI restriction sites and 5'- and 3'-termini of the *pGLR3.3* sequence, respectively. The obtained *pGLR3.3* amplicon was digested with KpnI and NotI (NEB, https://international.neb.com/) and ligated with the pGreen0179 binary vector previously digested with the same enzymes. Second, the *AtGLR3.3* genomic sequence (*gGLR3.3*) was amplified by PCR from the genomic DNA of *Arabidopsis* using the proofreading Phusion High-Fidelity DNA Polymerase (NEB, https://international.neb.com/). AC357 (Forward) and AC549 (Reverse) primers were designed to insert a KpnI site at both 5'- and 3'-termini of the *gGLR3.3* sequence. The obtained *gGLR3.3* amplicon was digested with KpnI and ligated with the *pGreen0179-pGLR3.3* construct previously digested with the same enzyme and dephosphorylated with the Antarctic Phosphatase (NEB, https://international.neb.com/) to prevent self-ligation. Site-directed mutations introduced into the *pGreen0179-pGLR3.3::gGLR3.3* (GLR3.3$_{R550N}$ and GLR3.3$_{D543G}$) were commissioned to Vector Builder (https://en.vectorbuilder.com/). Primers used for site-directed mutagenesis are listed in **Supplementary Table 2**. All obtained vectors were sequenced to verify the absence of mistakes.

IV.6. Transformation of plasmid DNA into DH5α competent E. coli cells

The freeze-thaw method was used to introduce constructs of interest into DH5α competent *E. coli* cells. 100 ng of plasmid DNA was added to 50 µL of DH5α *E. coli* cells that were subsequently incubated in ice for 30 min. At the end of the incubation in ice, heat shock was induced by incubating the cells in a water bath at 42°C for 45 sec and then chilling them immediately at 0°C for at least 2 min. 500 µL of Luria-Bertani (LB) (1% (w/v) Bacto-Tryptone, 5% (w/v) Bacto-Yeast extract, 5% (w/v) NaCl) growth medium (SIGMA-ALDRICH, http://sigmaaldrich.com/) was added to the cells that were left at 37°C for 1 h to recover. Transformed cells were then plated on LB growth medium solidified with 2% (w/v) agar added with the appropriate selective antibiotic, and incubated overnight at 37°C.

IV.7. Plasmid DNA extraction

Colonies of DH5α competent *E. coli* cells grown on the selective solid LB medium were inoculated in 3 mL liquid LB growth medium containing the appropriate selective antibiotic at 37 °C overnight, under a continuous and gentle shacking (150 rpm). The plasmid DNA was isolated and purified from the grown bacterial cultures with the Monarch Plasmid Miniprep Kit (NEB, https://international.neb.com/) which employs the alkaline lysis method.

IV.8. Agrobacterium tumefaciens transformation

Agrobacterium tumefaciens is a widely used plant pathogen characterized by the ability to transfer foreign genes into a wide variety of host plants. In particular, *A. tumefaciens* is able to transfer a portion (T-DNA) of the tumour-inducing (Ti) plasmid in the plant host's nuclear genome, an ability that has been exploited in plant genetic engineering. Constructs of interest were introduced in *A. tumefaciens* GV3101/pMP90 strain by the freeze-thaw method. 1 µg of plasmid DNA was added to 100 µL of GV3101/pMP90 competent *A. tumefaciens* cells that were subsequently frozen in liquid nitrogen. Then, cells were incubated in a water bath at 37°C for 5 min. 1 mL of Yeast Extract Peptone (YEP) medium (1% (w/v) Bacto-Tryptone, 1% (w/v) Yeast-Extract, 5% (w/v) NaCl, pH 7.0) was added to the cells that were left to recover at 28°C for 2 h, under a gentle shaking (50 rpm). Cells were pelleted at 2000 x g for 2 min and the supernatant was discarded. 0.1 mL of YEP medium was added to the pellet, and cells were plated on LB growth medium solidified with 2% (w/v) agar added with the appropriate selective antibiotics and incubated at 28°C for 2-3 days.

IV.9. Transient Expression in Nicotiana benthamiana leaves

Nicotiana benthamiana leaf infiltration was performed using *Agrobacterium tumefaciens GV3101/pMP90* strain carrying the specified constructs (*p35S::GLR3.3*$_{wt}$*-eGFP*, *p35S::GLR3.3*$_{R550N}$*-eGFP*, and *p35S::GLR3.3*$_{D543G}$*-eGFP*) together with the p19-enhanced expression system according to the method described by Waadt and Kudla (Waadt and Kudla, 2008). For the confocal imaging analysis, the plants were kept for 3–5 days after the infiltration under incubation conditions described above.

IV.10. Transgenic plants

The *pGreen0029-pSUC2::YC3.6* and *pGreen0179-pGLR3-3::gGLR3.3*$_{wt}$, *pGreen0179-pGLR3-3::gGLR3.3*$_{R550N}$, *pGreen0179-pGLR3-3::gGLR3.3*$_{D543G}$, constructs were introduced into the *Agrobacterium tumefaciens* GV3101/pMP90 strain. *A. tumefaciens* cultures were incubated overnight in 250 mL YEP medium with selective antibiotics. Grown cultures were pelleted at 7000 x g at 10°C for 15 min. The supernatant was discarded, and the pellet was suspended in a 500 mL solution containing 5% (w/v) sucrose and 0.05 (v/v) Silwett L-77, a surfactant that enhances bacteria penetration into plant tissues. To generate the *pSUC::YC3.6* transgenic lines, *Arabidopsis thaliana* Col-0 wild type, *glr3.3-1* knockout allele at the flowering stage (Qi et al., 2006) were dipped into a suspension cell culture of *A. tumefaciens* (Floral-dip; Clough and Bent, 1998) harbouring the *pGreen0029-pSUC2::YC3.6*. To generate the *pGLR3.3-gGLR3.3* wt and mutated complemented lines, *Arabidopsis thaliana* Col-0 *glr3.3-1* and *glr3.3-2* knockout alleles at the flowering stage (Qi et al., 2006) expressing the NES-YC3.6 (NES = Nuclear export signal) were dipped into a suspension cell culture of *A. tumefaciens* harbouring the *pGreen0179-pGLR3.3::gGLR3.3*$_{wt}$, or the *pGreen0179-pGLR3.3::gGLR3.3*$_{R550N}$, or the *pGreen0179-pGLR3.3::gGLR3.3*$_{D543G}$. Transgenic *pSUC::YC3.6* lines were selected by means of a fluorescent stereo microscope (using the GFP filter) for the presence of the Cameleon YC3.6 fluorescence. Transgenic *glr3.3-1* and *glr3.3-2* lines complemented with the *pGLR3.3::gGLR3.3*$_{wt}$, *pGLR3.3::gGLR3.3*$_{R550N}$, and *pGLR3.3::gGLR3.3*$_{D543G}$ were selected on ½ MS solid medium supplemented with 25 mg/L hygromycin.

The *Arabidopsis thaliana* double sensor line for the simultaneous analysis of $[\text{L-Glu}]_{apo}$ and $[Ca^{2+}]_{cyt/nuc}$ was generated by crossing *pUB10::R-GECO1* (Keinath et al., 2015) and *p35S::CHIB-iGluSnFR* (CHIB = basic chitinase signal peptide of 63 bp to localize the sensor in the apoplast) (Toyota et al., 2018) *Arabidopsis* plants. To generate the *glr3.3-1* T-DNA line expressing both the iGluSnFR and R-GECO1 sensors, the obtained *iGluSnFR x R-GECO1* double sensor line was crossed with the *glr3.3-1* T-DNA line and plants homozygous for the T-DNA insertion into the *AtGLR3.3* gene were isolated by carrying out a phenotypic selections based on the impaired Glu-induced $[Ca^{2+}]_{cyt/nuc}$ response. The selected putative mutants were then genotyped to detect the presence of T-DNA insertion in both copies of the *GLR3.3* allele (homozygous) (see below § IV.12). Primers used to the *glr3.3-1* genotyping are listed in **Supplementary Table 2**.

IV.11. Genomic DNA extraction from plant tissues

Genomic DNA used for the plant genotyping or amplification of genomic sequences was extracted from young leaves. Leaves were detached from the plant and rapidly transferred into 2 mL Eppendorf tubes in the presence of 500 µL freshly prepared extraction buffer (100 mM Tris pH 8.5, 50 mM EDTA, 500 mM NaCl) at 4°C. Leaves were shredded mechanically with a plastic pestle. 35 µL of 20% (w/v) sodium dodecyl sulphate (SDS) were added in order to solubilize proteins and lipids, and samples were incubated at 65°C for 5 min. After the addition of 130 µL 5 M potassium acetate (KOAc) to decrease the mixture alkalinity, samples were kept at 0°C for 5 min and then centrifuged at 10000 x g for 10 min. The supernatant was transferred into 1.5 mL Eppendorf tubes and both 640 µL isopropyl alcohol and 60 µL 3 M sodium acetate (NaOAc) were added, which make the DNA insoluble allowing its precipitation. Samples were kept at -20°C for 1h. Samples were centrifuged at 15000 x g for 10 min and the supernatant was discarded. Pellets were washed with 300 µL 70% (v/v) ethanol (EtOH) to eliminate salts and SDS residues and enhance the DNA precipitation after a successive centrifugation step (5 min, 15000 x g). The supernatant was discarded, and the pellets were left to dry out under a chemical hood for 30 min to allow the complete ethanol evaporation which presence would inhibit subsequent enzymatic reactions. Pellets were later re-suspended in 40µl bi-distilled H_2O and heated at 65°C for 10 min. Samples were centrifuged at 15000 x g for 5 min and the supernatant containing the DNA was conserved at -20°C.

IV.12. Genotyping of Arabidopsis thaliana insertion mutant alleles

To assess the T-DNA homozygosity in the *glr3.3-1* and *glr3.3-2* T-DNA lines, genomic DNA extracted from the different plants was subjected to two different PCR reactions, one that amplifies the region of the *AtGLR3.3* gene where the T-DNA is located in the insertion lines, and the other one that assures the presence of the T-DNA into the *AtGLR3.3* gene. Two couples of primers were employed: (i) AC400 (Forward) and AC401 (Reverse) annealed on *AtGLR3.3* and report the presence of an intact copy of the gene; (ii) AC441 (Forward) and AC401 annealed on the T-DNA and *AtGLR3.3*, respectively, and report the presence of the presence of the T-DNA into the *AtGLR3.3* sequence. The same PCR reactions were performed on *glr3.3-1* and *glr3.3-2* T-DNA lines expressing the NES-YC3.6 complemented with the *At*GLR3.3 wild type or mutated variants, to both verify the insertion of the T-DNA into the *AtGLR3.3* gene and the presence of at least one copy of the reintroduced *AtGLR3.3* genomic sequence. To verify the presence of the mutated variants of *AtGLR3.3* generated by site-directed mutagenesis (§ x.x) used to complement the *glr3.3-1* and *glr3.3-2* T-DNA alleles a a different strategy based on RT-PCR analysis was designed. First, complementary strands of DNA (cDNAs) were produced by retro transcription of total RNA extracted from 6-day-old seedlings of the differentet complemented lines. The obtained cDNAs were used as a template in PCR reactions with AC387 and AC401 primers designed to amplify a portion of the AtGLR3.3 ligand binding sequence (the region were the point mutations were introduced) straddling the mutated region. The obtained amplicons were sequenced to confirm the presence of the mutations. Primer sequences are listed in **Supplementary Table 2**. All the PCR reactions to assess the presence of the T-DNA and the presence of the *AtGLR3.3* gene were performed using the GoTaq™ DNA Polymerase (Promega Corporation, https://Promega.com/). The PCR reactions to amplify the portion of the sequence coding for the LBD from cDNAs were performed with the proofreading Phusion High-Fidelity DNA Polymerase (NEB, https://international.neb.com/).

IV.13. PCR conditions

PCR Go-Taq® standard protocol: <10 ng/25 µl DNA, 0.5 µl 10 mM dNTPs mix, 5 µl 5X Green Go-Taq Reaction Buffer (Promega Corporation, https://Promega.com/), 0.1 µl 5U/µl Go-Taq® G2 DNA Polymerase (Promega Corporation, https://Promega.com/), 0.5µl 10µM forward and reverse primers, bi-distilled H_2O to a final volume of 25µl.

PCR Phusion® standard protocol: <10 ng DNA, 10µl 5X Phusion® HF Reaction Buffer (NEB, https://international.neb.com/), 1 µl dNTPs 10 mM mix, 1.5 µl 10 µM forward (F) and reverse (R) primers, 1µl 2U/µl Phusion-HF® DNA polymerase (NEB, https://international.neb.com/), 1.5µl 100% DMSO (NEB, https://international.neb.com/), bi-distilled H_2O to a final volume of 50µl.

IV.14. RNA extraction and quantitative qRT-PCR analysis

To assess the expression level of the Jasmonate-inducible *AtJAZ10* (AT5G13220) gene, total RNA was extracted from the primary inflorescence of 5-week-old plants at 0, 15, 30 and 60 min after the burning of one fully expanded rosette leaf. To assess the expression level of *AtGLR3.3* in the different genetic backgrounds at the developmental stages used to perform the experiments, total RNA was extracted from both the primary inflorescence of 5-week-old plants and 6-day-old seedlings. The extraction of total RNA was carried out through the LiCl-based methodology described in “Verwoerd et al., 1989”. To remove gDNA contamination from RNA samples, extracted RNAs were treated with DNase I (NEB, https://international.neb.com/). 0.5 µg of total RNA was reverse transcribed using the ImProm-II Reverse Transcriptase System (Promega Corporation, https://Promega.com/). The obtained cDNA was used to assess the expression of the gene of interest by means of quantitative Reverse Transcription PCR (qRT-PCR). qRT-PCR was performed in technical triplicates with SYBR Green detection (iTaq Universal SYBR Green Supermix, Bio-Rad Laboratories, https://bio-rad.com/) using the CFX 96 Real-Time System (Bio-Rad Laboratories, https://bio-rad.com/). The primers used were AC629 and AC630 for *JAZ10,* AC402 and AC403 for *GLR3.3. AtJAZ10* and *AtGLR3.3* cDNA level was standardized relative to TUBULIN (AT5G44340) (AC348 and AC349 primers for *TUB*) transcript levels and gene expression analysis was performed with the 2^−ΔΔCt method using Bio-Rad CFX Maestro software v.4.0 (Bio-Rad Laboratories, https://bio-rad.com/). Values are representative averages from three biological samples. Specific primers are listed in **Supplementary Table 2.**

IV.15. GUS staining

The β-Glucuronidase (GUS) is a bacterial enzyme that catalyses the hydrolysis of colourless β-Glucoronide residues generating coloured products (blue). The histochemical staining of GUS activity in transgenic plants harbouring the GUS gene under the control of the promoter of a gene of interest enables to detect in which cells, tissues, and organs such gene is expressed (transcriptional reporter). Moreover, chimeric protein in which the sequence of a gene of interest is fused to the GUS gene allows to identify in which cells, tissues, and organs the protein of interest localizes (translational reporter). The inflorescence of the *pGLR3.3::GLR3.3-GUS* (translational reporter), and the *pGLR3.6::GUS* and *pJAZ10::GUS* (transcriptional reporters) were collected and tissues were prefixed in 90% acetone at -20°C for 1 h. The tissues were washed 3 times for 5 min with 50 mM phosphate buffer (pH 7.0). Samples were incubated in the GUS staining solution (2 mM X-Gluc, 0.1 % Triton X-100 (v/v), 2 mM C6FeK4N6, 2 mM C6N6FeK3, 50 mM phosphate buffer pH 7.0, 10 mM EDTA) and subjected to a vacuum step for 20 min to facilitate the penetration of the GUS staining solution into the tissues. At the end of the vacuum step, samples were incubated at 37°C for 16 h. Tissues were cleared in 70% ethanol, then mounted in 20% glycerol and observed.

IV.16. Preparation of transverse sections

Transverse sections of the primary *Arabidopsis* inflorescence stem were produced using a vibratome (Speed= 0.9 mm/s, Amplitude = 1.25 mm, Feed rate = 50 µm) on a portion of the stem previously embedded in 6% (w/v) agarose. Sections were collected in a Petri dish containing 50 mM phosphate buffer. *pGLR3.3::GLR3.3-GUS* and *pGLR3.6::GUS* sections were imaged with a bright field microscope. *pSUC::YC3.6* sections were imaged with a confocal microscope.

IV.17. Confocal laser scanning microscopy

Confocal microscopy analyses of stable transgenic *Arabidopsis* plants and *Nicotiana benthamiana* leaves were performed using a Nikon Eclipse Ti2 inverted microscope, equipped with a Nikon A1R+ laser scanning device (http://www.nikon.com/). For localization studies, images were acquired by a CFI Plan Apo Lambda 4X (Numerical Aperture (N.A.) 0.2), a CFI Apo Lambda 40XC LWD WI (N.A. 1.15) and CFI Plan Apo Lambda 60X Oil (N.A. 1.4). Cameleon YC3.6 and GFP were excited with the 488-nm laser and the emission was collected at 505–550 nm. Chlorophyll was excited with the 488-nm laser and the emission was collected at 663–738 nm. NIS-Elements (Nikon; http://www.nis-elements.com/) was used as a platform to control the microscope. Images were analyzed using FIJI software (https://fiji.sc/).

IV.18. Wide-field fluorescence microscopy

For wide-field apoplastic L-Glu and Ca^{2+} imaging analyses in seedling root tip cells of iGluSnFR and Cameleon lines, an inverted fluorescence Nikon microscope (Ti-E; http://www.nikon.com/) with a CFI Plan Apo VC 20X (N.A. 0.75) was used. For imaging of mature primary inflorescence of Cameleon lines images were acquired by a CFI Plan Apo Lambda 4X (N.A. 0.2). Excitation light was produced by a fluorescent lamp (Prior Lumen 200 PRO; Prior Scientific; http://www.prior.com/) with 488 nm (470/40 nm) for both the iGluSnFR and ER-GCaMP6-210 sensors, and 440 nm (436/20 nm) for the Cameleon YC3.6. The lamp was set at 20% at 20X magnification or 100% with the 4X magnification. iGluSnFR and ER-GCaMP6-210 fluorescence emission was collected at 505–530 nm. For the analysis of the Cameleon YC3.6 lines, the FRET CFP/YFP optical block A11400-03 (emission 1, 483/32 nm for ECFP; emission 2, 542/27 nm for FRET/cpVenus) with a dichroic 510 nm mirror

(Hamamatsu) was used. Images were collected with a Hamamatsu Dual CCD camera (ORCA-D2; http://www.hamamatsu.com/). Camera binning was set to 2 x 2 for the iGluSnFR, ER-GCaMP6-210, and YC3.6 seedlings with exposure times from 100 to 150 ms and 4 x 4 in YC3.6 inflorescence with exposure times from 250 to 500 ms depending on the line analyzed. Images were acquired every 5 s. Filters and dichroic mirrors were purchased from Chroma Technology (http://www.chroma.com/). NIS-Elements (Nikon; http://www.nis-elements.com/) was used as a platform to control the microscope, illuminator, and camera. Images were analyzed using FIJI software (https://fiji.sc/).

IV.19. Spinning Disk Confocal Microscopy

Confocal spinning disk microscopy analyses of root-tip cells and receptacle flower cells were performed using a Nikon Eclipse Ti2 inverted microscope, equipped with a Yokogawa Spinning Disk Confocal System (https://www.microscope.healthcare.nikon.com/en_EU/products/confocal-microscopes/csu-series/specifications/). The oil immersion CFI Plan Apo Lambda 60X Oil (N.A. 1.4) and the CFI Plan Apo VC 20X (N.A. 0.75) were used as objectives. iGluSnFR and ER-GCaMP6-210 were excited by a 488-nm single-mode optical fibre laser and the emission was collected at 525–550 nm. R-GECO1 was excited by a 561-nm single-mode optical fibre laser and the emission was collected at 576–626 nm. Images were collected with a Photometrics Prime BSI CMOS camera (https://www.photometrics.com/products/prime-family/primebsi/) with an exposure time from 200 to 300 ms with a 2 x 2 binning (1024 x 1024 pixels) for each emission. The NIS-Element AR (Nikon, Japan, http://www.nis-elements.com/) was used as a platform to control the microscope, laser, camera, and post-acquisition analyses.

IV.20. Stereomicroscopy of wound-, burn- and hypoosmotic stress-induced Ca^{2+} and L-Glu increase in adult plants

Wounding experiments were performed on 3-week-old *Arabidopsis iGluSnFR x R-GECO1* plants and on 3-week-old *Arabidopsis ER-GCaMP6-210 x R-GECO1* plants. Wounding was carried out after 3 min from the start of the experiment by crushing a fully expanded leaf with a forceps, being careful to damage the primary vein. Images were acquired with a Nikon stereomicroscope (SMZ18, http://www.nikon.com/) equipped with a 5.9-megapixel CMOS DS-Fi3 Microscope Camera. Excitation light was produced by a mercury light source (Intensilight; http://www.nikon.com/) with GFP and RFP filter Cubes. A Plan Apo 0.5X objective was used without zoom for the imaging of the entire plant and images were collected with an exposure time of 1 sec with a 2 x 2 camera binning (1440 x 1024 pixels) for each emission. iGluSnFR and R-GECO1 images were acquired every 5 sec by an automatized switching between the GFP and RFP configuration. The same protocol was used to acquire ER-GCaMP6-210 and R-GECO1 images.

Leaf burning experiments were performed on 4-week-old *Arabidopsis GCaMP3* plants. Leaf burning was carried out by means of a lighter after 2 min from the start of the experiment flaming a fully expanded leaf. Images were acquired with the same setup used in wounding experiments, employing the GFP filter cube only. Images were collected with an exposure time of 1 sec in continuum with a 2 x 2 camera binning (1440 x 1024 pixels)

Hypoosmotic stress experiments were performed on 3-week-old *Arabidopsis iGluSnFR x R-GECO1* plants grown in hydroponics. Plants were incubated in hydroponic solution containing 500 mM D-Sorb for 4 h and then imaged. Plants were places in custom chambers produced with a 3D-printer with a capacity of 15 mL. D-Sorb was washout with a perfusion system (10 mL/min) after 3 min from the start of the experiment, which allowed the complete washout of the solution in less than 2 minutes. Images were acquired with the same setup used in wounding experiments. iGluSnFR and R-GECO1 images were acquired every 5 sec by an automatized switching between the GFP and RFP configuration.

IV.21. Image analysis

All the acquired images were analyzed using FIJI software (https://fiji.sc/). For each sensor, the respective emission intensity has been quantified as mean of the signal intensity of each pixel in a Region Of Interest (ROI) (indicated in the figures). The signal intensity mean was subtracted from the background signal, which was calculated as mean signal of pixels in a ROI drawn outside the sample. All the data were processed with Excel software (https://www.microsoft.com/). For iGluSnFR, R-GECO, GCaMP3, ER-GCaMP6-210 analysis, the signal intensity mean, subtracted from the background, was normalized in respect to the fluorescence intensity value representative of the pre-stimulus condition (F_0) and presented as $\Delta F/F_0$ ($\Delta F = F_t – F_0$, where F_t is the fluorescence intensity value at a specific time point). For Cameleon analysis, the ratio (R) between the YFP (cpVenus) and CFP fluorescence emissions intensities subtracted from the background was calculated. The raw cpVenus/CFP ratio was normalized in respect to the ratio value representative of the pre-stimulus condition (R_0) and presented as $\Delta R/R_0$ ($\Delta R = R_t – R_0$, where R_t is the ratio value at a specific time point).

IV.22. Measurements of the burning-induced bending of the stem of the primary inflorescence

Adult plants of wild type, *glr3.3* mutants and *glr3.3* complemented lines were imaged with the camera of a smartphone. A fully expanded leaf was burned with a lighter and the entity of the movement was quantified in the x-axis direction (the axis perpendicular to the primary inflorescence stem) using graph paper as a reference.

IV.23. Kymograph

Kymograph **Fig. 14m** was generated using Fiji (multiple kymograph plugin). The kymograph was used to depict the temporal evolution of the iGluSnFR emission changes in the primary inflorescence stem after the burning of one rosette leaf.

IV.24. Seedling imaging

Root imaging experiments were performed on 7-day-old seedlings. Seedling were removed from the plate (see ***Plant material and growth conditions***) and mounted on an imaging chamber. Samples were overlaid with cotton wool soaked in imaging solution (5 mM KCl, 10 mM MES, 10 mM $CaCl_2$ pH 5.8 adjusted with Tris-base). Under continuous perfusion (0.9 mL/min), 5 min were awaited before the start of the experiment to allow the plant to recover from the stress caused by the transfer into the imaging chamber. After 2 min from the start of the experiment, seedlings were perfused with the imaging solution supplemented with L-Glu or D-Glu for 3 min (pulsed treatment). Solution with L-Glu or D-Glu was then wash away perfusing the imaging solution until the end of the experiment.

IV.25. Imaging in longitudinal stem sections

For imaging experiments on sections from the primary inflorescence stem, a portion of the stem was cut transversely with a bistury. The cut part was mounted on an imaging chamber and was overlaid with cotton wool soaked in imaging solution (5 mM KCl, 10 mM MES, 10 mM $CaCl_2$ pH 5.8 adjusted with Tris-base). Under continuous perfusion (0.9 mL/min), 25 min were awaited before the start of the experiment to allow the plant to recover from the stress caused by the invasive procedure. After 2 min from the start of the experiment, stem sections were perfused with the imaging solution supplemented with L-Glu for 3 min (pulsed treatment). Solution with L-Glu was then wash away perfusing the imaging solution until the end of the experiment.

IV.26. Organic Electronic Ion Pump fabrication and characterization (Performed by Eleni Stavrinidou's lab)

Capillary based Organic Electronic Ion Pumps (c-OEIPs) were fabricated according to Seitanidou et al. (2019). Briefly, 4 glass capillary fibres (40 cm long) with inner and outer diameters of 25 and 150 µm, respectively (TSP025150 Fused Silica Capillary, CM Scientific) were flushed with 2 M KOH for 2 h at a pressure of 2 bar to etch the inner surface. The capillaries were then flushed with deionized water for 10 min and dried upon nitrogen for 10 min. To provide covalent bonding of the polymer to the glass capillary surface, vinylic groups are added to the surface through flushing 3-(trimethoxysilyl)propylmethacrylate (10% (w/v) in toluene) for 1 h. The inner surface was then washed with ethanol for 20 min and dried with nitrogen for 10 min. As the last step, we flushed the polyelectrolyte solution consisting of the monomer [2-(acryloyloxy) ethyl]trimethylammonium chloride (AETMAC), Sigma-Aldrich, MW 2000, 35% (w/v)) mixed with polyethylene glycol diacrylate (MW 6000 2 wt%), deionized water and two photoinitiators (0.5% (w/v) 2-hydroxy-4′-(2-hydroxyethoxy)-2-methylpropiophenone, and Lithium phenyl-2,4,6- Trimethylbenzoylphosphinate, Sigma-Aldrich). The capillaries were then irradiated with UV light (Osram Dulux L Blue 18W/71 UVB) for 1 h to promote crosslinking. The fibres were then cut into 10 mm pieces and assembled with shrink tubes, acting as reservoirs. The assembled OEIP were stored in 0.2 M NaCl solution, in order to keep the polycationic membrane hydrated. c-OEIP L-Glu and D-Glu delivery efficiency was evaluated with mass spectrometry. The c-OEIP source reservoir was filled with 50 mM L-Glu or D-glu (Sigma-Aldrich) solutions. Taking into account that the c-OEIP channel is charge-selective (i.e., all negatively charged ions from the source solution can be delivered), the pH of the source solution was adjusted to 7 using 1 M NaOH, providing a high Glu^-/OH^- ratio. The device was operated in constant current mode with a source meter unit (Keithley 2602). The current was applied between the source and the target, using (poly(3,4-ethylenedioxythiophene):polystyrene sulfonate) PEDOT:PSS electrodes. A constant current of 150 nA was applied for 1 h, delivering L-Glu in a target solution (deionized water), and then Mass Spectrometry analysis was carried out (see the section for details) for quantification.

IV.27. L- and D-Glu UHPLC-MS/MS analysis (Performed by Eleni Stavrinidou's lab)

The analysis and quantification of the L- and D-Glutamate (L-Glu, D-Glu) was carried out as follows. Samples containing 500 µl of deionized water with L- or D-Glu, always individually, were diluted 100x and 100 µl were transferred into insert-equipped vial. 20 µl was subsequently injected into UHPLC-ESI-MS/MS system, consisting of a 1290 Infinity Binary LC System coupled to a 6490 Triple Quad LC/MS System with Jet Stream and Dual Ion Funnel technologies (Agilent Technologies, Santa Clara, CA, USA). The mobile phase composition was A: 10 mM ammonium formate, pH 2.6; B: 100% MeOH. Stationary phase: Atlantis Premier BEH C18 AX Column, 1.7 µm, 2.1 x 100 mm (Waters Inc., Milford, MA, USA). Elution was isocratic A:B, 98:2, flow rate 0.250 ml/min, column temperature 40°C, total run time was 3 min. Targeted compound was eluted in 1.19 min. The targeted compounds have a mass of 148 $[M+H]^+$ and produce a fragment with the mass of 84 $[M+H]^+$. Hence, the MRM transition of 148 > 84 was used for confirmation and quantification. A calibration curve was prepared by injecting L-or D-Glu stock solutions in the range of 10^{-9} M – 10^{-4} M, 10 µl, (0.01 pmol – 1000 pmol on column). Log function of the peak area to Log function of the calibration point concentrations was used to create a linear regression with the equation of $y = 0.9392x + 5.0892$ and correlation coefficient R2 = 0.998. The peak area, its log value, extracted from each of the samples was used in this equation to calculate the concentration of targeted compounds in the diluted samples.

IV.28. In planta glutamate delivery with the c-OEIP (Performed in collaboration with Eleni Stavrinidou's lab)

The c-OEIP was inserted closed to the main vein of *Arabidopsis thaliana* leaf with the help of a micromanipulator. A PEDOT:PSS electrode was placed in the source electrolyte, while an Ag/AgCl electrode (Redox.me) was placed in the soil as a reference electrode. The c-OEIP was operated at a constant current of 150 nA using a source meter unit (Agilent b2912a), for 30 min. Wound control experiments were performed with dry c-OEIP on other plants (**Fig. 13c-g**).

IV.29. Statistical analysis

All the data are representative of $n \geq 3$ experiments. Reported traces are averages of traces from all single experiments used for the statistical analyses. Results are reported as averages ± standard deviations (SD). *P*-values were calculated with a two-sided Student's *t*-test. Statistical significance was also validated using one-way analysis of variance and with post hoc Tukey Honestly Significant. Data from experiments with at least $n = 5$ were plotted as box-and-whisker plots using GraphPad, in which all the experimental points are plotted, and their distribution represented as a box that extends from the 25th to 75th percentiles. The line in the middle of the box is plotted at the median

Chapter V. Supplementary materials

Supplementary Table 1. List of *AtGLR* genes that are expressed in the residuum (REC) and secession (SEC) cells of the flower abscission zone (from Lee et al., (2018)).

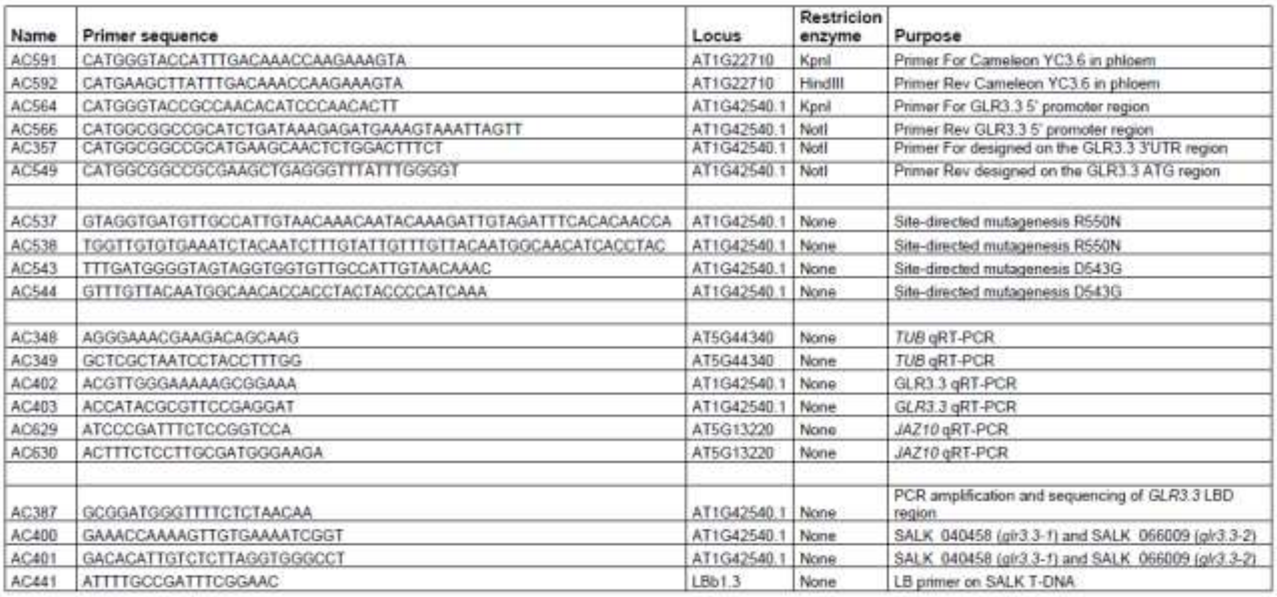

Name	Primer sequence	Locus	Restricion enzyme	Purpose
AC591	CATGGGTACCATTTGACAAACCAAGAAAGTA	AT1G22710	KpnI	Primer For Cameleon YC3.6 in phloem
AC592	CATGAAGCTTATTTGACAAACCAAGAAAGTA	AT1G22710	HindIII	Primer Rev Cameleon YC3.6 in phloem
AC564	CATGGGTACCGCCAACACATCCCAACACTT	AT1G42540.1	KpnI	Primer For GLR3.3 5' promoter region
AC566	CATGGCGGCCGCATCTGATAAAGAGATGAAAGTAAATTAGTT	AT1G42540.1	NotI	Primer Rev GLR3.3 5' promoter region
AC357	CATGGCGGCCGCATGAAGCAACTCTGGACTTTCT	AT1G42540.1	NotI	Primer For designed on the GLR3.3 3'UTR region
AC549	CATGGCGGCCGCGAAGCTGAGGGTTTATTTGGGGT	AT1G42540.1	NotI	Primer Rev designed on the GLR3.3 ATG region
AC537	GTAGGTGATGTTGCCATTGTAACAAACAATACAAAGATTGTAGATTTCACACAACCA	AT1G42540.1	None	Site-directed mutagenesis R550N
AC538	TGGTTGTGTGAAATCTACAATCTTTGTATTGTTTGTTACAATGGCAACATCACCTAC	AT1G42540.1	None	Site-directed mutagenesis R550N
AC543	TTTGATGGGGTAGTAGGTGGTGTTGCCATTGTAACAAAC	AT1G42540.1	None	Site-directed mutagenesis D543G
AC544	GTTTGTTACAATGGCAACACCACCTACTACCCCATCAAA	AT1G42540.1	None	Site-directed mutagenesis D543G
AC348	AGGGAAACGAAGACAGCAAG	AT5G44340	None	*TUB* qRT-PCR
AC349	GCTCGCTAATCCTACCTTTGG	AT5G44340	None	*TUB* qRT-PCR
AC402	ACGTTGGGAAAAAGCGGAAA	AT1G42540.1	None	GLR3.3 qRT-PCR
AC403	ACCATACGCGTTCCGAGGAT	AT1G42540.1	None	*GLR3.3* qRT-PCR
AC629	ATCCCGATTTCTCCGGTCCA	AT5G13220	None	*JAZ10* qRT-PCR
AC630	ACTTTCTCCTTGCGATGGGAAGA	AT5G13220	None	*JAZ10* qRT-PCR
AC387	GCGGATGGGTTTTCTCTAACAA	AT1G42540.1	None	PCR amplification and sequencing of *GLR3.3* LBD region
AC400	GAAACCAAAAGTTGTGAAAATCGGT	AT1G42540.1	None	SALK_040458 (*glr3.3-1*) and SALK_066009 (*glr3.3-2*)
AC401	GACACATTGTCTCTTAGGTGGGCCT	AT1G42540.1	None	SALK_040458 (*glr3.3-1*) and SALK_066009 (*glr3.3-2*)
AC441	ATTTTGCCGATTTCGGAAC	LBb1.3	None	LB primer on SALK T-DNA

Supplementary Table 2 List of primers.

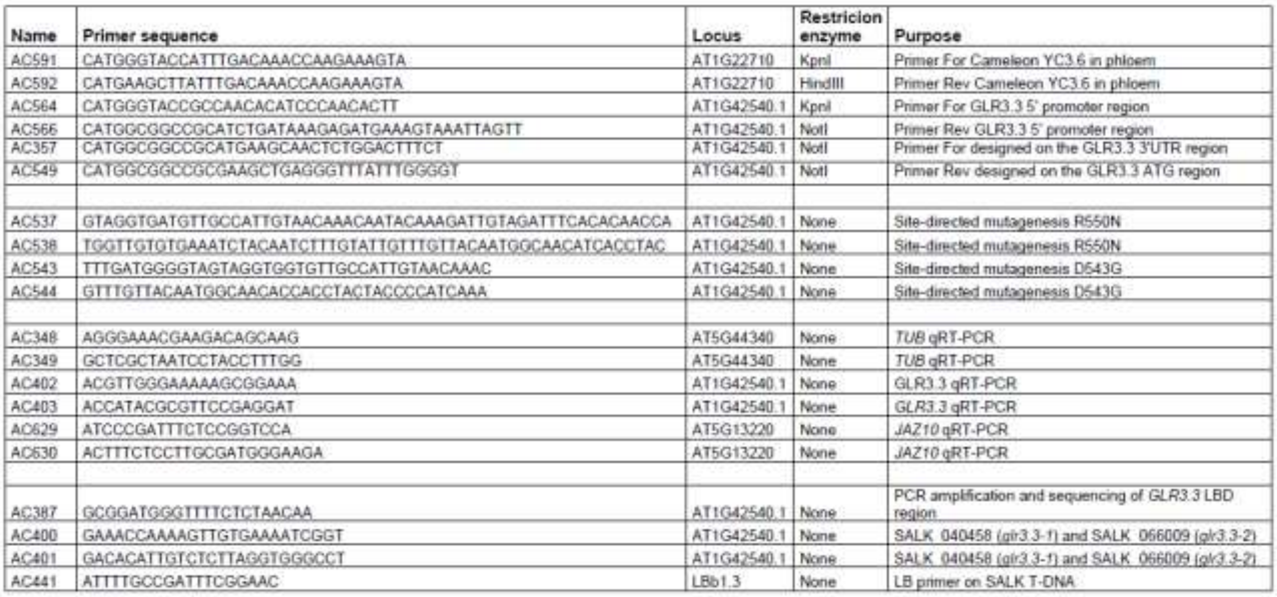

Name	Primer sequence	Locus	Restricion enzyme	Purpose
AC591	CATGGGTACCATTTGACAAACCAAGAAAGTA	AT1G22710	KpnI	Primer For Cameleon YC3.6 in phloem
AC592	CATGAAGCTTATTTGACAAACCAAGAAAGTA	AT1G22710	HindIII	Primer Rev Cameleon YC3.6 in phloem
AC564	CATGGGTACCGCCAACACATCCCAACACTT	AT1G42540.1	KpnI	Primer For GLR3.3 5' promoter region
AC566	CATGGCGGCCGCATCTGATAAAGAGATGAAAGTAAATTAGTT	AT1G42540.1	NotI	Primer Rev GLR3.3 5' promoter region
AC357	CATGGCGGCCGCATGAAGCAACTCTGGACTTTCT	AT1G42540.1	NotI	Primer For designed on the GLR3.3 3'UTR region
AC549	CATGGCGGCCGCGAAGCTGAGGGTTTATTTGGGGT	AT1G42540.1	NotI	Primer Rev designed on the GLR3.3 ATG region
AC537	GTAGGTGATGTTGCCATTGTAACAAACAATACAAAGATTGTAGATTTCACACAACCA	AT1G42540.1	None	Site-directed mutagenesis R550N
AC538	TGGTTGTGTGAAATCTACAATCTTTGTATTGTTTGTTACAATGGCAACATCACCTAC	AT1G42540.1	None	Site-directed mutagenesis R550N
AC543	TTTGATGGGGTAGTAGGTGGTGTTGCCATTGTAACAAAC	AT1G42540.1	None	Site-directed mutagenesis D543G
AC544	GTTTGTTACAATGGCAACACCACCTACTACCCCATCAAA	AT1G42540.1	None	Site-directed mutagenesis D543G
AC348	AGGGAAACGAAGACAGCAAG	AT5G44340	None	*TUB* qRT-PCR
AC349	GCTCGCTAATCCTACCTTTGG	AT5G44340	None	*TUB* qRT-PCR
AC402	ACGTTGGGAAAAAGCGGAAA	AT1G42540.1	None	GLR3.3 qRT-PCR
AC403	ACCATACGCGTTCCGAGGAT	AT1G42540.1	None	*GLR3.3* qRT-PCR
AC629	ATCCCGATTTCTCCGGTCCA	AT5G13220	None	*JAZ10* qRT-PCR
AC630	ACTTTCTCCTTGCGATGGGAAGA	AT5G13220	None	*JAZ10* qRT-PCR
AC387	GCGGATGGGTTTTCTCTAACAA	AT1G42540.1	None	PCR amplification and sequencing of *GLR3.3* LBD region
AC400	GAAACCAAAAGTTGTGAAAATCGGT	AT1G42540.1	None	SALK_040458 (*glr3.3-1*) and SALK_066009 (*glr3.3-2*)
AC401	GACACATTGTCTCTTAGGTGGGCCT	AT1G42540.1	None	SALK_040458 (*glr3.3-1*) and SALK_066009 (*glr3.3-2*)
AC441	ATTTTGCCGATTTCGGAAC	LBb1.3	None	LB primer on SALK T-DNA

Chapter VI. References

Alfieri *et al.* (2020) ‘The structural bases for agonist diversity in an *Arabidopsis thaliana* glutamate receptor-like channel’, *Proc Natl Acad Sci U S A,* 117(1):752-760. doi: 10.1073/pnas.1905142117.

Basu and Haswell (2021) ‘The Mechanosensitive Ion Channel MSL10 Potentiates Responses to Cell Swelling in Arabidopsis Seedlings’, *Curr Biol.*, 20;30(14):2716-2728.e6. doi: 10.1016/j.cub.2020.05.015. Epub 2020 Jun 11.

Behera et al. (2018) ‘Cellular Ca^{2+} Signals Generate Defined pH Signatures in Plants’, *The Plant Cell*, Volume 30, Issue 11, Pages 2704–2719. doi: https://doi.org/10.1105/tpc.18.00655.

Bernacka-Wojcik *et al.* (2018) ‘Implantable Organic Electronic Ion Pump Enables ABA Hormone Delivery for Control of Stomata in an Intact Tobacco Plant’, *Small* 2019, 15, 1902189. doi: https://doi.org/10.1002/smll.201902189.

Berridge *et al.* (2000) ‘The versatility and universality of calcium signalling’, *Nat Rev Mol Cell Biol*, 1(1):11-21. doi: 10.1038/35036035.

Blyth and Morris (2019) ‘Shear-Enhanced Dispersion of a Wound Substance as a Candidate Mechanism for Variation Potential Transmission’, *Front. Plant Sci.,* doi: https://doi.org/10.3389/fpls.2019.01393.

Boari and Malone (1993) ‘Wound-Induced Hydraulic Signals: Survey of Occurrence in a Range of Species’, *Journal of Experimental Botany*, Volume 44, Issue 4, Pages 741–746. doi: https://doi.org/10.1093/jxb/44.4.741

Bonza and De Michelis (2011) ‘The plant Ca^{2+}-ATPase repertoire: biochemical features and physiological functions’, *Plant Biology,* 421–430. doi:10.1111/j.1438-8677.2010.00405.x.

Bonza *et al.* (2013) ‘Analyses of Ca^{2+} Accumulation and Dynamics in the Endoplasmic Reticulum of *Arabidopsis* Root Cells Using a Genetically Encoded Cameleon Sensor’, *Plant Physiol.*, 163(3): 1230–1241. doi: 10.1104/pp.113.226050.

Bose *et al.* (2011) ‘Calcium efflux systems in stress signaling and adaptationin plants’, *Front Plant Sci,* 2:85 doi: 10.3389/fpls.2011.00085.

Bush and Jones (1987) ‘Measurement of cytoplasmic calcium in aleurone protoplasts using indo-1 and fura-2’, *Cell Calcium* 8(6):455-72. doi: 10.1016/0143-4160(87)90029-7.

Case *et al.* (2007) ‘Evolution of calcium homeostasis: From birth of the first cell to an omnipresent signalling system’, *Cell Calcium*, 42(4-5):345-50. doi: 10.1016/j.ceca.2007.05.001.

Charpentier *et al.* (2016) ‘Nuclear-localized cyclic nucleotide-gated channels mediate symbiotic calcium oscillations’, *Science*, 352(6289):1102-5. doi: 10.1126/science.aae0109.

Chen *et al.* (1999) ‘Functional characterization of a potassium-selective prokaryotic glutamate receptor’, *Nature,* 402(6763):817-21. doi: 10.1038/45568.

Chen *et al*. (2016) ‘Evolutionary and Expression Analysis Provides Evidence for the Plant Glutamate-like Receptors Family is Involved in Woody Growth-related Function’, *Scientific Reports*, volume 6, Article number: 32013 (2016). doi: https://doi.org/10.1038/srep32013.

Chiu *et al.* (2002) ‘Phylogenetic and expression analysis of the glutamate-receptor-like gene family in *Arabidopsis thaliana*’, *Mol Biol Evol*., 19(7):1066-82. doi: 10.1093/oxfordjournals.molbev.a004165

Christmann *et al*. (2013) ‘Hydraulic signals in long-distance signaling’, *Curr Opin Plant Biol* 16(3):293-300. doi: 10.1016/j.pbi.2013.02.011.

Coe and Michalak (2009) ‘Calcium binding chaperones of the endoplasmic reticulum’, *Gen Physiol Biophys*, Spec No Focus: F96-F103. doi:10.1042/BJ20081847.

Conn *et al.* (2011) ‘Cell-Specific Vacuolar Calcium Storage Mediated by CAX1 Regulates Apoplastic Calcium Concentration, Gas Exchange,and Plant Productivity in *Arabidopsis*’, *The Plant Cell*, Vol. 23: 240–257. doi: 10.1105/tpc.109.072769.

Corso *et al.* (2018) ‘Endoplasmic reticulum-localized CCX2 is required for osmotolerance by regulating ER and cytosolic Ca^{2+} dynamics in *Arabidopsis*’, *Proc Natl Acad Sci U S A,* 115 (15) 3966-3971. doi: https://doi.org/10.1073/pnas.1720422115.

Costa *et al.* (2018) ‘The contribution of organelles to plant intracellular Calcium signalling’, *J Exp Bot,* doi: 10.1093/jxb/ery185.

De Bortoli *et al.* (2016) ‘Evolutionary insight into the ionotropic glutamate receptor superfamily of photosynthetic organisms’, *Biophys Chem*., 218:14-26. doi: 10.1016/j.bpc.2016.07.004. Epub 2016 Aug 2.

De Falco *et al.* (2010) ‘Breaking the code: Ca^{2+} sensors in plant signalling’, *Biochem. J.,* 425, 27–40 doi:10.1042/BJ20091147

Demidchik et al. (2002) ‘Nonselective cation channels in plants’, *Annu Rev Plant Biol,* 53:67-107. doi: 10.1146/annurev.arplant.53.091901.161540.

Demidchik *et al.* (2004) ‘Glutamate activates cation currents in the plasma membrane of *Arabidopsis* root cells’, *Planta*, 219(1):167-75. doi: 10.1007/s00425-004-1207-8. Epub 2004 Feb 7.

Demidchik *et al.* (2018) ‘Calcium transport across plant membranes: mechanisms and functions’, *New Phytologist*, 220:49–69 doi: 10.1111/nph.15266.

Dennison and Spalding (2000) ‘Glutamate-Gated Calcium Fluxes in *Arabidopsis*’, *Plant Physiology*, Volume 124, Issue 4, Pages 1511–1514, doi: https://doi.org/10.1104/pp.124.4.1511.

Dingledine *et al.* (1999) ‘The glutamate receptor ion channels’, *Pharmacol Rev.*, 51(1):7-61. PMID: 10049997.

Dodd *et al.* (2010) ‘The language of calcium signaling’, *Annu Rev Plant Biol*, 61:593-620. doi: 10.1146/annurev-arplant-070109-104628.

Dziubinska *et al.* (1989) ‘The effect of excitation on the rate of respiration in the liverwort *Conocephalum conicum*’, *Physiologia Plantarum*, doi: https://doi.org/10.1111/j.1399-3054.1989.tb04648.x

Edel *et al.* (2017) ‘The Evolution of Calcium-Based Signalling in Plants’, *Curr Biol.*, 27(13):R667-R679. doi: 10.1016/j.cub.2017.05.020.

Edwards (2021) ‘Periplasmic-binding protein-based biosensors and bioanalytical assay platforms: Advances, considerations, and strategies for optimal utility’, *Talanta Open 3*. doi: https://doi.org/10.1016/j.talo.2021.100038.

Etherton and Rubinstein (1978) ‘Evidence for Amino Acid-H^+ Co-Transport in Oat Coleoptiles’, *Plant Physiology*, Volume 61, Issue 6, Pages 933–937, doi: https://doi.org/10.1104/pp.61.6.933.

Farmer *et al.* (2014) ‘The squeeze cell hypothesis for the activation of jasmonate synthesis in response to wounding’, *New Phytologist*, 204: 282–288. doi: 10.1111/nph.12897

Farmer *et al.* (2020) ‘Wound- and mechanostimulated electrical signals control hormone responses’, *New Phytologist,* 227:1037–1050doi: 10.1111/nph.16646.

Fleet *et al.* (1998) ‘Calcium Buffering Capacity of Neuronal Cell Cytosol Measured by Flash Photolysis of Calcium Buffer NP-EGTA’, *Biochem Biophys Res Commun*, 250(3):786-90. doi: 10.1006/bbrc.1998.9377.

From and Lautner (2006) ‘Electrical signals and their physiological significance in plants’, *Plant, Cell and Environment,* 249–257 doi: 10.1111/j.1365-3040.2006.01614.x.

Gangwar *et al.* (2020) ‘Structure of the Arabidopsis Glutamate Receptor-like Channel GLR3.2 Ligand-Binding Domain’, *Structure,* 29(2):161-169.e4. doi: 10.1016/j.str.2020.09.006. Epub 2020 Oct 6

Gasperini *et al.* (2015) ‘Axial and Radial Oxylipin Transport’, *Plant Physiology*, Volume 169, Issue 3, Pages 2244–2254. doi: https://doi.org/10.1104/pp.15.01104

Gibeaut *et al.* (1997) ‘Maximal Biomass of Arabidopsis thaliana Using a Simple, Low-Maintenance Hydroponic Method and Favorable Environmental Conditions’, *Plant Physiology*, Volume 115, Issue 2, Pages 317–319, doi: https://doi.org/10.1104/pp.115.2.317

Gilroy *et al.* (1991) ‘Role of Calcium in Signal Transduction of Commelina Guard Cells’, *Plant Cell,* 3(4):333-344. doi: 10.1105/tpc.3.4.333.

Gilroy *et al*. (2016) ‘ROS, Calcium, and Electric Signals: Key Mediators of Rapid Systemic Signaling in Plants’, *Plant Physiology*, Volume 171, Issue 3, Pages 1606–1615. doi: https://doi.org/10.1104/pp.16.00434.

Green *et al.* (2021) **‘**Structure of the *Arabidopsis thaliana* glutamate receptor-like channel GLR3.4’, *Mol Cell.,* 81(15):3216-3226.e8. doi: 10.1016/j.molcel.2021.05.025. Epub 2021 Jun 22.

Grenzi *et al.* (2021a) ‘Illuminating the hidden world of calcium ions in plants with a universe of indicators’, *Plant Physiology*, Volume 187, Issue 2, Pages 550–571, doi: https://doi.org/10.1093/plphys/kiab339

Grenzi *et al.* (2021b) ‘Structural insights into long-distance signal transduction pathways mediated by plant glutamate receptor-like channels’, *New Phytologist*, 229:1261–1267. doi: 10.1111/nph.17034

Hadzic *et al*. (2017) ‘Ionotropic glutamate receptors: Which ones, when, and where in the mammalian neocortex’, *J Comp Neurol.,* 1;525(4):976-1033. doi: 10.1002/cne.24103.

He et al., (2021) ‘Transport, functions, and interaction of calcium and manganese in plant organellar compartments’, *Plant Physiol.,* 187(4):1940-1972. doi: 10.1093/plphys/kiab122.

Hedrich *et al.* (2016) ‘Electrical Wiring and Long-Distance Plant Communication’, *Trends Plant Sci* 21(5):376-387. doi: 10.1016/j.tplants.2016.01.016.

Herde et al. (1999) ‘Electric Signaling and *Pin2* Gene Expression on Different Abiotic Stimuli Depend on a Distinct Threshold Level of Endogenous Abscisic Acid in Several Abscisic Acid-Deficient Tomato Mutants’, *Plant Physiol.,* 119(1): 213–218. doi: 10.1104/pp.119.1.213.

Iosip et al. (2020) ‘The Venus flytrap trigger hair–specific potassium channel KDM1 can reestablish the K^+ gradient required for hapto-electric signaling’, *PLOS Biology*. doi: https://doi.org/10.1371/journal.pbio.3000964

Ishka *et al*. (2021) ‘*Arabidopsis* Ca^{2+}-ATPases 1, 2, and 7 in the endoplasmic reticulum contribute to growth and pollen fitness’, *Plant Physiol.* 185(4): 1966–1985. doi: 10.1093/plphys/kiab021.

Iwano *et al.* (2009) 'Fine-Tuning of the Cytoplasmic Ca*2*+ Concentration Is Essential for Pollen Tube Growth', *Plant Physiology*, Volume 150, Issue 3, Pages 1322–1334. doi: https://doi.org/10.1104/pp.109.139329.

Jaiswal (2001) 'Calcium - how and why?', *J Biosci*, 26(3):357-63. doi: 10.1007/BF02703745.

Keinath *et al.* (2015) 'Live Cell Imaging with R-GECO1 Sheds Light on flg22- and Chitin-Induced Transient [Ca(2+)]cyt Patterns in Arabidopsis', *Mol Plant,* 8(8):1188-200. doi: 10.1016/j.molp.2015.05.006. Epub 2015 May 19.

Kelner *et al.* (2018) 'Dual color sensors for simultaneous analysis of calcium signal dynamics in the nuclear and cytoplasmic compartments of plant cells', *Frontiers in Plant Science* 9, 245. doi: https://doi.org/10.3389/fpls.2018.00245.

Klusener and Weiler (1999) 'A Calcium-Selective Channel from Root-Tip Endomembranes of Garden Cress', *Plant Physiology*, Volume 119, Issue 4, Pages 1399–1406. doi: https://doi.org/10.1104/pp.119.4.1399.

Knight *et al.* (1991) 'Transgenic plant aequorin reports the effects of touch and cold-shock and elicitors on cytoplasmic calcium', *Nature*, 524–526. doi: https://doi.org/10.1038/352524a0

Kong et al. (2016) 'L-Met Activates *Arabidopsis* GLR Ca $^{2+}$ Channels Upstream of ROS Production and Regulates Stomatal Movement', *Cell Rep.,* 17(10):2553-2561. doi: 10.1016/j.celrep.2016.11.015.

Krebs *et al.* (2012) 'FRET-based genetically encoded sensors allow high-resolution live cell imaging of Ca^{2+} dynamics', *The Plant Journal*, 9, 181–192. doi: 10.1111/j.1365-313X.2011.04780.x

Kudla *et al.* (2018) 'Advances and current challenges in calcium signaling', *New Phytologist*, 218:414–431 doi: 10.1111/nph.14966

Lacombe *et al.* (2001) 'The identity of plant glutamate receptors', *Science,* 292(5521):1486-7. doi: 10.1126/science.292.5521.1486b.

Lam *et al.* (1998) 'Glutamate-receptor genes in plants', *Nature*, 12;396(6707):125-6 doi: 10.1038/24066.

Lautner *et al*. (2005) 'Characteristics of Electrical Signals in Poplar and Responses in Photosynthesis', *Plant Physiology*, Volume 138, Issue 4, Pages 2200–2209, doi: https://doi.org/10.1104/pp.105.064196.

Lecorieux *et al.* (2006) 'Calcium in plant defence-signalling pathways', *New Phytologist,* 171: 249–269. doi: https://doi.org/10.1111/j.1469-8137.2006.01777.x

Lee and Michalak (2012) ‘Calcium and bioenergetics: from endoplasmic reticulum to mitochondria’, *Animal Cells and Systems*, Pages 269-273. doi: https://doi.org/10.1080/19768354.2012.685181.

Lee *et al.* (2018) ‘A Lignin Molecular Brace Controls Precision Processing of Cell Walls Critical for Surface Integrity in Arabidopsis’, *Cell*, 173, 1468–1480, May 31. doi: https://doi.org/10.1016/j.cell.2018.03.060

Leitão *et al.* (2019) ‘Nuclear calcium signatures are associated with root development’, *Nat Commun*, 10, 4865 (2019). doi: https://doi.org/10.1038/s41467-019-12845-8.

Li *et al.* (2021) ‘Plant electrical signals: A multidisciplinary challenge’, *J Plant Physiol*., 261:153418. doi: 10.1016/j.jplph.2021.153418.

Loro *et al.* (2016) ‘Chloroplast-specific in vivo Ca^{2+} imaging using yellow cameleon fluorescent protein sensors reveals organelle-autonomous Ca^{2+} signatures in the stroma’ *Plant Physiology*, 171, 2317–2330. doi: https://doi.org/10.1104/pp.16.00652.

MacKinnon (2003) ‘Potassium channels’, *FEBS Lett*., 555(1):62-5. doi: 10.1016/s0014-5793(03)01104-9.

Madden (2002) ‘The structure and function of glutamate receptor ion channels’, *Nat Rev Neurosci*., 3(2):91-101. doi: 10.1038/nrn725.

Malone (1992) ‘Kinetics of wound-induced hydraulic signals and variation potentials in wheat seedlings’, *Planta*, 187, 505–510. doi: https://doi.org/10.1007/BF00199969.

Malone and Stankovic (1991) ‘Surface potentials and hydraulic signals in wheat leaves following localized wounding by heat’, *Plant, Cell and Environment*, doi: https://doi.org/10.1111/j.1365-3040.1991.tb00953.x.

Mano and Hasabe (2021) ‘Rapid movements in plants’, J Plant Res.,134(1):3-17. doi: 10.1007/s10265-020-01243-7. Epub 2021 Jan 7.

Marvin *et al.* (2013) ‘An optimized fluorescent probe for visualizing glutamate neurotransmission’, *Nat Methods*, 10, 162–170. doi: https://doi.org/10.1038/nmeth.2333

Marvin *et al.* (2018) ‘Stability, affinity, and chromatic variants of the glutamate sensor iGluSnFR’, *Nat Methods*, 15, 936–939 (2018). https://doi.org/10.1038/s41592-018-0171-3.

McAinsh and Hetheringtom (1998) ‘Encoding specificity in Ca2+ signalling systems’, *Trends in Plant Science*, Volume 3, Issue 1, Pages 32-36

McAinsh *et al.* (1990) ‘Abscisic acid-induced elevation of guard cell cytosolic Ca^{2+} precedes stomatal closure’, *Nature***,** 186–188 (1990). doi: https://doi.org/10.1038/343186a0.

Minguet-Parramona *et al.* (2015) ‘An Optimal Frequency in Ca^{2+} Oscillations for Stomatal Closure Is an Emergent Property of Ion Transport in Guard Cells’, *Plant Physiology*, Volume 170, Issue 1, Pages 33–42. doi: https://doi.org/10.1104/pp.15.01607.

Mithofer and Mazar (2002) ‘Aequorin-based measurements of intracellular Ca^{2+}-signatures in plant cells’, *Biol Proced Online,* 4:105-118. doi: 10.1251/bpo40.

Miyawaki *et al.* (1997) ‘Fluorescent indicators for Ca^{2+}based on green fluorescent proteins and calmodulin’, *Nature*, 882–887. doi: https://doi.org/10.1038/42264

Moe-Lange *et al.* (2021) ‘Interdependence of a mechanosensitive anion channel and glutamate receptors in distal wound signaling’, *Sci Adv.,* 7(37):eabg4298. doi: 10.1126/sciadv.abg4298. Epub 2021 Sep 8.

Monshausen (2012) ‘*Visualizing Ca(2+) signatures in plants’*, *Curr Opin Plant Biol*, 15(6):677-82. doi: 10.1016/j.pbi.2012.09.014.

Moosavi and Ghassabian (2017) ‘Linearity of Calibration Curves for Analytical Methods: A Review of Criteria for Assessment of Method Reliability’, *Calibration and Validation of Analytical Methods - A Sampling of Current Approaches.* doi: 10.5772/intechopen.72932.

Mou *et al.* (2020) ‘Ethylene-independent signaling by the ethylene precursor ACC in *Arabidopsis* ovular pollen tube attraction’, *Nat Commun*., 4082. doi: https://doi.org/10.1038/s41467-020-17819-9

Mousavi *et al.* (2013) ‘*GLUTAMATE RECEPTOR-LIKE* genes mediate leaf-to-leaf wound signalling’, *Nature*, 422–426 (2013). doi: https://doi.org/10.1038/nature12478.

Muir and Sanders (1997) ‘Inositol 1,4,5-Trisphosphate-Sensitive Ca^{2+} Release across Nonvacuolar Membranes in Cauliflower’, *Plant Physiology*, Volume 114, Issue 4, Pages 1511–1521, doi: https://doi.org/10.1104/pp.114.4.1511.

Nagai *et al.* (2004) ‘Expanded dynamic range of fluorescent indicators for Ca(2+) by circularly permuted yellow fluorescent proteins’, Proc Natl Acad Sci U S A ;101(29):10554-9. doi: 10.1073/pnas.0400417101.

Navazio *et al.* (2000) ‘Calcium release from the endoplasmic reticulum of higher plants elicited by the NADP metabolite nicotinic acid adenine dinucleotide phosphate’, *Proc Natl Acad Sci U S A,* 97 (15) 8693-8698*.* doi: *https://doi.org/10.1073/pnas.140217897*

Navazio et al. (2001) ‘Mobilization of Ca^{2+} by Cyclic ADP-Ribose from the Endoplasmic Reticulum of Cauliflower Florets’, *Plant Physiol.,* 125(4): 2129–2138. doi: 10.1104/pp.125.4.2129.

Nguyen *et al.* (2018) 'Identification of cell populations necessary for leaf-to-leaf electrical signaling in a wounded plant', *Proc Natl Acad Sci U S A,* 115 (40) 10178-10183 doi: https://doi.org/10.1073/pnas.1807049115

Ni *et al.* (2016) 'Heterologous Expression and Functional Analysis of Rice GLUTAMATE RECEPTOR-LIKE Family Indicates its Role in Glutamate Triggered Calcium Flux in Rice Roots', *Rice*, 9:9. Doi: 10.1186/s12284-016-0081-x

Opritov *et al.* (1991) 'Biolectrogenesis in higher plants', Nauka, Moskow

Ortiz-Ramirez *et al.* (2017) 'GLUTAMATE RECEPTOR-LIKE channels are essential for chemotaxis and reproduction in mosses', *Nature*, 549(7670):91-95. doi: 10.1038/nature23478. Epub 2017 Jul 24.

Paredes *et al.* (2008) 'Chemical calcium indicators', *Methods*, 46(3):143-51. doi: 10.1016/j.ymeth.2008.09.025. Epub 2008 Oct 16.

Perez Koldenkova and Nagai (2013) 'Genetically encoded Ca(2+) indicators: properties and evaluation', *Biochim Biophys Acta,* 1833(7):1787-97. doi: 10.1016/j.bbamcr.2013.01.011.

Prasher *et al.,* (1985) 'Cloning and expression of the cDNA coding for aequorin, a bioluminescent calcium-binding protein', *Biochemical and Biophysical Research Communications*, Volume 126, Issue 3, Pages 1259-1268. doi: https://doi.org/10.1016/0006-291X(85)90321-3

Price et al. (2012) 'Glutamate receptor homologs in plants: functions and evolutionary origins', *Front. Plant Sci.,* doi: https://doi.org/10.3389/fpls.2012.00235.

Qi et al. (2006) 'Calcium entry mediated by GLR3.3, an *Arabidopsis* glutamate receptor with a broad agonist profile', *Plant Physiol*., 142(3):963-71. doi: 10.1104/pp.106.088989. Epub 2006 Sep 29.

Resentini *et al.* (2021) 'The signatures of organellar calcium', *Plant Physiol*, 187(4):1985-2004. doi: 10.1093/plphys/kiab189.

Resentini, Grenzi *et al.* (2021) 'Simultaneous imaging of ER and cytosolic Ca^{2+} dynamics reveals long-distance ER Ca^{2+} waves in plants', *Plant Physiology*, Volume 187, Issue 2, Pages 603–617, doi: https://doi.org/10.1038/s41477-020-0667-6

Ricca (1916) 'Soluzione di un Problema di Fisiologia: la Propagazione di Stimulo nella Mimosa', Nuovo G Bot Ital 23:51-170.

Ridgway and Ashley (1967) 'Calcium transients in single muscle fibers', *Biochem Biophys Res Commun*., 29(2):229-34. doi: 10.1016/0006-291x(67)90592-x.

Salvador Recatala (2016) ‘New roles for the GLUTAMATE RECEPTOR-LIKE 3.3, 3.5, and 3.6 genes as on/off switches of wound-induced systemic electrical signals’, *Plant Signal Behav*., 11(4):e1161879. doi: 10.1080/15592324.2016.1161879.

Sanders *et al.* (1999) ‘Communicating with calcium’, *Plant Cell*, 11(4):691-706. doi: 10.1105/tpc.11.4.691.

Schmid *et al*. (2005) ‘A gene expression map of Arabidopsis thaliana development’, *Nat Genet*., 37(5):501-6. doi: 10.1038/ng1543. Epub 2005 Apr 3.

Sello *et al*. (2016) ‘Dissecting stimulus-specific Ca^{2+} signals in amyloplasts and chloroplasts of *Arabidopsis thaliana* cell suspension cultures’, *Journal of Experimental Botany* 67, 3965–3974. doi: https://doi.org/10.1093/jxb/erw038.

Shao *et al*. (2020) ‘Two glutamate- and pH-regulated Ca^{2+} channels are required for systemic wound signaling in *Arabidopsis*’, *Sci Signal.,* 13(640):eaba1453. doi: 10.1126/scisignal.aba1453.

Shimomura (2005) ‘The discovery of aequorin and green fluorescent protein’, *Journal of Microscopy*, Vol. 217, Pt 1 January 2005, pp. 3 –15. doi: https://doi.org/10.1111/j.0022-2720.2005.01441.x.

Shimomura *et al.* (1962) ‘Extraction, Purification and Properties of Aequorin, a Bioluminescent Protein from the Luminous Hydromedusan, *Aequorea*’, *J. Cell. Comp*. *Physiol.*, 59: 223-239. Doi: https://doi.org/10.1002/jcp.1030590302.

Shkolnik *et al*. (2018) ‘MIZ1 regulates ECA1 to generate a slow, long-distance phloem-transmitted Ca^{2+} signal essential for root water tracking in *Arabidopsis*’, *Proc Natl Acad Sci U S A,* 115 (31) 8031-8036. doi: https://doi.org/10.1073/pnas.1804130115.

Shroeder *et al.* (1984) ‘Potassium-selective single channels in guard cell protoplasts of *Vicia faba’, Nature*, volume 312, pages361–362. doi: https://doi.org/10.1038/312361a0.

Simon *et al.,* (2009) ‘An organic electronic ion pump to regulate intracellular signaling at high spatiotemporal resolution’, *TRANSDUCERS* 2009 - 2009 International Solid-State Sensors, Actuators and Microsystems Conference, 2009, pp. 1790-1793, doi: 10.1109/SENSOR.2009.5285721.

Singh *et al.* (2016) ‘The Arabidopsis glutamate receptor-like gene GLR3.6 controls root development by repressing the Kip-related protein gene KRP4’, *Journal of Experimental Botany*, Volume 67, Issue 6, Pages 1853–1869. doi: https://doi.org/10.1093/jxb/erv576

Stael et al. (2011) ‘Plant organellar calcium signalling: an emerging field’, *J Exp Bot*, 63(4):1525-42. doi: 10.1093/jxb/err394. Epub 2011 Dec 26.

Stahlberg and Cosgrove (1991) ‘Rapid alterations in growth rate and electrical potentials upon stem excision in pea seedlings’, *Planta*, 187(4):523-31. doi: 10.1007/BF00199972.

Stahlberg *et al.* (2006) ‘Slow Wave Potentials — a Propagating Electrical Signal Unique to Higher Plants’, *Communication in Plants*, pp 291–308. doi: https://doi.org/10.1007/978-3-540-28516-8_20.

Stankovik *et al.* (1997) ‘Characterization of the Variation Potential in Sunflower’, *Plant Physiology*, Volume 115, Issue 3, Pages 1083–1088. doi: https://doi.org/10.1104/pp.115.3.1083

Stephens *et al*. (2008) ‘Glutamate receptor subtypes evidenced by differences in desensitization and dependence on the GLR3.3 and GLR3.4 genes’, *Plant Physiol*., 146(2):529-38. doi: 10.1104/pp.107.108134. Epub 2007 Dec 27.

Swarbrek *et al.* (2013) ‘Plant Calcium-Permeable Channels’, *Plant Physiol*, Vol. 163, No. 2, pp. 514-522. doi: 10.1104/pp.113.220855

Tapken and Hollman (2008) ‘*Arabidopsis thaliana* Glutamate Receptor Ion Channel Function Demonstrated by Ion Pore Transplantation’, *J Mol Biol.,* ;383(1):36-48. doi: 10.1016/j.jmb.2008.06.076. Epub 2008 Jul 3.

Tapken *et al*. (2013) ‘A Plant Homolog of Animal Glutamate Receptors Is an Ion Channel Gated by Multiple Hydrophobic Amino Acids’, *SCIENCE SIGNALING,* Vol 6, Issue 279. doi: 10.1126/scisignal.2003762.

tat the single-cell level’, *Proc Natl Acad Sci U S A,* 97 (13) 7260-7265. doi: https://doi.org/10.1073/pnas.97.13.7260.

Teardo *et al.* (2015) ‘Alternative Splicing-Mediated Targeting of the *Arabidopsis* GLUTAMATE RECEPTOR3.5 to Mitochondria Affects Organelle Morphology’, *Plant Physiol*., 167(1): 216–227. doi: 10.1104/pp.114.242602.

Tian et al. (2009) ‘Imaging neural activity in worms, flies and mice with improved GCaMP calcium indicators’, *Nat Methods*, 6(12):875-81. doi: 10.1038/nmeth.1398. Epub 2009 Nov 8.

Tian *et al.* (2014) ‘The rice TAL effector-dependent resistance protein XA10 triggers cell death and calcium depletion in the endoplasmic reticulum’, *The Plant Cell* 26, 497–515. doi: 10.1105/tpc.113.119255.

Tian *et al.* (2020) ‘Calcium spikes, waves and oscillations in plant development and biotic interactions’, *Nature Plants*, Volume 6, 750-759. doi: https://doi.org/10.1038/s41477-020-0667-6

Toyota *et al.* (2018) ‘Glutamate triggers long-distance, calcium-based plant defense signaling’, *SCIENCE*, Vol 361, Issue 6407, pp. 1112-1115. doi: 10.1126/science.aat7744.

Traynelis *et al.* (2010) 'Glutamate receptor ion channels: structure, regulation, and function', *Pharmacol Rev.,* 62(3):405-96. doi: 10.1124/pr.109.002451.

Truernit and Sauer (1995) 'The promoter of the Arabidopsis thaliana SUC2 sucrose-H+ symporter gene directs expression of beta-glucuronidase to the phloem: evidence for phloem loading and unloading by SUC2', *Planta*, 196(3):564-70. doi: 10.1007/BF00203657.

Tsien (1980) 'New calcium indicators and buffers with high selectivity against magnesium and protons: design, synthesis, and properties of prototype structures', *Biochemistry* 1980, 19, 11, 2396–2404. doi: https://doi.org/10.1021/bi00552a018.

Vega-Munoz *et al.* (2020) 'Breaking Bad News: Dynamic Molecular Mechanisms of Wound Response in Plants', Front Plant Sci., 11:610445. doi: 10.3389/fpls.2020.610445. eCollection 2020.

Vincent et al. (2017) 'Interplay of Plasma Membrane and Vacuolar Ion Channels, Together with BAK1, Elicits Rapid Cytosolic Calcium Elevations in Arabidopsis during Aphid Feeding'*, The Plant Cell,* Volume 29, Issue 6, Pages 1460–1479. doi: https://doi.org/10.1105/tpc.17.00136.

Vincill *et al.* (2012) 'Ca(2+) conduction by an amino acid-gated ion channel related to glutamate receptors'*, Plant Physiol*., 159(1):40-6. doi: 10.1104/pp.112.197509. Epub 2012 Mar 23.

Vincill *et al.* (2013) 'Interacting Glutamate Receptor-Like Proteins in Phloem Regulate Lateral Root Initiation in Arabidopsis', *The Plant Cell*, Volume 25, Issue 4, Pages 1304–1313. doi: https://doi.org/10.1105/tpc.113.110668

Vodeneev *et al.* (2012) 'The mechanism of propagation of variation potentials in wheat leaves', *J Plant Physiol*., 1;169(10):949-54. doi: 10.1016/j.jplph.2012.02.013. Epub 2012 Apr 23

Vodeneev *et al.* (2015) 'Variation potential in higher plants: Mechanisms of generation and propagation', *Plant Signal Behav.,* 10(9): e1057365. doi: 10.1080/15592324.2015.1057365.

Wang *et al.* (2019) 'Systemic Root-Shoot Signaling Drives Jasmonate-Based Root Defense against Nematodes', Volume 29, Issue 20, 21 October 2019, Pages 3430-3438.e4. doi: https://doi.org/10.1016/j.cub.2019.08.049.

Wang, Himschoot, Grenzi *et al.* (2022) 'Auxin analog-induced Ca $^{2+}$ signaling is not involved in inhibition of endosomal aggregation in *Arabidopsis* roots', *J Exp Bot*, erac019. doi: 10.1093/jxb/erac019

Whalley and Knight (2012) 'Calcium signatures are decoded by plants to give specific gene responses' *New Phytologist*, 197:690–693 doi: https://doi.org/10.1111/nph.12087

Whalley *et al.* (2011) ‘Transcriptomic Analysis Reveals Calcium Regulation of Specific Promoter Motifs in *Arabidopsis*’, *Plant Cell*, Volume 23, Issue 11, Pages 4079-4095. doi: 10.1105/tpc.111.090480

Wudick *et al.* (2018a) ‘CORNICHON sorting and regulation of GLR channels underlie pollen tube Ca^{2+} homeostasis’, *SCIENCE,* Vol 360, Issue 6388 pp. 533-536. doi: 10.1126/science.aar6464.

Wudick *et al.* (2018b) ‘Comparing plant and animal glutamate receptors: common traits but different fates?’, *Journal of Experimental Botany*, Volume 69, Issue 17, Pages 4151–4163. doi: https://doi.org/10.1093/jxb/ery153

Xiong *et al*. (2006) ‘Calcium signaling in plant cell organelles delimited by a double membrane’, *Biochimica et Biophysica Acta*, 1763, 1209–1215. doi: 10.1016/j.bbamcr.2006.09.024.

Yu *et al.* (2021) ‘GLUTAMATE RECEPTOR-like gene *OsGLR3.4* is required for plant growth and systemic wound signaling in rice (*Oryza sativa*)’, *New Phytologist*, (2022)233:1238–1256 doi: 10.1111/nph.17859

Yuan and Zhang (2015) ‘Roles of jasmonate signalling in plant inflorescence and flower development’, *Curr Opin Plant Biol.,* 27:44-51. doi: 10.1016/j.pbi.2015.05.024.

Zhao *et al.* (2011) ‘An Expanded Palette of Genetically Encoded Ca^{2+} Indicators’, *Science,* 333(6051): 1888–1891 doi: 10.1126/science.1208592

Zimmerman *et al.* (2009) ‘System Potentials, a Novel Electrical Long-Distance Apoplastic Signal in Plants, Induced by Wounding’, *Plant Physiol*., 149(3): 1593–1600. doi: 10.1104/pp.108.133884

List of scientific publications on Journals with Impact Factor

Original scientific productions

Alfieri A, Doccula FG, Pederzoli R, **Grenzi M**, Bonza MC, Luoni L, Candeo A, Romano Armada N, Barbiroli A, Valentini G, Schneider TR, Bassi A, Bolognesi M, Nardini M, Costa A (2020) *Genetics and structure reveal Arabidopsis thaliana GLR3.3 as an amino acid receptor with a broad agonist profile.* ***PNAS*** *117: 752-760.* (contribution: imaging experiments execution and analysis)

Resentini F*, **Grenzi M***, Ancora D, Cademartori M, Luoni L, Franco M, Bassi A, Bonza MC, Costa A (2021) *Simultaneous imaging of ER and cytosolic Ca^{2+} dynamics reveals long-distance ER Ca^{2+} waves in plants.* ***Plant Physiol***. *187: 603-617* (**Joint First Author**). (contribution: experiments design, imaging experiment execution and analysis, preparation of figures and videos)

Wang R*, Himschoot E*, **Grenzi M***, Chen J, Safi A, Krebs M, Schumacher K, Nowack MK, Van Damme D, De Smet I, Geelen D, Beeckaman T, Friml J, Vanneste S (2022) Auxin analog-induced Ca^{2+} signaling is not involved in inhibition of endosomal aggregation in Arabidopsis roots. ***J Exp Bot*** Jan 27;erac019. (**Joint First Author**). (contribution: imaging experiments execution and analysis, preparation of figures).

Sato K, Saito S, Endo K, Kono M, Kakei T, Taketa H, Kato M, Hamamoto S, **Grenzi M**, Costa A, Munemasa S, Murata Y, Ishimaru Y and Uozumi N (2022) *Catechin gallate and gallocatechin gallate direct the inhibition of ABA-induced stomatal closure.* ***Adv Sci (Weinh)*** May 7;e2201403. (contribution: imaging experiments execution and analysis).

Ruberti C, Wagner S, Xu Z, Feitosa-Araujo E, Fuchs P, Parmagnani AS, **Grenzi M**, Balcerowicz D, Schoenaers S, de la Torre C, Nunes-Nesi A, Wirtz M, Vissenber K, Van Aken O, Hause B, Costa A, Schwarzlander M (2022) *MCU proteins dominate in vivo mitochondrial Ca^{2+} uptake in Arabidopsis roots.* ***Accepted in The Plant Cell***. (contribution: imaging experiments execution).

Reviews

Grenzi M, Bonza MC, Alfieri A, Costa A (2020) *Structural insights into long-distance signal transduction pathways mediated by plant glutamate receptor-like channels*. ***New Phytol.*** *229: 1261-1267*. (contribution: preparation of figures, feedback on the manuscript preparation)

Resentini F, Ruberti C, **Grenzi M**, Bonza MC, Costa A (2021) *The signature of organellar calcium.* ***Plant Physiol***. *187: 1985-2004*. (contribution: preparation of figures).

Grenzi M, Resentini F, Vanneste S, Zottii M, Bassi A, Costa A (2021) *Illuminating the hidden world of calcium ions in plants with a universe of indicators.* ***Plant Physiol***. *187: 550-571.* (contribution: imaging experiments execution and analysis, preparation of figures, feedback on the manuscript preparation)

Grenzi M, Bonza MC, Costa A (2022) *Signaling by plant glutamate receptor-like channels: what else!* ***Current Opinion in Plant Biology*****.** 68:102253 (contribution: preparation of figures, feedback on the manuscript preparation).

Manuscript in preparation

Grenzi M, Parmagnani AS, Buratti S, Abdel Aziz I, Bernacka-Wojcik I, Resentini F, Šimura J, Doccula FG, Alfieri A, Luoni L, Ljung K, Bonza MC, Stavrinidou E, Costa A (2022) *Long-distance hydraulic signals induce local activation of plant glutamate receptor-like channels*. In preparation/revision. (contribution: project conceivment, experiments design, imaging experiments execution and analysis, preparation of figures and videos, feedback on the manuscript preparation)

The structural bases for agonist diversity in an *Arabidopsis thaliana* glutamate receptor-like channel

Andrea Alfieri[a,1,2], Fabrizio G. Doccula[a,3], Riccardo Pederzoli[a,b,3], Matteo Grenzi[a], Maria Cristina Bonza[a], Laura Luoni[a], Alessia Candeo[c], Neli Romano Armada[c,d], Alberto Barbiroli[e], Gianluca Valentini[c], Thomas R. Schneider[b], Andrea Bassi[c], Martino Bolognesi[a,f], Marco Nardini[a], and Alex Costa[a,g,1]

[a]Department of Biosciences, University of Milan, 20133 Milan, Italy; [b]European Molecular Biology Laboratory, Hamburg Unit c/o DESY, European Molecular Biology Laboratory, 22603 Hamburg, Germany; [c]Department of Physics, Politecnico di Milano, 20133 Milan, Italy; [d]Instituto de Investigaciones para la Industria Química, Faculty of Engineering, National University of Salta, 4400 Salta, Argentina; [e]Department of Food, Environmental and Nutritional Sciences, University of Milan, 20133 Milan, Italy; [f]Pediatric Research Center "Romeo ed Enrica Invernizzi," University of Milan, 20133 Milan, Italy; and [g]Institute of Biophysics, National Research Council of Italy (CNR), 20133 Milan, Italy

Edited by Gloria M. Coruzzi, New York University, New York, NY, and approved November 27, 2019 (received for review April 2, 2019)

***Arabidopsis thaliana* glutamate receptor-like (GLR) channels are amino acid-gated ion channels involved in physiological processes including wound signaling, stomatal regulation, and pollen tube growth. Here, fluorescence microscopy and genetics were used to confirm the central role of GLR3.3 in the amino acid-elicited cytosolic Ca^{2+} increase in *Arabidopsis* seedling roots. To elucidate the binding properties of the receptor, we biochemically reconstituted the GLR3.3 ligand-binding domain (LBD) and analyzed its selectivity profile; our binding experiments revealed the LBD preference for L-Glu but also for sulfur-containing amino acids. Furthermore, we solved the crystal structures of the GLR3.3 LBD in complex with 4 different amino acid ligands, providing a rationale for how the LBD binding site evolved to accommodate diverse amino acids, thus laying the grounds for rational mutagenesis. Last, we inspected the structures of LBDs from nonplant species and generated homology models for other GLR isoforms. Our results establish that GLR3.3 is a receptor endowed with a unique amino acid ligand profile and provide a structural framework for engineering this and other GLR isoforms to investigate their physiology.**

GLR channels | X-ray crystallography | binding assay | modeling | Ca^{2+} signaling

Plant glutamate receptor-like (GLR) channels are plant homologs of mammalian ionotropic glutamate receptors (iGluRs) (1). iGluRs are homo- or heterotetrameric cation channels activated by the neurotransmitters L-glutamate, glycine, and D-serine released in the synaptic space. They are extensively studied for their central role in neurotransmission, learning, and memory (2).

The identification of iGluR homologs in other eukaryotes, including invertebrates and plants, and cyanobacteria has outlined the existence of a large family of GLR proteins across all kingdoms of life. In particular, the stoichiometry and architecture of plant GLRs are believed to be similar to iGluRs (3): Each subunit hosts an extracellular amino-terminal domain (ATD), an extracellular ligand-binding domain (LBD) composed of segments S1 and S2, 4 transmembrane helices (M1 to M4, 1 of which—M2—is not fully transmembrane), and a cytoplasmic tail (carboxyl-terminal domain; CTD), arranged in the order ATD-S1-M1-M2-M3-S2-M4-CTD (*SI Appendix*, Fig. S1*A*). The LBD has a conserved clamshell architecture resembling the periplasmic binding protein-like II superfamily in bacteria (4); in vertebrates, the binding of a ligand/agonist induces a variable degree of closure of the clamshell that pulls the transmembrane segments and opens the channel pore (2).

The 20 *Arabidopsis thaliana* GLR isoforms are grouped in 3 clades (5, 6). Specific isoforms have been implicated in several physiological processes, such as root growth (7), hypocotyl elongation (8), seed germination (9), long-distance wound signaling (10–12), pollen tube growth (13, 14), stomatal aperture (15, 16), as well as Ca^{2+} signaling (17–20); such isoforms are then considered Ca^{2+}-permeable channels. In particular, the *A. thaliana* GLR3.3 isoform has been studied for its role in amino acid-induced cytosolic Ca^{2+} concentration ($[Ca^{2+}]_{cyt}$) increases (17, 21), and recently recognized as a key player in glutamate-mediated defense signaling (11). Despite genetic data supporting the role of GLRs as amino acid receptors (11, 16–22), no biochemical binding assay has demonstrated that any plant GLR isoform can indeed bind glutamate or other ligands. Furthermore, whereas for iGluRs hundreds of X-ray structures are available for the LBD moiety (23) and an increasing number of cryoelectron microscopy full-length structures are accumulating (24–27) (*SI Appendix*, Fig. S1*B*), no structural information for any plant GLR isoform is available to date.

In the present study, we set out to investigate the role of *A. thaliana* GLR3.3 in the generation of amino acid-elicited cytosolic Ca^{2+} transients and reconstituted its ligand-binding domain in vitro. The determination of its selectivity profile by binding

Significance

Glutamate receptor-like (GLR) channels are plant homologs of glutamate receptors in vertebrate synapses; they are calcium-permeable channels involved in root and pollen tube growth, stomatal regulation, and wound signaling. This study presents crystal structures of a plant GLR ligand-binding domain (LBD) in complex with 4 different amino acid ligands and identifies the protein residues responsible for amino acid binding. Binding assays show that the amino acids that trigger GLR-mediated calcium influx in *Arabidopsis thaliana* root tip cells bind the GLR LBD with micromolar affinities.

Author contributions: A.A. and A. Costa designed and directed the research; A.A. and M.C.B generated the constructs of GLR3.3 LBD and the mutated versions; A.A. expressed, purified, and characterized the proteins; A. Barbiroli performed the circular dichroism experiments; A.A. performed the MST analyses and the crystallization experiments; A.A. and R.P. solved and refined the crystal structures of GLR3.3 LBD; A.A. analyzed the structures; L.L. generated the knock-out mutant lines expressing the NES-YC3.6; F.G.D., M.G., A. Candeo, N.R.A., and A. Bassi performed the imaging experiments; M.C.B. performed the yeast complementation tests; A.A., F.G.D, R.P., M.G., A. Candeo, G.V., A. Barbiroli, G.V., T.R.S., A. Bassi, M.B., M.N., and A. Costa analyzed the data; A.A. and A. Costa generated the figures and the supplemental material; and A.A. and A. Costa wrote the paper.

The authors declare no competing interest.

This article is a PNAS Direct Submission.

Published under the PNAS license.

Data deposition: The atomic coordinates and structure factors reported in this paper have been deposited in the Protein Data Bank, http://www.wwpdb.org (PDB ID codes 6R85, 6R88, 6R89, and 6R8A for the complexes of the GLR3.3 LBD with L-Glu, Gly, L-Cys, and L-Met, respectively).

[1] To whom correspondence may be addressed. Email: andrea.alfieri@unimi.it or alex.costa@unimi.it.

[2] Present address: Centro Grandi Strumenti, University of Pavia, 27100 Pavia, Italy.

[3] F.G.D. and R.P. contributed equally to this work.

This article contains supporting information online at https://www.pnas.org/lookup/suppl/doi:10.1073/pnas.1905142117/-/DCSupplemental.

doi:10.1093/plphys/kiab251

PLANT PHYSIOLOGY 2021: 187: 603–617

Plant Physiology®

Breakthrough Tech

Simultaneous imaging of ER and cytosolic Ca^{2+} dynamics reveals long-distance ER Ca^{2+} waves in plants

Francesca Resentini[1,‡] **Matteo Grenzi**[1,‡] **Daniele Ancora**[2] **Mara Cademartori,**[1] **Laura Luoni**[1] **Marianna Franco**[1] **Andrea Bassi**[2] **Maria Cristina Bonza**[1] **and Alex Costa**[1,3,*,†]

1 Department of Biosciences, University of Milan, Milan 20133, Italy
2 Department of Physics, Politecnico di Milano, Milan 20133, Italy
3 Institute of Biophysics, Consiglio Nazionale Delle Ricerche, Milan 20133, Italy

*Author for communication: alex.costa@unimi.it

†Senior author.

‡These authors contributed equally to this work (F.R. and M.G.).

A.C. and M.C.B. conceived the project with specific input from F.R., M.G., and A.B., M.G., and A.C. designed the experiments. F.R., M.C., and M.F. generated the constructs. F.R., M.G., and M.F. performed and analyzed the experiments. F.R. and L.L. generated the transgenic lines. D.A. and A.B. performed cross-correlation analyses of Figure 3 and temporal evolution of signals in Figure 4. A.C. and M.G. prepared the figures and videos. A.C. and M.C.B. wrote the manuscript with input from all coauthors. A.C. agrees to serve as the author responsible for contact and ensures communication.

The author responsible for distribution of materials integral to the findings presented in this article in accordance with the policy described in the Instructions for Author (https://academic.oup.com/plphys/pages/general-instructions) is: Alex Costa (alex.costa@unimi.it).

Abstract

Calcium ions (Ca^{2+}) play a key role in cell signaling across organisms. In plants, a plethora of environmental and developmental stimuli induce specific Ca^{2+} increases in the cytosol as well as in different cellular compartments including the endoplasmic reticulum (ER). The ER represents an intracellular Ca^{2+} store that actively accumulates Ca^{2+} taken up from the cytosol. By exploiting state-of-the-art genetically encoded Ca^{2+} indicators, specifically the ER-GCaMP6-210 and R-GECO1, we report the generation and characterization of an Arabidopsis (*Arabidopsis thaliana*) line that allows for simultaneous imaging of Ca^{2+} dynamics in both the ER and cytosol at different spatial scales. By performing analyses in single cells, we precisely quantified (1) the time required by the ER to import Ca^{2+} from the cytosol into the lumen and (2) the time required to observe a cytosolic Ca^{2+} increase upon the pharmacological inhibition of the ER-localized P-Type IIA Ca^{2+}-ATPases. Furthermore, live imaging of mature, soil-grown plants revealed the existence of a wounding-induced, long-distance ER Ca^{2+} wave propagating in injured and systemic rosette leaves. This technology enhances high-resolution analyses of intracellular Ca^{2+} dynamics at the cellular level and in adult organisms and paves the way to develop new methodologies aimed at defining the contribution of subcellular compartments in Ca^{2+} homeostasis and signaling.

Introduction

In animals, besides its role in protein secretion, the endoplasmic reticulum (ER) is a calcium ions (Ca^{2+}) store participating in the generation and shaping of stimulus-induced cytosolic Ca^{2+} increases (Soboloff et al., 2012). Moreover, in animals, Ryanodine (RyR) and inositol trisphosphate ($InsP_3R$) receptors are ER-localized, ligand-gated Ca^{2+} permeable channels that release Ca^{2+} into the cytosol (Foskett et al.,

Received February 02, 2021. Accepted May 12, 2021. Advance access publication May 29, 2021

© American Society of Plant Biologists 2021. All rights reserved. For permissions, please email: journals.permissions@oup.com

SOCIETY FOR EXPERIMENTAL BIOLOGY

Journal of Experimental Botany
https://doi.org/10.1093/jxb/erac019 Advance Access Publication 27 January, 2022

RESEARCH PAPER

Auxin analog-induced Ca^{2+} signaling is independent of inhibition of endosomal aggregation in Arabidopsis roots

Ren Wang[1,2,*], Ellie Himschoot[1,2,*], Matteo Grenzi[3,*], Jian Chen[1,2], Alaeddine Safi[1,2], Melanie Krebs[4], Karin Schumacher[4], Moritz K. Nowack[1,2], Wolfgang Moeder[5], Keiko Yoshioka[5], Daniël Van Damme[1,2], Ive De Smet[1,2], Danny Geelen[6], Tom Beeckman[1,2], Jiří Friml[7], Alex Costa[3,8,†] and Steffen Vanneste[1,6,9,†]

[1] Department of Plant Biotechnology and Bioinformatics, Ghent University, 9052 Ghent, Belgium
[2] VIB Center for Plant Systems Biology, 9052 Ghent, Belgium
[3] Department of Biosciences, University of Milan, 20133 Milan, Italy
[4] Centre for Organismal Studies, Plant Developmental Biology, University of Heidelberg, 69120 Heidelberg, Germany
[5] Department of Cell and Systems Biology, University of Toronto, Toronto, ON M5S 3B2, Canada
[6] Department of Plants and Crops, Ghent University, 9000 Ghent, Belgium
[7] Institute of Science and Technology Austria (IST Austria), 3400 Klosterneuburg, Austria
[8] Institute of Biophysics, National Research Council of Italy (CNR), 20133 Milan, Italy
[9] Lab of Plant Growth Analysis, Ghent University Global Campus, Incheon 21985, Republic of Korea

[*] These authors contributed equally to this work.
[†] Correspondence: steffen.vanneste@ugent.be or alex.costa@unimi.it

Received 17 November 2021; Editorial decision 14 January 2022; Accepted 25 January 2022

Editor: Richard Napier, University of Warwick, UK

Abstract

Much of what we know about the role of auxin in plant development derives from exogenous manipulations of auxin distribution and signaling, using inhibitors, auxins, and auxin analogs. In this context, synthetic auxin analogs, such as 1-naphthalene acetic acid (1-NAA), are often favored over the endogenous auxin, indole-3-acetic acid (IAA), in part due to their higher stability. While such auxin analogs have proven instrumental in revealing the various faces of auxin, they display in some cases bioactivities distinct from IAA. Here, we focused on the effect of auxin analogs on the accumulation of PIN proteins in brefeldin A-sensitive endosomal aggregations (BFA bodies), and correlation with the ability to elicit Ca^{2+} responses. For a set of commonly used auxin analogs, we evaluated if auxin analog-induced Ca^{2+} signaling inhibits PIN accumulation. Not all auxin analogs elicited a Ca^{2+} response, and their differential ability to elicit Ca^{2+} responses correlated partially with their ability to inhibit BFA-body formation. However, in *tir1/afb* and *cngc14*, 1-NAA-induced Ca^{2+} signaling was strongly impaired, yet 1-NAA still could inhibit PIN accumulation in BFA bodies. This demonstrates that TIR1/AFB–CNGC14-dependent Ca^{2+} signaling does not inhibit BFA body formation in Arabidopsis roots.

Keywords: Arabidopsis, auxin analogs, calcium, endosomes, PIN protein, root, signaling, trafficking.

Abbreviations: 1/2-NAA, 1/2-naphthalene acetic acid; 2,4-D, 2,4-dichlorophenoxyacetic acid; BA, benzoic acid; BFA, brefeldin A; CNGC, CYCLIC NUCLEOTIDE GATED CHANNEL; IAA, indole-3-acetic acid; PAA, phenyl acetic acid; PEO-IAA, α-(phenyl ethyl-2-one)-indole-3-acetic acid; PIN, PIN-FORMED; TIR1/AFB, TRANSPORT INHIBITOR RESISTANT1/AUXIN-RELATED F-BOX.

© The Author(s) 2022. Published by Oxford University Press on behalf of the Society for Experimental Biology. All rights reserved.
For permissions, please email: journals.permissions@oup.com

Green Tea Catechins, (−)-Catechin Gallate, and (−)-Gallocatechin Gallate are Potent Inhibitors of ABA-Induced Stomatal Closure

*Kanane Sato, Shunya Saito, Kohsuke Endo, Masaru Kono, Taishin Kakei, Haruka Taketa, Megumi Kato, Shin Hamamoto, Matteo Grenzi, Alex Costa, Shintaro Munemasa, Yoshiyuki Murata, Yasuhiro Ishimaru, and Nobuyuki Uozumi**

Stomatal movement is indispensable for plant growth and survival in response to environmental stimuli. Cytosolic Ca^{2+} elevation plays a crucial role in ABA-induced stomatal closure during drought stress; however, to what extent the Ca^{2+} movement across the plasma membrane from the apoplast to the cytosol contributes to this process still needs clarification. Here the authors identify (−)-catechin gallate (CG) and (−)-gallocatechin gallate (GCG), components of green tea, as inhibitors of voltage-dependent K^+ channels which regulate K^+ fluxes in *Arabidopsis thaliana* guard cells. In *Arabidopsis* guard cells CG/GCG prevent ABA-induced: i) membrane depolarization; ii) activation of Ca^{2+} permeable cation (I_{Ca}) channels; and iii) cytosolic Ca^{2+} transients. In whole *Arabidopsis* plants co-treatment with CG/GCG and ABA suppressed ABA-induced stomatal closure and surface temperature increase. Similar to ABA, CG/GCG inhibited stomatal closure is elicited by the elicitor peptide, flg22 but has no impact on dark-induced stomatal closure or light- and fusicoccin-induced stomatal opening, suggesting that the inhibitory effect of CG/GCG is associated with Ca^{2+}-related signaling pathways. This study further supports the crucial role of I_{Ca} channels of the plasma membrane in ABA-induced stomatal closure. Moreover, CG and GCG represent a new tool for the study of abiotic or biotic stress-induced signal transduction pathways.

1. Introduction

When plants undergo environmental changes or biotic stress, they regulate the opening and closure of stomata to ensure transpiration, prevent water, loss or bacterial invasion to maintain intracellular homeostasis. ABA signal transduction plays a central role in this stomatal closure during drought stress.[1–3] Drought stimulus elicits the synthesis of plant hormones such as ABA. This is followed by ABA binding to the ABA receptors in guard cell which initiates downstream responses including ion uptake and excretion, intracellular calcium ion (Ca^{2+}) transient increase, generation of Reactive Oxygen Species, and protein phosphorylation/dephosphorylation, resulting in the excretion of ions, solutes, and water from guard cells which leads to a decrease in the turgor pressure and cell volume.[4–7]

Plant cells contain potassium ions (K^+) as the major cations for controlling membrane

---

K. Sato, S. Saito, K. Endo, T. Kakei, H. Taketa, M. Kato, S. Hamamoto, Y. Ishimaru, N. Uozumi
Department of Biomolecular Engineering
Graduate School of Engineering
Tohoku University
Aobayama 6-6-07, Sendai 980-8579, Japan
E-mail: uozumi@tohoku.ac.jp

The ORCID identification number(s) for the author(s) of this article can be found under https://doi.org/10.1002/advs.202201403

© 2022 The Authors. Advanced Science published by Wiley-VCH GmbH This is an open access article under the terms of the Creative Commons Attribution License, which permits use, distribution and reproduction in any medium, provided the original work is properly cited.

DOI: 10.1002/advs.202201403

M. Kono
Department of Biology
Graduate School of Science
University of Tokyo
Bunkyo-ku 113-0033, Japan

M. Grenzi, A. Costa
Department of Biosciences
University of Milan
Via G. Celoria 26, Milan 20133, Italy
E-mail: alex.costa@unimi.it

A. Costa
Institute of Biophysics
National Research Council of Italy (CNR)
Via G. Celoria 26, Milan 20133, Italy

S. Munemasa, Y. Murata
Graduate School of Environmental and Life Science
Okayama University
Tsushima, Okayama 700-8530, Japan

New Phytologist

Review

Tansley insight

Structural insights into long-distance signal transduction pathways mediated by plant glutamate receptor-like channels

Author for correspondence:
Alex Costa
Email: alex.costa@unimi.it

Received: *30 July 2020*
Accepted: *29 September 2020*

Matteo Grenzi[1], Maria Cristina Bonza[1], Andrea Alfieri[2] and Alex Costa[1,3]

[1]Department of Biosciences, University of Milan, Via G. Celoria 26, Milano 20133, Italy; [2]Centro Grandi Strumenti, University of Pavia, via Ferrata 9, Pavia 27100, Italy; [3]Institute of Biophysics, National Research Council of Italy (CNR), Via G. Celoria 26, Milano 20133, Italy

Contents

Summary 1261
I. Introduction: plant glutamate receptor-like channels 1261
II. Structural features and conservation in GLRs 1262
III. GLRs in long-distance electrical and Ca^{2+} signaling 1262
IV. How do plant GLRs work? 1263
V. Concluding remarks and perspectives 1265
Acknowledgements 1266
References 1266

New Phytologist (2021) **229**: 1261–1267
doi: 10.1111/nph.17034

Key words: AtGLR3.3 ligand-binding domain structure, glutamate receptor-like channels, long-distance calcium signalling, plant intercellular communication, vascular tissues.

Summary

In recent years, studies have shed light on the physiological role of plant glutamate receptor-like channels (GLRs). However, the mechanism by which these channels are activated, and in particular, what is the physiological role of their binding to amino acids, remains elusive. The first direct biochemical demonstration that the *Arabidopsis thaliana* GLR3.3 isoform binds glutamate and other amino acids in a low micromolar range of concentrations was reported only recently. The first crystal structures of the ligand-binding domains of *At*GLR3.3 and *At*GLR3.2 isoforms also have been released. We foresee that these new experimental pieces of evidence provide the basis for a better understanding of how GLRs are activated and modulated in different physiological responses.

I. Introduction: plant glutamate receptor-like channels

Calcium (Ca^{2+}) is a key second messenger in plant cells. It is universally involved in different developmental programs as well as in plant local and systemic responses to changing environments. The generation of free cytosolic Ca^{2+} transients requires the opening of Ca^{2+}-permeable channels which regulate cytosolic Ca^{2+} influx (Kudla *et al.*, 2018).

Ionotropic glutamate receptors (iGluRs) are ligand-gated nonselective cation channels that mediate neurotransmission in the animal central nervous system (Traynelis *et al.*, 2010). Homologous proteins were identified in plants, namely glutamate receptor-like channels (GLRs). In *Arabidopsis thaliana*, 20 GLR members were grouped into three clades (I, II and III; Lam *et al.*, 1998), and have been found to be involved in root development, seed germination, ion transport, metabolic pathways and Ca^{2+} signaling (reviewed in Wudick *et al.*, 2018a). Several members of the Arabidopsis GLRs are expressed in pollen and are crucial for the generation of the Ca^{2+}-tip gradient as well as for proper pollen tube growth, attraction and fertility (Michard *et al.*, 2011; Wudick *et al.*, 2018b; Mou *et al.*, 2020). In addition, the two *Physcomitrella patens* GLRs are essential for both chemotaxis and reproduction (Ortiz-Ramírez *et al.*, 2017). Intriguingly, both Arabidopsis and *Solanum lycopersicum* GLRs, particularly those belonging to Clade III, are elemental in long-distance signaling (Mousavi *et al.*, 2013; Farmer *et al.*, 2014; Nguyen *et al.*, 2018; Toyota *et al.*, 2018; Wang *et al.*, 2019; Goto *et al.*, 2020; Shao *et al.*, 2020).

© 2020 The Authors
New Phytologist © 2020 New Phytologist Foundation

doi:10.1093/plphys/kiab189 PLANT PHYSIOLOGY 2021: 187: 1985–2004

Plant Physiology®

Update

The signatures of organellar calcium

Francesca Resentini ,[1] **Cristina Ruberti,**[1] **Matteo Grenzi,**[1] **Maria Cristina Bonza** [1] **and**
Alex Costa [1,2,*,†]

1 Department of Biosciences, University of Milan, Milano 20133, Italy
2 Institute of Biophysics, National Research Council of Italy (CNR), Milano 20133, Italy

*Author for communication: alex.costa@unimi.it
†Senior author.

A.C. conceived the project and wrote the main body of the article. F.R. wrote the part on developmental processes. M.G. prepared Figures 1 and 3. M.C.B. prepared Box 2. All authors made comments on the manuscript, which were integrated by A.C. All authors contributed to the article and approved the submitted version.

The author responsible for distribution of materials integral to the findings presented in this article in accordance with the policy described in the Instructions for Authors (https://academic.oup.com/plphys/pages/general-instructions) is: Alex Costa (alex.costa@unimi.it).

Abstract

Recent insights about the transport mechanisms involved in the in and out of calcium ions in plant organelles, and their role in the regulation of cytosolic calcium homeostasis in different signaling pathways.

Introduction

Plants are continuously subjected to environmental changes, such as fluctuating light, the day/night cycle, oscillating temperatures, water availability, and interaction with other organisms. Often these variations can be adverse, being stressful and thus affecting plant growth, development and, in several cases, causing major yield losses in agriculture. Especially, plants cannot move to a more comfortable environment to survive and they, thus, need to continuously monitor, and possibly anticipate, any upcoming stress (Zhu, 2016).

Plants' early responses to stress often occur in a time frame of seconds or a few minutes in different cell compartments, and in these cases, they mainly rely on quick changes of ions' concentrations (e.g. Ca^{2+}, H^+, K^+, NO^{3-}, Cl^-) which are dependent upon their movements across membranes (Stephan et al., 2016; Behera et al., 2018; Costa et al., 2018; Demes et al., 2020; Martí Ruiz et al., 2020). Among the ions, it is well-accepted that calcium (Ca^{2+}) plays a key role in many signal transduction pathways (Trewavas and Malhó, 1998; Sanders et al., 2002; Dodd et al., 2010; Kudla et al., 2010, 2018; Tian et al., 2020). At rest, in plant cells, the cytosolic free Ca^{2+} concentration ($[Ca^{2+}]_{cyt}$) is in the range of 100–200 nM (Trewavas, 1999; Logan and Knight, 2003; Stael et al., 2012; Jezek and Blatt, 2017), but it can rise steeply (often too low µM concentrations) in response to the perception of different stimuli (Knight et al., 1997; Ranf et al., 2008). Importantly, the stimulus-induced increase in $[Ca^{2+}]_{cyt}$ is not a "digital signal," but an "analog" one that, depending on the stimulus type and magnitude, assumes a peculiar dynamic often dubbed "cytosolic Ca^{2+} signature" (Sanders et al., 2002; Kudla et al., 2010, 2018; Tian et al., 2020). The model predicts that different signatures activate different Ca^{2+} sensors (e.g. Calmodulin [CaM], CaM-like proteins [CMLs], calcineurin β-like proteins [CBLs]), and Ca^{2+} relays (e.g. Ca^{2+}-dependent protein kinases [CDPKs], or CaM-dependent protein kinase [CCaMK]) that trigger precise and tailored responses, altering gene expression and metabolism (Figure 1; reviewed in Sanders et al., 2002; McCormack et al., 2005; DeFalco et al., 2009; Hamel et al., 2014; Edel et al., 2017; Kudla et al., 2018; Lenzoni et al., 2018; Poovaiah and Du, 2018; Liu et al., 2020; Tang et al., 2020). The understanding of how the Ca^{2+} signature is generated and shaped to assume its "analog nature" is a key aspect to dissect the roots of Ca^{2+} signaling, which is traceable to its movement across membranes. Thus, important questions are (1) how do plant cells generate specific Ca^{2+} signatures? (2) which are the mechanisms for their tight regulation? A simple answer is that generation and shaping of cytosolic

Received January 19, 2021. Accepted April 10, 2021. Advance access publication April 27, 2021
© American Society of Plant Biologists 2021. All rights reserved. For permissions, please email: journals.permissions@oup.com

doi:10.1093/plphys/kiab339
PLANT PHYSIOLOGY 2021: 187: 550–571

Plant Physiology®

Illuminating the hidden world of calcium ions in plants with a universe of indicators

Matteo Grenzi [1], Francesca Resentini [1], Steffen Vanneste [2,3,4] Michela Zottini [5], Andrea Bassi [6,7] and Alex Costa [1,8,*,†]

1 Department of Biosciences, University of Milan, 20133 Milano, Italy
2 Department of Plant Biotechnology and Bioinformatics, Ghent University, 9052 Ghent, Belgium
3 Department of Plants and Crops, Ghent University, 9000 Ghent, Belgium
4 Laboratory of Plant Growth Analysis, Ghent University Global Campus, Incheon 21985, South Korea
5 Department of Biology, University of Padova, 35131 Padova, Italy
6 Department of Physics, Politecnico di Milano, 20133 Milano, Italy
7 Institute of Photonics and Nanotechnologies, National Research Council of Italy (CNR), 20133 Milano, Italy
8 Institute of Biophysics, National Research Council of Italy (CNR), 20133 Milano, Italy

*Author for communication: alex.costa@unimi.it
†Senior author

M.G. carried out the experiments reported in Figures 3 and 4 and prepared Figures 1, 3, and 4. F.R. prepared Tables 1 and 4. A.C. conceived the project and wrote the article with feedback from all authors. A.C. serves as the author responsible for contact and ensures communication.
The author responsible for distribution of materials integral to the findings presented in this article in accordance with the policy described in the Instructions for Authors (https://academic.oup.com/plphys/pages/General Instructions) is Alex Costa (alex.costa@unimi.it).

Introduction

Calcium (Ca^{2+}) is a well-known second messenger in both unicellular and multicellular organisms (Berridge et al., 2000; Carafoli and Krebs, 2016). In plants, apart from its role as a structural component (White and Broadley, 2003), calcium plays a role in signaling events in response to a multitude of developmental and environmental stimuli (Kudla et al., 2010; Edel et al., 2017; Kudla et al., 2018). Biotic and abiotic challenges affect the cellular Ca^{2+} homeostasis by triggering transient changes of Ca^{2+} concentrations in the cytosol as well as in subcellular compartments (McAinsh and Pittman, 2009; Stael et al., 2012; Costa et al., 2018; Pirayesh et al., 2021; Resentini et al., 2021b).

The basis of calcium's role as a signaling component lies in its peculiar chemistry and the existence of a large electrochemical gradient across the cell's membranes, maintained by the activity of the proton- and calcium-ATPases (H^{+}-ATPases and Ca^{2+}-ATPases; Palmgren, 2001; Demidchik et al., 2018; Klejchova et al., 2021). The main evolutionary reason for evolving mechanisms that generate and maintain this large gradient is based on the need to keep the cytosolic Ca^{2+} concentrations ([Ca^{2+}]$_{cyt}$) low, to prevent the precipitation of organic and inorganic molecules (e.g.

ADVANCES

- GECIs have been efficiently employed in plants.
- In vivo Ca^{2+} imaging at high spatial and temporal resolution is possible at tissue, cell, and organelle levels.
- Plants expressing GECIs with different affinities for Ca^{2+} are available for cytosolic and organellar analyses.
- Ratiometric GECIs allow a reliable comparison of Ca^{2+} levels in different genetic backgrounds and in long-term treatments.
- Intensiometric GECIs require simple and cost-effective imaging setups.

Received February 23, 2021. Accepted July 15, 2021
© American Society of Plant Biologists 2021. All rights reserved. For permissions, please email: journals.permissions@oup.com

Available online at www.sciencedirect.com

ScienceDirect

Current Opinion in
Plant Biology

Signaling by plant glutamate receptor-like channels: What else!

Matteo Grenzi[1], Maria Cristina Bonza[1] and Alex Costa[1,2]

Abstract

Plant glutamate receptor-like channels (GLRs) are transmembrane proteins that allow the movement of several ions across membranes. In the model plant Arabidopsis, there are 20 GLR isoforms grouped in three clades and, since their discovery, it was hypothesized that GLRs were mainly involved in signaling processes. Indeed, in the last years, several pieces of evidence demonstrate different signaling roles played by GLRs, related to pollen development, sexual reproduction, chemotaxis, root development, regulation of stomatal aperture, and response to pathogens. Recently, GLRs have gained attention for their role in long-distance electric and calcium signaling. In this review, we resume the evidence about the role of GLRs in signaling processes. This role is mostly linked to the GLRs involvement in the regulation of ion fluxes across membranes and, in particular, of calcium, which represents a key second messenger in plant cell responses to both endogenous and exogenous stimuli.

Addresses
[1] Department of Biosciences, University of Milan, Via G. Celoria 26, 20133 Milano, Italy
[2] Institute of Biophysics, National Research Council of Italy (CNR), Via G. Celoria 26, 20133 Milano, Italy

Corresponding author: Costa, Alex (alex.costa@unimi.it)

Current Opinion in Plant Biology 2022, **68**:102253

This review comes from a themed issue on **Cell biology and cell signalling**

Edited by **Stefanie Sprunck**, **Claus Schwechheimer** and **Miyo Morita**

For a complete overview see the Issue and the Editorial

Available online xxx

https://doi.org/10.1016/j.pbi.2022.102253

1369-5266/© 2022 Elsevier Ltd. All rights reserved.

Introduction

Glutamate receptor-like channels (GLRs) are proteins homologous to the animal ligand-gated ion channels activated by excitatory amino acids (AA) and named ionotropic glutamate receptors (iGluRs) [1,2]. In animals, iGluRs play key roles in almost all aspects of brain function [3]. In plants, GLRs are involved in several processes such as development, regulation of stomatal aperture, response to mechanical wounding and herbivore attack, immunity, reproduction, and chemotaxis [4–13]. Since the discovery of plant GLRs [14], which are grouped in three clades (I, II, III), it was believed that their structure resembled that of iGluRs, therefore, acting as ligand-gated ion channels, with L-glutamate (L-glu) or glycine [15] as main ligands. Plant cells respond to exogenous L-glu administration showing plasma membrane depolarization and an increase in cytosolic calcium (Ca^{2+}) concentration ($[Ca^{2+}]_{cyt}$), a response that in *Arabidopsis thaliana* is primarily dependent on *At*GLR3.3 [16–18]. However, besides L-glu, plant cells showed membrane depolarization and $[Ca^{2+}]_{cyt}$ increase also in response to other exogenously administered AA, including glycine, L-alanine, L-cysteine, L-serine, L-asparagine, and L-methionine [17–19], whereas D-serine modulates $[Ca^{2+}]_{cyt}$ oscillations and growth in pollen tubes [20]. The hypothesis that the architecture and stoichiometry of GLRs resemble those of iGluRs [1] was confirmed with the first available crystal structures of the ligand-binding domain (LBD) of the Arabidopsis *At*GLR3.3 and *At*GLR3.2 [18,21] and the single-particle cryo-EM structure of the full-length *At*GLR3.4 [22] (Figure 1). *In vitro* binding experiments performed on *At*GLR3.3- and *At*GLR3.4-LBDs revealed their preference not only for L-glu, but also for other residues including sulfur-containing AA (i.e. L-cysteine and L-methionine) [18,22] supporting their role as *bona fide* receptors activated by the AA-binding. Of interest, the ethylene precursor 1-aminocyclopropane-1-carboxylic acid (ACC) is also a potential GLRs ligand [12,23].

This review delves into different fields of cellular signaling in plants, examining the role of AA sensing and GLRs activity with a focus on reproduction, development, and responses to environmental clues (Figure 2).

GLRs roles in plant reproduction

In angiosperms, sexual reproduction relies on the recognition between pollen and ovules which involves rapid growth of the pollen tube within the female tissues. In this process, pollen performs a continued survey of compatible and incompatible interactions with different cell types with the final recognition of the egg cell leading to sperm delivery [24]. GLRs play key signaling roles in several steps of this pollen journey (Figure 2). In tobacco and Arabidopsis, D-serine

ACCEPTED

Research Article

MCU proteins dominate *in vivo* mitochondrial Ca^{2+} uptake in Arabidopsis roots

Cristina Ruberti [1], Stephan Wagner [1,2], Zhaolong Xu [3,4], Elias Feitosa-Araujo [1,5], Philippe Fuchs [1,2], Ambra Selene Parmagnani [3], Matteo Grenzi [3], Daria Balcerowicz [6], Sébastjen Schoenaers [6], Carolina de la Torre [7], Adriano Nunes-Nesi [5], Markus Wirtz [8], Kris Vissenberg [6,9], Olivier Van Aken [10], Bettina Hause [11], Alex Costa [3,12,a], Markus Schwarzländer [1,a]

[1] *Institute of Plant Biology and Biotechnology, University of Münster, Schlossplatz 8, D-48143 Münster, Germany*
[2] *Institute of Crop Science and Resource Conservation (INRES), University of Bonn, Friedrich-Ebert-Allee 144, D-53113 Bonn, Germany*
[3] *Department of Biosciences, University of Milano, Via Celoria 26, I-20133, Milan, Italy*
[4] *Provincial Key Laboratory of Agrobiology, Jiangsu Academy of Agricultural Sciences, Nanjing 210014, China*
[5] *Departamento de Biologia Vegetal, Universidade Federal de Viçosa, 36570-900 Viçosa, Minas Gerais, Brazil*
[6] *Integrated Molecular Plant Physiology Research, University of Antwerp, Campus Groenenborger 171, B-2020 Antwerp, Belgium*
[7] *Medical Research Center, University of Heidelberg, Theodor-Kutzer-Ufer 1-3, D-68167 Mannheim, Germany*
[8] *Centre for Organismal Studies (COS) Heidelberg, University of Heidelberg, Im Neuenheimer Feld 360, D-69120 Heidelberg, Germany*
[9] *Plant Biochemistry and Biotechnology Lab, Department of Agriculture, Hellenic Mediterranean University, Stavromenos, Heraklion, 71410, Crete, Greece*
[10] *Department of Biology, Lund University, Sölvegatan 35, Lund 223 62, Sweden*
[11] *Department of Cell and Metabolic Biology, Leibniz Institute of Plant Biochemistry (IPB), Weinberg 3, D-06120 Halle (Saale), Germany*
[12] *Institute of Biophysics, Consiglio Nazionale delle Ricerche (CNR), Via Celoria 26, I-20133 Milan, Italy*
[a] *Corresponding authors*

ABSTRACT

Ca^{2+} signaling is central to plant development and acclimation. While Ca^{2+}-responsive proteins have been investigated intensely in plants, only few Ca^{2+} channels are known, and our understanding of how intracellular Ca^{2+} fluxes are facilitated remains limited. Arabidopsis homologues of the mammalian channel-forming mitochondrial calcium uniporter (MCU) protein showed Ca^{2+} transport activity *in vitro*. Yet, the evolutionary complexity of MCU proteins, reports about alternative systems and unperturbed mitochondrial Ca^{2+} uptake in knockout lines of *MCU* genes leave critical questions about the *in vivo* functions of the MCU protein family in plants unanswered. Here, we demonstrate that MCU proteins mediate mitochondrial Ca^{2+} uptake *in planta* and that this uptake mechanism is the major route. We generate an *mcu* triple knockout line following the rationale of constraining the total MCU capacity. We use this model to explore *in vivo* mitochondrial Ca^{2+} uptake capacity by stimulating Ca^{2+} transients of different amplitudes and to reveal the significance of mitochondrial Ca^{2+} uptake on other plant functions. Using Ca^{2+} imaging in living root tips demonstrates that mitochondrial Ca^{2+} uptake becomes limiting in the triple mutant, where also the resting mitochondrial Ca^{2+} level is altered. This drastic cell physiological phenotype of subcellular Ca^{2+} transport impairment coincides with deregulated jasmonate-related signaling. Our findings establish MCUs as major mitochondrial Ca^{2+} entry route *in planta* and link mitochondrial Ca^{2+} transport with hormone signaling.